Light Scattering by Photonic Crystals with a Dirac Spectrum

Ruslan Sepkhanov

Light Scattering by Photonic Crystals with a Dirac Spectrum

PROEFSCHRIFT

DOOR

Ruslan Sepkhanov

GEBOREN TE MOSKOU IN 1983

Promotiecommissie:

Promotor: Prof. dr. C. W. J. Beenakker
Overige leden: Dr. M. J. A. de Dood
                   Prof. dr. A. Lagendijk (AMOLF)
                   Dr. A. P. Mosk (Universiteit Twente)
                   Prof. dr. J. M. van Ruitenbeek
                   Prof. dr. ir. W. van Saarloos

Посвящается моим родителям
и моей жене Ирине.

Contents

Chapter 1

Introduction

1.1 Photonic Crystals

Photonic crystals [1] are artificial materials with macroscopic arrangements of periodic modulation of dielectric and/or magnetic constant (see Figures 1.1, 1.2, 1.3, 1.5, 2.1, 3.1, 4.1). Known for the last few decades they are designed for the goal to control the optical properties of materials in pretty much the same way the crystal structure of metals and semiconductors controls propagation of electronic waves. From electronics and semiconductor physics we know that a periodic potential can forbid the propagation of electrons with certain energies and in certain directions, by creating a gap in the energy band structure. Outside of the gap, the electrons propagate freely, but with different properties (such as mass or magnetic moment) than electrons in free space. Photonic crystals being the optical analogue of ordinary crystals can therefore help us to design materials that perfectly reflect electromagnetic waves in a certain range of frequencies, or allow them to propagate only in one direction, or modify their free-space properties in other ways. This capability opens up a variety of opportunities for technological developments in laser physics, high-speed computing, spectroscopy and so forth. Additionally, since Maxwell's equations are scale invariant, photonic crystals can be constructed to control waves of almost any frequencies — limited only by our abilities to manipulate small objects.

The simplest photonic crystal is a periodic stack of layers with differ-
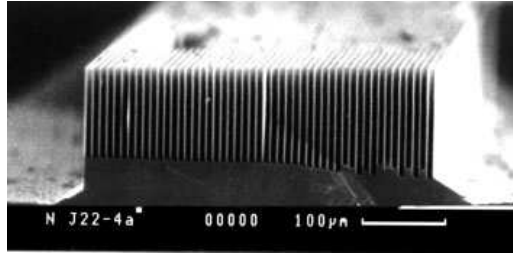
Figure 1.1. Scanning electron microscope image of a one-dimensional photonic crystal from Ref. [2].
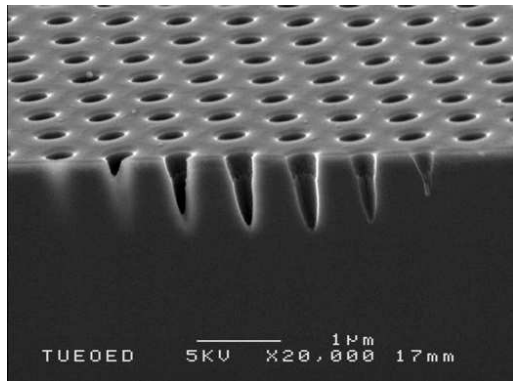
Figure 1.2. Scanning electron microscope image of a two-dimensional photonic crystal from Ref. [3].

ent dielectric constants (see Fig. 1.1). It is a one-dimensional crystal as it is periodic along one direction and homogeneous along the other two. This system was studied first by Lord Rayleigh in 1887. By summing multiple reflections and refractions at each interface he was able to shown that a multilayer film has a band gap. Consequently such a photonic crystal can serve as a mirror, known as a Bragg mirror, and it can confine electromagnetic waves by introducing certain defects in the periodic structure.

A two-dimensional photonic crystal is periodic in two directions and homogeneous in the third, like the one shown in Fig. 1.2. In two dimensions the electromagnetic waves decouple into TE modes (transverse electric, assuming the electric field to be in the plane of periodicity) and TM modes (transverse magnetic, assuming the magnetic field to be in the
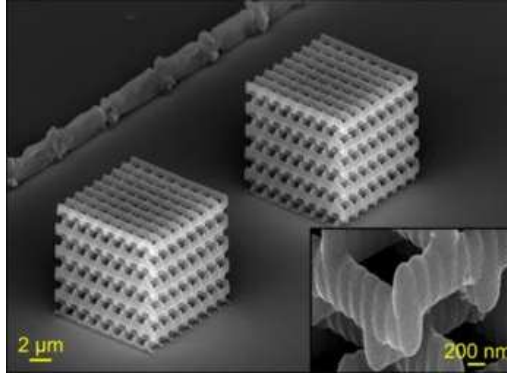
Figure 1.3. Scanning electron microscope image of a pair of three-dimensional photonic crystals with an inset showing enlarged voxels. From Ref. [4].

plane of periodicity). Each of those has its own bandstructure. A complete band gap may appear, originating from the interference of reflected and refracted waves. The band gap prevents light from propagating in any direction in the plane of periodicity. As a consequence in two-dimensions the light modes with a frequency within the band gap can be trapped by point defects in the crystal structure or guided from one location to another by line defects (linear defects). In addition there can appear surface states that live on the edge between the photonic crystal and free space.

Finally, the full optical analogue of a conventional crystal is a three-dimensional photonic crystal (see Fig. 1.3), which is periodic along three axes. Similar phenomena occur in this case as in the two-dimensional case with the additional possibility to confine electromagnetic radiation in all three dimensions.

Although we define photonic crystals as artificial structures, they can actually be found in inanimate nature as well as in animate nature. A mineral opal formed by silica microspheres organized in a hexagonal or cubic lattice [5, 6, 7, 8] is an example of a natural photonic crystal. A microphotograph of its surface is shown in the left panel of Fig. 1.4. The most often mentioned example of a photonic crystal in living creatures is the butterfly wing [9, 10] shown in the right panel of Fig. 1.4. Other examples of one-dimensional, two-dimensional and three-dimensional struc-
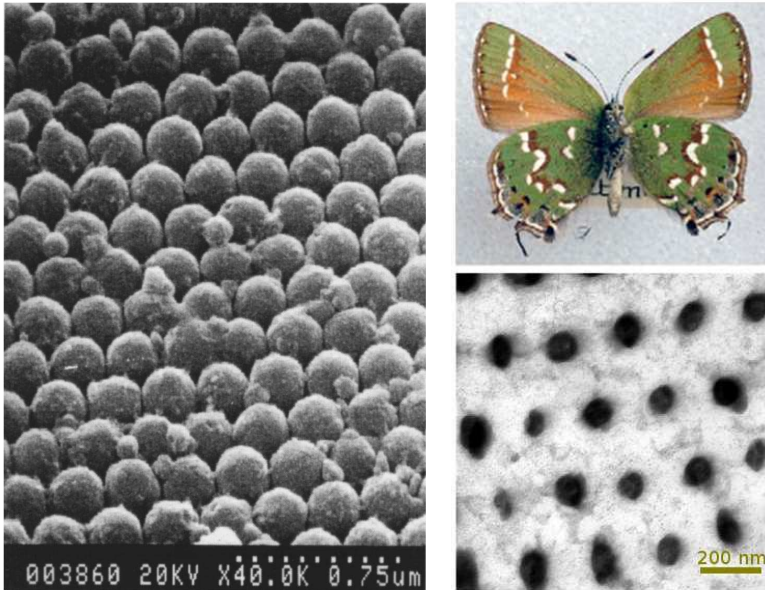
Figure 1.4.   Left panel: microphotograph of the opal surface from Ref. [12]; right panel: *Mitoura gryneus* butterfly and transmission electron microscope image of its structurally colored scales. Figure adapted from Ref. [13].

tures varying in configurations and functions appear in a very wide range of biological objects from crabs to 500 million years old fossil animals [11].

1.2   Photonic Crystals with a Dirac Spectrum

Two-dimension triangular lattice photonic crystals with inversion symmetry have been studied extensively [1, 14, 15, 16, 17, 18]. Their crystal structure can be represented as a two-dimensional triangular[1] underlying Bravais lattice and a basis where points are placed in such a way that inversion symmetry of the lattice is present. Examples are the triangular, hexagonal, and kagome lattices shown in Fig. 1.5. They have, respectively, one-point, two-point and three-point bases. The interest in these lattices stems from the fact that they have a wide band gap with relatively large

---

[1]sometimes also called hexagonal in the literature
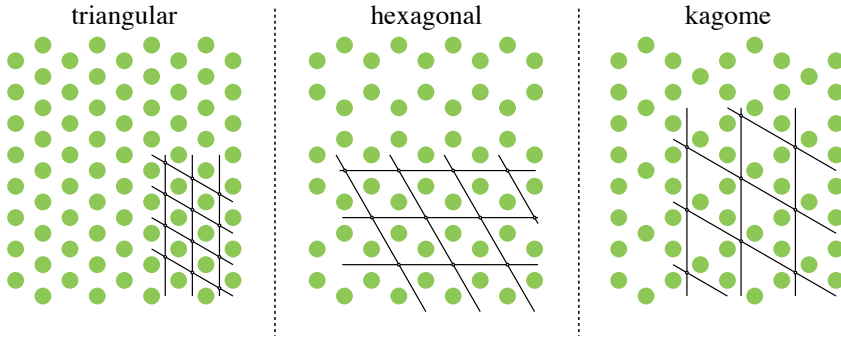
Figure 1.5. Top view of two-dimensional photonic crystals formed by parallel dielectric rods possessing triangular and inversion symmetries: triangular, hexagonal and kagome lattices. The triangular Bravais lattice is shown in black in the right bottom corner of each lattice.
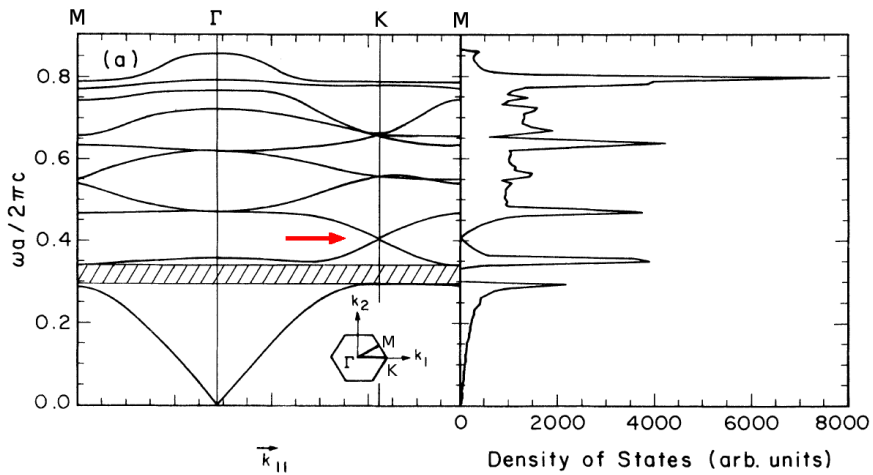
Figure 1.6. Plot of TE band structure and density of states of a triangular lattice photonic crystal formed by dielectric rods in vacuum with $\epsilon = 14$ and occupying a fraction $f = 0.431$ of the unit cell area. The Dirac point is indicated by a red arrow. Adapted from Ref. [14].

gap-to-midgap ratio, which in most cases overlaps for TE and TM modes. Photonic crystals with these lattices have also attracted interest because they exhibit negative refraction [19, 20, 21, 22, 23, 24, 25].

Another peculiar feature in their band structure has received much less attention. As indicated by the red arrow in Fig. 1.6, the band struc-
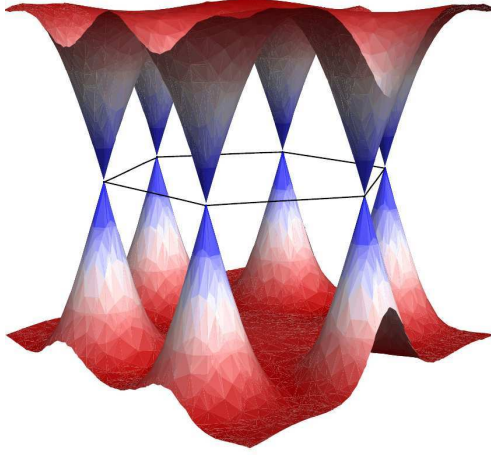
Figure 1.7. Plot of second and third TE bands (frequency (vertical) versus two-dimensional momentum) from Fig 1.6. The hexagonal Brillouin zone is shown in black. Picture by courtesy of M. J. A. de Dood.

ture has a conical singularity with linearly vanishing density of states and linear dispersion in its vicinity (see Fig. 1.7 for a full three-dimensional image of the touching bands). This singularity or Dirac point in a photonic system did not attract any attention before the seminal work of F. D. M. Haldane and S. Raghu[2] [28, 29]. In analogy with the "nearly-free electron" approximation the authors considered an approximation in which a two-dimensional "free photon" spectrum is perturbed by a weak periodic triangular modulation of the dielectric constant. They have shown within this so-called "nearly-free photon" approach that close to a corner of the hexagonal first Brillouin zone $\boldsymbol{K}$ or $\boldsymbol{K'}$ a pair of almost degenerate envelope Bloch modes is governed by the two-dimensional massless Dirac equation

$$v_D \left(-i\sigma_x \frac{\partial}{\partial x} - i\sigma_y \frac{\partial}{\partial y} \right) \Psi = \left(\omega - \omega_D \right) \Psi, \tag{1.1}$$

---

[2]In contrast, Dirac points in the electronic system of graphene were studied theoretically since 1947 [26] and experimentally since the discovery of carbon monolayers in 2004 [27].
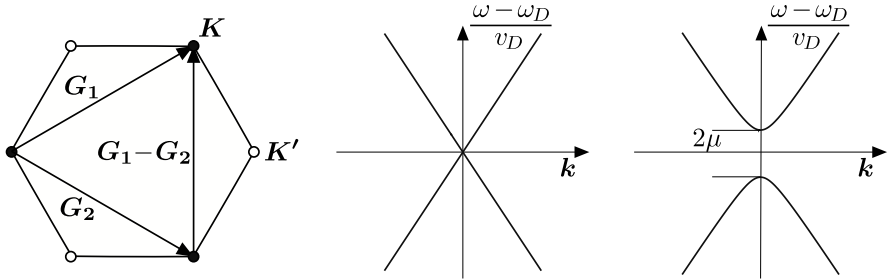
Figure 1.8. Left panel: Brillouin zone of triangular, hexagonal or kagome lattice; inequivalent corners are denoted K and K'; equivalent corners are related by the reciprocal lattice vectors G_i, ($i = 1, 2$). Middle panel: dispersion relation (1.2) of the massless Dirac equation (1.1). Right panel: dispersion relation (1.4) of the Dirac equation (1.3) with a mass term.

where σ_x, σ_y are Pauli matrices. The corresponding dispersion relation

$$(\omega - \omega_D)^2/v_D^2 = k_x^2 + k_y^2 \qquad (1.2)$$

and the Brillouin zone are shown in the middle and left panels of Fig. 1.8, respectively. The degeneracy frequency (= Dirac frequency) ω_D and the velocity v_D depend on the photonic crystal parameters. These include the dielectric constant of rods/holes and the filling fraction of rods/holes (= the fraction of the unit cell area they occupy). In the "nearly-free photon" approximation the approximate values of ω_D and v_D are given by $\omega_D \approx c|K| = c|K'|$ and $v_D \approx c/2$, where c is the speed of light. These simple estimates compare reasonably well with the numerically computed values (see chapters 3 and 4).

Broken time-reversal or inversion symmetry leads to a mass term and Eq. (1.1) for the envelope Bloch states modifies to

$$v_D \left(-i\sigma_x \frac{\partial}{\partial x} - i\sigma_y \frac{\partial}{\partial y} + \mu\sigma_z \right) \Psi = (\omega - \omega_D) \Psi. \qquad (1.3)$$

The resulting spectrum

$$(\omega - \omega_D)^2/v_D^2 = \mu^2 + k_x^2 + k_y^2 \qquad (1.4)$$

is shown in the right panel of Fig. 1.8. The ratio $\mu/|K| = \mu/|K'|$ is

determined by the strength of the symmetry breaking and characterizes
the splitting of degeneracies at the Brillouin zone corners.

There are two inequivalent K points in the Brillouin zone that are
not related by the reciprocal lattice vectors (see the left panel of Fig. 1.8).
They are also often called K and K' valleys. Equations (1.1) and (1.3) are
single-valley equations: they give an effective description in the vicinity of
either the K or K' points. In an ideal bulk crystal the wave propagation
in K and K' valleys is independent, however, the presence of disorder on
the scale of lattice spacing or crystal edges can cause changes of wave vec-
tor that are large enough to scatter from one valley to the other. Disorder
which is sufficiently smooth on the scale of the lattice constant produces
only weak intervalley scattering. The reason for that is, that such disor-
der results in a smooth potential term in the Dirac equation. The Fourier
transform of such a smooth potential has predominantly wave vector com-
ponents that are smaller than the difference between K and K' points.

In general there exist three types of disorder. First, scalar disorder
originating from changes of the dielectric constant of the material or fill-
ing fraction. This introduces a scalar potential term in the Dirac equation
and can be also thought of as a local change of Dirac frequency. Ef-
fects of scalar disorder on the coherent backscattering are investigated in
chapter 5. Second, random mass disorder originating from locally broken
time-reversal or inversion symmetry. Third, random vector potential dis-
order originating from local changes of the lattice spacing. The second
and third types of disorder are not considered in this thesis. It should
be stressed that we consider macroscopic disorder because microscopic
disorder in the material that forms the photonic crystal has no effect on
the electromagnetic wave propagation through the photonic crystal in the
range of frequencies of the linear spectrum.

The presence of the degeneracies at the Brillouin zone corners is as-
sured by the symmetries of the lattice [28, 29]. It is not guaranteed, how-
ever, that there will not be other states near the Dirac frequency in the
interior of the Brillouin zone. It is neither guaranteed that the frequency
range of the linear part of the spectrum around the Dirac point will not
be very small in comparison with the Dirac frequency. We need photonic
crystals with well isolated Dirac points and appreciable frequency range of

linear spectrum in their vicinity. Such photonic crystals we call photonic crystals with a Dirac spectrum. Figures 1.6 and 1.7 show an example of a band structure of such a crystal. By numerical trial and error we know that for a photonic crystal formed by dielectric rods organized in a triangular lattice there is an appreciable range of parameters within which there exists a well-developed and isolated Dirac spectrum for TE modes.

1.3 Graphene

As was explained in section 1.1, photonic crystals are optical analogs of real atomic crystals. Therefore it is reasonable that significant progress in the field of photonics has been achieved by exploiting similarities with electronics. Photonic crystals with a Dirac spectrum are not an exception: a large part of the ideas and developments presented in chapters 2, 3, 4, and 5 of this thesis concerning photonic crystals is inspired by the recent advances in the electronic system of graphene. Graphene possesses similar peculiar properties — the dynamics of electrons is described by the two-dimensional Dirac equation. In chapter 6 we demonstrate that the analogy between the two systems works the other way around as well. The Goos-Hänchen effect, which plays an important role in photonic crystals and metamaterials, can also be relevant for graphene.

Graphene is a single layer of carbon atoms forming a hexagonal lattice. It can be also thought of as a single layer of graphite, which consists of a stack of atomic layers of hexagonal lattices. The property of the monolayer are, however, completely different from the multilayer, because the two-dimensionality of the dynamics in a single layer is obscured in graphite by hopping between the layers. Schematic and experimental images of graphene are shown in the left and middle panels of Fig. 1.9, respectively.

Graphene has been studied since the middle of the 20th century, either as a building block of graphite, or for its own theoretical interest [26, 32, 33, 34, 35]. There were strong objections against the existence of graphene as a stable form of carbon. It was shown theoretically that two-dimensional crystals cannot be realized because thermal fluctuations at any finite temperature would destroy long-range order [36, 37, 38, 39, 40, 41, 42]. Experimental studies of thin films confirmed
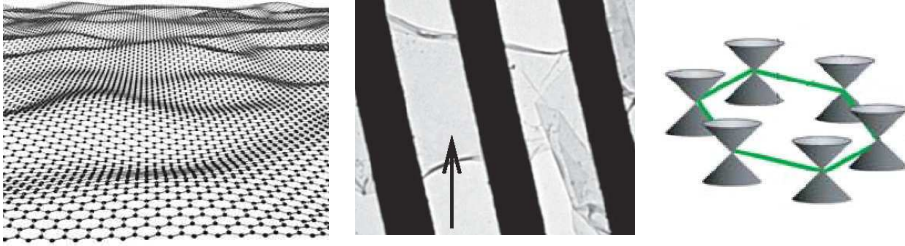
Figure 1.9. Left panel: artists impression of a corrugated graphene sheet by Jannik Meyer. Middle panel: Bright-field transmission electron microscope image of a suspended graphene membrane. A homogeneous and featureless region of a monolayer graphene is indicated by an arrow; image adapted from Ref. [30]. Right panel: Brillouin zone of graphene with a linear double cone spectrum at its corners; picture adapted from Ref. [31].

the theory. It was demonstrated that films below a certain thickness become thermodynamically unstable – they segregate into islands or decompose [43, 44, 45]. However in 2004 a group from Manchester University led by A. K. Geim reported a successfull fabrication of graphene [27]. In order to prove that graphene as a two-dimensional crystal can be stable without a substrate they also fabricated a suspended graphene sheet [30], shown in the middle panel of Fig. 1.9. They have shown that suspended graphene is rippled with the wavelength of ripples being much larger than the interatomic distance. The suspended graphene sheet thus is not perfectly flat. This observation is in accordance with further theoretical analysis which proved the possibility of existence of nearly flat two-dimensional crystals [46, 47, 48].

The experimental breakthrough of the successful fabrication of graphene triggered enormous interest of both experimentalists and theorists in the past few years, resulting in a large number of scientific publications that is still growing very rapidly. Such an interest is caused by the fact that graphene offers great possibilities for scientific and technological developments, ranging from measurements of fine structure constant [49] to detection of individual molecules [50] and hydrogen storage [51]. For reviews of recent advances in the field of graphene see [52, 53, 54, 55]

The hexagonal or honeycomb lattice of graphene is a triangular Bravais

lattice with two-point basis (or two atoms in the unit cell), as shown in the middle panel of Fig. 1.5. Hence the symmetry considerations of section 1.2 concerning triangular lattices can be applied to graphene. The Brillouin zone with two inequivalent K points is shown in the left panel of Fig. 1.8. Using the tight-binding model it can be shown that graphene has a linear double cone spectrum with a singularity (= Dirac point or neutrality point) at the K points of the Brillouin zone (see right panel of Fig. 1.9). The effective single-valley equation describing the envelope wave function is the massless two-dimensional Dirac equation

$$v_D \left(-i\sigma_x \frac{\partial}{\partial x} - i\sigma_y \frac{\partial}{\partial y} + V \right) \Psi = \epsilon \, \Psi. \tag{1.5}$$

Here σ_x, σ_y are Pauli matrices, V is an electric potential, the velocity $v_D \approx c/300$, where c is the speed of light. The Fermi level in undoped graphene lies exactly through the Dirac point, so the Fermi surface is just formed of the two points at K and K'.

Two atoms in the unit cell (see the middle panel of Fig. 1.5) form two independent triangular sublattices — not related by the lattice vectors. These sublattices are usually denoted as A and B. The two components of the spinor wave function from Eq. (1.5) can be interpreted as amplitudes of the envelope wave on A and B sublattices. Although the left hand side of Eq. (1.5) has the form of a spin-orbit coupling term, $\boldsymbol{\sigma} = (\sigma_x, \sigma_y)$ is not the real spin of the electron. This so-called "pseudospin" originates from the orbital motion in the periodic potential of the honeycomb lattice. The real spin of the electron is decoupled from the dynamics.

Despite the fact that the excitations in graphene and in photonic crystals with a Dirac spectrum obey the same two-dimensional Dirac equation, there is an essential difference between these excitations. Electrons in graphene are fermions due to the real spin while in the photonic crystals photons are bosons, even though they effectively have spin-$\frac{1}{2}$. This does not violate the Pauli theorem which relates spin and statistics because the effective Dirac equation is an approximate equation, which only holds in the long-lenght limit. To describe the statistics of the system we would need to quantize the fundamental equation. These are Maxwell's

equations in the case of photonic crystals and the four-dimensional Dirac equation in the case of electrons.

1.4 Numerical Calculations

Our understanding of photonic crystals with a Dirac spectrum is based on the effective Dirac equation. To test the accuracy of this description for realistic parameter values, we performed numerical simulations based on first principles, by solving full Maxwell's equations. Such a numerical experiment helps to convince ourselves and others of the validity of our analytical predictions, but it cannot replace a real experiment. In particular, in our numerics we assume complete translational invariance in the direction perpendicular to the crystal plane, while a real experiment would include the effects of a finite length in the perpendicular direction.

There are two types of problems we need to solve. First, the problem to determine the transmission and reflection spectra, that is the transmission and reflection as a function of frequency. Second, the eigenvalue problem to figure out the band structure and extract parameters of the spectrum: Dirac frequency, Dirac velocity and mass. In the following two subsections we describe the methods employed for solving these two problems along with the software packages used.

1.4.1 Time-domain

Time-domain numerical methods for electromagnetic calculations simulate full time-dependent Maxwell's equations. That is they simulate the evolution of the spatial dependence of the fields as it changes with time. This allows to obtain the transmission and reflection spectra in a single run by simulating the propagation of a Gaussian pulse through a structure.

Finite-difference time-domain method

The most widely used technique for time-domain simulations is the finite-difference time-domain method (FDTD). The details of the FDTD method are described in Ref. [56]. Here we explain this method for a particular case of two-dimensional transverse electric (TE) modes propagating in

some linear nondispersive isotropic nonmagnetic material, i.e. a material characterized by a scalar spatially dependent dielectric function ϵ.

By two-dimensional we mean that the structure is translationally invariant along one direction (z direction). Assuming also that the incident wave has no wave vector component in the z direction, this implies that the fields cannot change along the z direction. Therefore we set to zero all spatial derivatives of the fields with respect to z. Then Maxwell's curl equations for TE modes reduce to

$$\frac{\partial E_x}{\partial t} = \frac{1}{\epsilon}\frac{\partial H_z}{\partial y}, \tag{1.6}$$

$$\frac{\partial E_y}{\partial t} = -\frac{1}{\epsilon}\frac{\partial H_z}{\partial x}, \tag{1.7}$$

$$\frac{\partial H_z}{\partial t} = \frac{\partial E_x}{\partial y} - \frac{\partial E_y}{\partial x} - \tilde{J}_z. \tag{1.8}$$

Here E_x and E_y are, respectively, the x and y components of the electric field, H_z is the z component of the magnetic field, $\tilde{J}_z$ is a magnetic charge current density. The latter quantity is a convenient computational way to mimic a source of TE modes.

This system of equations is discretized using central-difference second-order accurate approximations to the space and time derivatives on a Yee lattice (or Yee mesh), shown in Fig. 1.10, and solved according to the Yee algorithm (after seminal work by Kane Yee [57]). As indicated in Fig. 1.10, every electric field component is surrounded by two circulating magnetic field components and every magnetic field component is surrounded by four circulating electric field components. A point denoted (i, j) on the Yee lattice corresponds to the spatial coordinate $(i\Delta, j\Delta)$, where Δ is a lattice space increment, i and j are integers. The electric field component E_x is stored for the locations $((i+1/2)\Delta, j\Delta)$, the electric field component E_y is stored for the locations $(i\Delta, (j + 1/2)\Delta)$ and the magnetic field component H_z is stored for the locations $((i + 1/2)\Delta, (j + 1/2)\Delta)$.

The time evolution is simulated in a so-called "leap-frog" scheme. That is, the electric field is computed at time t from the electric field at time $t - \Delta_t$ (Δ_t is a time step) and the magnetic field at time $t - \Delta_t/2$, then
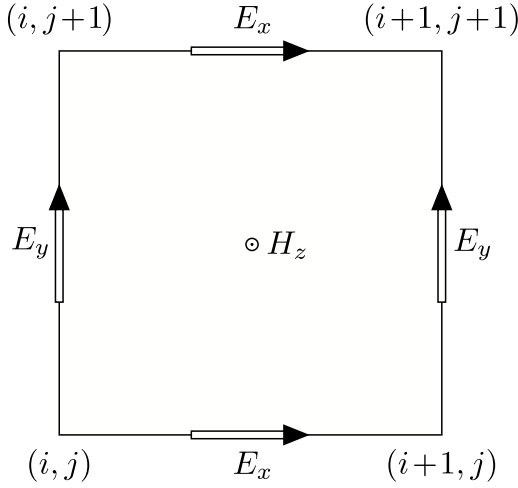
Figure 1.10. The two-dimentional Yee lattice used in the finite-difference time-domain calculations.

the magnetic field at time $t + \Delta_t/2$ is computed from the electric field at time t and the magnetic field at time $t - \Delta_t/2$.

We denote a function f at a discrete point in the Yee lattice and at a discrete point in time as $f(i\Delta, j\Delta, n\Delta_t) = f_{i,j}^n$. The central-difference second-order accurate in the space and time steps numerical approximation of Eq. (1.8) is given by

$$\frac{H_z|_{i,j}^{n+1/2} - H_z|_{i,j}^{n-1/2}}{\Delta_t} = \frac{E_x|_{i,j+1/2}^n - E_x|_{i,j-1/2}^n}{\Delta}$$
$$- \frac{E_y|_{i+1/2,j}^n - E_y|_{i-1/2,j}^n}{\Delta} - \tilde{J}_z|_{i,j}^n. \quad (1.9)$$

This expression is used to obtain the magnetic field at time step $n + 1/2$ from the magnetic field at time step $n - 1/2$, the electric field and the current density at time step n. The central-difference second order

accurate approximation of Eq. (1.6) and (1.7) gives

$$\frac{E_x|_{i,j}^{n+1} - E_x|_{i,j}^{n}}{\Delta_t} = \frac{1}{\epsilon_{i,j}} \frac{H_z|_{i,j+1/2}^{n+1/2} - E_x|_{i,j-1/2}^{n+1/2}}{\Delta}, \qquad (1.10)$$

$$\frac{E_y|_{i,j}^{n+1} - E_y|_{i,j}^{n}}{\Delta_t} = \frac{1}{\epsilon_{i,j}} \frac{H_z|_{i-1/2,j}^{n+1/2} - E_x|_{i+1/2,j}^{n+1/2}}{\Delta}. \qquad (1.11)$$

These equations provide the electric field at time step $n + 1$ from the electric fields at time step n and the magnetic field at time step $n + 1/2$. The simulation is stopped when a desired field configuration is reached or a certain condition is fulfilled.

It can be shown that the above described discretization on a Yee mesh implicitly enforces the other two Maxwell's equations [56]. The Yee lattice is, thus, divergence-free with respect to its electric and magnetic fields and thereby enforces the absence of free electric and magnetic charge in the source free space.

Implementation: MIT Electromagnetic Equation Propagation

We used the open source MIT Electromagnetic Equation Propagation (MEEP) software package to obtain a numerical solution of Maxwell's equations in time-domain. Detailed information about MEEP and a tutorial on its usage can be found on the MEEP website [58].

The usage of MEEP includes setting up a volume wherein the simulation is performed (computational cell or computational domain), adjusting boundary conditions on the edges of the computational domain and defining sources of electromagnetic radiation and regions where the flux or fields will be measured. When transmission calculations are carried out, a Gaussian pulse source is used in order to obtain the transmission in a frequency range. In this case MEEP saves the field values at every time step in some region behind the sample (a plane in three-dimensions), then Fourier transforms them and multiplies to obtain frequency dependent flux. The simulation is stopped after the pulse has propagated through the structure and a flux plane. The simulation is run again without the structure (normalization run) to get the incident flux, and, thus, obtain

the transmission (= ratio of transmitted and incident flux). If the reflectivity is computed as well, the fields from the normalization run are subtracted from the fields calculated in front of the sample to obtain only the fields of the reflected wave.

In addition to the FDTD method itself, MEEP incorporates other useful algorithms and features. We mention here those that we take advantage of.

The Bloch periodic boundary conditions can be imposed, i.e. any phase difference between two opposite boundaries of the computational domain can be adjusted.

One can simulate open boundary conditions by putting a perfectly matched layer [59] (PML) next to the boundary. The PML in theory absorbs without any reflection electromagnetic waves at all frequencies and angles of incidence. It can be formulated as a region with artificial anisotropic absorbing materials [60]. The discretization may cause some spurious reflection. Instead of using a PML for simulating open boundaries, one can alternatively set a large computational cell, if it is large enough so that the wave does not reach the end of the cell before the simulation stops. This would require, however, much more computer resources.

MEEP has an implementation of subpixel averaging (or subpixel smoothing) developed in Ref. [61]. Subpixel smoothing deals with one of the sources of errors in FDTD calculations — staircasing of dielectric materials interfaces due to discretization. The averaging greatly increases the accuracy of the FDTD method when discontinuous dielectric materials are modelled. Unfortunately, the subpixel averaging occasionally makes the numerical algorithm less stable. To make sure that we stay in the regime where instabilities are insignificant we perform a variety of consistency checks. These include a test for decay of the field after the pulse has propagated through the structure, a check for unitarity (transmission and reflection sum to unity) and a search for incipient instabilities in the entire computational domain. We also compared the results of simulations with and without the subpixel averaging.

As was explained above, in FDTD simulations the electric and magnetic fields are offset in time by one half of a time step $\Delta_t/2$. So when

the flux is computed at time step n, the electric field at time step n is multiplied by the magnetic field at time step $n - 1/2$. As a consequence, the flux is calculated with first-order accuracy, while the FDTD method is ideally second-order accurate. To improve the accuracy MEEP provides the possibility to synchronize the fields in time by calculating the magnetic field at time step $n + 1/2$ and taking arithmetic average of its values at times $t - \Delta_t/2$ and $t + \Delta_t/2$. This gives the magnetic field at time t to second-order accuracy in Δ_t. The discussed improvement comes in handy in chapter 5 (see Appendix 5.A) where we calculate the flux at some fixed time.

1.4.2   Frequency-domain

Time-domain methods can also be used for band structure calculations by looking at the response of a system to a short pulse. The eigenfrequencies produce peaks in the spectrum of the response. This method, however, has certain disadvantages. Resolving nearly degenerate peaks may take a long time. Additionally, the signal processing techniques involved in peak identification are not very reliable, they may miss eigenfrequencies or identify spurious ones. Frequency-domain eigensolvers are more robust and often faster.

In a system of linear nondispersive isotropic nonmagnetic materials, characterized by a scalar spatially dependent dielectric function ϵ, Maxwell's curl equations can be reduced to the equation for the magnetic field

$$\nabla \times \left(\frac{1}{\epsilon} \nabla \times \boldsymbol{H}(\boldsymbol{r}) \right) = \omega^2 \boldsymbol{H}(\boldsymbol{r}). \tag{1.12}$$

Here ω is the frequency and $\boldsymbol{H}(\boldsymbol{r})$ is the spatial mode profile. The time and space dependent field is given by the spatially dependent profile $\boldsymbol{H}(\boldsymbol{r})$ multiplied by a complex exponential:

$$\boldsymbol{H}(\boldsymbol{r}, t) = \boldsymbol{H}(\boldsymbol{r}) e^{-i\omega t}. \tag{1.13}$$

Along with the divergence equation

$$\nabla \cdot \boldsymbol{H}(\boldsymbol{r}) = 0 \tag{1.14}$$

Eq. (1.12) gives us all the information about the spatial profile $\boldsymbol{H}(\boldsymbol{r})$ of the magnetic field. Since Maxwell's curl equations relate the electric and the magnetic fields, knowing $\boldsymbol{H}(\boldsymbol{r})$ we can deduce the electric field pattern.

In a periodic system like a photonic crystal the Bloch theorem holds. It states that the field has the following form:

$$\boldsymbol{H_k}(\boldsymbol{r}) = e^{i\boldsymbol{kr}}\boldsymbol{u_k}(\boldsymbol{r}), \tag{1.15}$$

where $\boldsymbol{u_k}(\boldsymbol{r})$ is a periodic function on the lattice, that is

$$\boldsymbol{u_k}(\boldsymbol{r}) = u_k(\boldsymbol{r} + \boldsymbol{R}) \tag{1.16}$$

for any lattice vector $\boldsymbol{R}$. The wave vector $\boldsymbol{k}$ identifies the mode $\boldsymbol{H_k}$ with frequency $\omega(\boldsymbol{k})$. After inserting Eq. (1.15) into Eq. (1.12) we arrive at the eigenvalue problem

$$(i\boldsymbol{k} + \nabla) \times \left(\frac{1}{\epsilon}(i\boldsymbol{k} + \nabla) \times \boldsymbol{u_k}(\boldsymbol{r}) \right) = \omega^2 \boldsymbol{u_k}(\boldsymbol{r}) \tag{1.17}$$

of a Hermitian operator

$$\Theta_{\boldsymbol{k}} = (i\boldsymbol{k} + \nabla) \times \frac{1}{\epsilon}(i\boldsymbol{k} + \nabla) \times . \tag{1.18}$$

In addition $\boldsymbol{u_k}(\boldsymbol{r})$ must satisfy the transversality constraint originating from Eq. (1.14):

$$(i\boldsymbol{k} + \nabla) \cdot \boldsymbol{u_k}(\boldsymbol{r}) = 0 \tag{1.19}$$

The solution $\omega(\boldsymbol{k})$ of Eq. (1.17) as a function of the wave vector $\boldsymbol{k}$ is known as a band structure. Since the system is periodic the eigenvalue problem (1.17) can be thought of as being restricted to a single unit cell of the lattice. A Hermitian eigenvalue problem restricted to a finite volume has discrete eigenvalues. This means that at each $\boldsymbol{k}$ there is an infinite set of discrete frequencies corresponding to a discrete set of bands.

We used the open source MIT Photonic Bands (MPB) software package to solve numerically the eigenvalue problem and determine the band structure of the systems we studied. The information about the MPB software and a tutorial are available on the MPB website [62]. The developers

summarize their method in one sentence, as "preconditioned conjugate-gradient minimization of the block Rayleigh quotient in a planewave basis". Below we explain briefly how this method works, for a more detailed description of the method implemented in MPB and its advantages we refer to Ref. [1].

MPB computes band structures and eigenmodes with a planewave method. The functions $u_k(r)$ are represented by a Fourier series

$$u_k(r) = \sum_G c_G(k)e^{iGr}.$$ (1.20)

Here the sum is over all the reciprocal vectors G and

$$c_G = \frac{1}{V} \int e^{-iGr} u_k(r) \, dr$$ (1.21)

with V being the unit cell volume. Fourier transform of the eigenvalue problem leads to an infinite set of equations for c_G. Truncation of this set of equations gives a finite generalized eigenproblem:

$$Ax = \omega^2 Bx,$$ (1.22)

where A and B are matrices and x is the eigenvector. The smallest eigenvalue ω_0^2 satisfies

$$\omega_0^2 = \min_x \frac{x^\dagger Bx}{x^\dagger Ax}.$$ (1.23)

This is known as Rayleigh-quotient minimization. The minimizing value x_0 is the eigenvector. The minimization is done using a preconditioned nonlinear conjugate-gradient method [63]. To find the next eigenvalue the same Rayleigh quotient is minimized with an orthogonality constraint imposed on x ($x^\dagger Bx_0=0$). This process is repeated to find other subsequent eigenvalues.

1.5 Berry Phase

In chapters 4 and 5 of this thesis we repeatedly employ the concept of Berry phase [64] (or geometric phase). Here we would like to give a brief
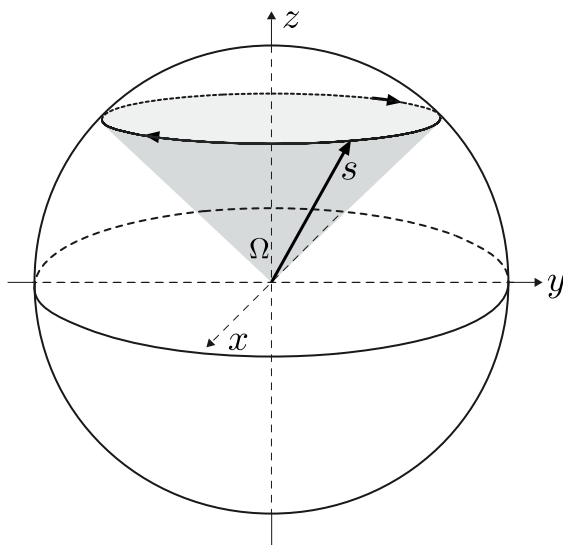
Figure 1.11. The rotating spin s subtends a solid angle Ω.

overview of this concept: we present a definition of a Berry phase to-
gether with basic formulas without detailed derivation. At the end we
give a simple instructive example very closely related to our further con-
siderations. An interested reader may consult Ref. [65] for seminal papers
or use Ref. [66] as a guide to literature; for an elementary introduction to
the subject we recommend chapter 10 from a book by Griffiths [67].

   We follow Berry's introduction of the geometric phase in the context
of quantum mechanics, as it was formulated by him in 1983 for the first
time in a generalized way in his famous work [64]. There were many
"anticipations" (as Berry calls them in his article on a history of the
geometric phase [68]) of this formulation. In fact the first "anticipations"
of a geometric phase were works by Soviet physicists in 1938 and in 1941
in the field of optics [69].

   Suppose the Hamiltonian of a quantum system $H(t)$ depends on some
parameters $R_i(t)$ (where $i = 1, 2, 3, \ldots, N$) that are changing gradually
with time. Consequently, the eigenfunctions and eigenvalues also depend
on time. We assume for simplicity the spectrum to be discrete and non-
degenerate:

$$H(t)\psi_n(t, x) = E_n(t)\psi_n(t, x). \qquad (1.24)$$

Gradual change of the parameters means that they vary with time much slower than the internal dynamic variables. As an example from classical physics one may think of a pendulum placed on an oscillating support with the period of oscillations being much greater than that of the pendulum.

Under this assumption the adiabatic theorem holds. It states that the system in the nth eigenstate will remain in the same n^{th} eigenstate during the time evolution, that is

$$\Psi_n(t, x) = \psi_n(t, x) e^{-i \int_0^t E_n(\tau)\, d\tau} e^{i\Gamma}. \tag{1.25}$$

In this expression the term $\int_0^t E_n(\tau)\, d\tau$ is known as the dynamic phase. The additional phase factor Γ is called the geometric phase.

If the Hamiltonian follows a closed path in parameter space and returns to its initial form after a time T, then the geometric phase is given by the line integral around a closed path in parameter space:

$$\Gamma = \Gamma_n(T) = i \oint \langle \psi_n | \nabla_R \psi_n \rangle\, d\boldsymbol{R}. \tag{1.26}$$

It can be shown that $\Gamma_n(T)$ does not depend on the elapsed time T. It is real and it equals to zero if the parameter space is one dimensional.

In many cases the geometric phase appears in quantum mechanics and in optics when the spin sweeps out some solid angle Ω (see Fig. 1.11). Then the geometric phase is given by the product of the spin s and the solid angle:

$$\Gamma = -s\,\Omega. \tag{1.27}$$

Let us consider an example of a massive spin-$\frac{1}{2}$ particle governed by the two dimensional Dirac equation

$$H\Psi = \varepsilon\Psi, \ \ H = -i\sigma_x \frac{\partial}{\partial x} - i\sigma_y \frac{\partial}{\partial y} + \mu\sigma_z, \tag{1.28}$$

where σ_x, σ_y and σ_z are Pauli matrices. The resulting dispersion relation is

$$\varepsilon^2 = \mu^2 + k_x^2 + k_y^2. \tag{1.29}$$

We calculate the Berry phase which is accumulated by the particle
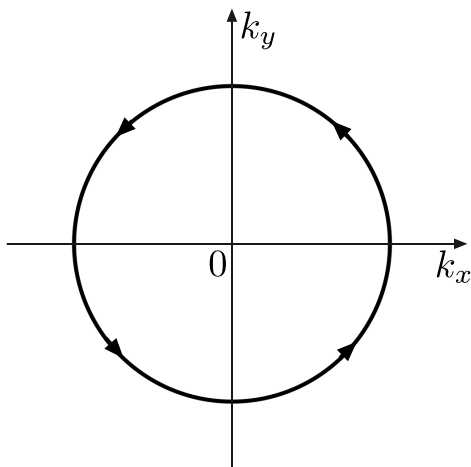
Figure 1.12. A circle in momentum space corresponding to motion along a circle in real space.

after one 360 degree rotation in the $x - y$ plane. A loop in parameter space, which is in this case the momentum space, is shown in Fig. 1.12. We insert the solution of equation (1.28) with well-defined momentum

$$\Psi(x, y) = \frac{1}{\sqrt{2\varepsilon(\varepsilon + \mu)}} \begin{pmatrix} \varepsilon + \mu \\ k_x + ik_y \end{pmatrix} e^{ik_x x + ik_y y} \qquad (1.30)$$

into the general formula for the Berry phase (1.26) and get:

$$\Gamma = \frac{i}{2\varepsilon(\varepsilon + \mu)} \oint [(k_x - ik_y)\, dk_x + (ik_x + k_y)\, dk_y]$$
$$+ i \oint (ix\, dk_x + iy\, dk_y). \quad (1.31)$$

The second term in this expression comes from taking a derivative of the exponential factor of Eq. (1.30). It equals to zero because it is a line integral along a circuit of a 'constant' vector (independent on the integration variable). The first term gives the following expression for the Berry phase:

$$\Gamma = -\pi \frac{\varepsilon - \mu}{\varepsilon}. \qquad (1.32)$$

In the ultrarelativistic or zero mass limit $\varepsilon \gg \mu$ the geometric phase is equal to $-\pi$. This result becomes obvious if we notice that the spin follows the direction of motion when the mass is zero, thus sweeping out the solid angle of 2π, and use formula (1.27).

In the nonrelativistic or zero kinetic energy limit $\varepsilon \approx \mu$ the Berry phase is zero. Indeed, the solid angle swept by the spin is zero because it is decoupled from the motion and points always in the same direction.

Analyzing this example one may ask about the validity of the adiabatic approximation. The answer is that adiabaticity is not required here as there is not any external parameter varying with time. Formally speaking the geometric phase accumulated by the particle in the example above should not be called Berry phase, because the Hamiltonian does not change with time. We use the term Berry phase as an equivalent to geometric phase following modernly accepted terminology.

Let us elaborate a little on the relevance of the adiabatic approximation for the geometric phase. Consider the classic example of the Berry phase [64]: the direction of the magnetic field changes with time, while its magnitude remains constant, and eventually returns to its initial configuration; the spin of a particle which starts out with spin up (along the magnetic field) follows the magnetic field and the wave function acquires the geometric phase given by Eq. (1.27). In this case the external magnetic field should change adiabatically: the rotation frequency of the magnetic field should be much smaller than the frequency associated with the coupling energy of the spin with the magnetic field. The classical analog of that condition would be a magnetic moment in a strong slowly rotating magnetic field, such that the magnetic moment is always aligned with the magnetic field pointing in the same direction.

In contrast in the example above the changing parameter is the momentum of the particle. One could think of a constant external magnetic field causing this change. Alternatively, one can think of a particle that makes a loop due to reflections and refractions like in the case studied in chapter 4. The geometric phase acquired by the wave function after one full rotation is also given by Eq. (1.27). However in this case the Hamiltonian is independent on time thus the adiabaticity is not required. In

other words the spin is tied to the momentum which is not an external parameter.

The presence of the mass term does not decouple the spin from the momentum. The mass only makes the spin rotate out of the x-y plane while its projection on the x-y plane still follows the momentum. Having realized this, the expression for the Berry phase (1.32) could have been simply derived using formula (1.27) and employing geometrical considerations. The solid angle is given by $\Omega = 2\pi(1 - \cos\theta)$. Here θ is the angle between the spin and the z axis and its cosine is given by the ratio between the mass and the energy μ/ε. Collecting these formulas together we recover the same result (1.32).

1.6 Outline of This Thesis

At the end of this introductory chapter we present an overview of the remaining chapters.

Chapter 2: Extremal Transmission at the Dirac Point of a Photonic Band Structure

In this chapter we consider transport of electromagnetic waves through a photonic crystal with a Dirac spectrum in the range of frequencies where the spectrum is linear. We calculate the effect of a Dirac point on the transmission through a photonic crystal.

In free space outside the crystal the electromagnetic wave obeys the Helmholtz equation whereas inside it is governed by the Dirac equation. We match the solutions of these two equations at the interfaces between free space and the photonic crystal by means of interface matrices. These matrices describe how strongly the plane wave outside is coupled to the Bloch wave inside, or in other words they describe the transparency of the interfaces, and depend on the termination of the photonic crystal. In this chapter the interface matrices remain undetermined (they are only constrained by the current conservation) allowing us to obtain general results that remain valid for any termination of the crystal.

The central result of this chapter is the "pseudo-diffusive" $1/L$ scaling

law for the transmitted photon current at the Dirac point

$$I = I_0 \Gamma_0 \frac{W}{L}, \ \ 0 < \Gamma_0 < \frac{1}{\pi}. \tag{1.33}$$

Here I_0 is the incident current per mode, W and L are the width and the length of the sample respectively. The slope prefactor Γ_0 is a function of interface matrices and thus contains information concerning the transparency of the interfaces. For the ideal matching when the interface matrices are just identity matrices we have $\Gamma_0 = 1/\pi$.

Additionally the assumption that the two interfaces are related by reflection symmetry leaves us with only two undetermined parameters in the transmission amplitude as a function of frequency of the incident wave. These parameters are calculated numerically in chapter 3 for some particular cases.

Knowing that the modes are evanescent at the Dirac point one might have expected exponential decay of the transmitted current as a function of sample length — the same as for a stopband (bandgap). On the contrary, for a passband the transmitted current does not depend on the length. It turns out that the Dirac point is a special point of a band structure which can be attributed to neither a passband nor to a stopband. It produses an unusual $1/L$ scaling law resembling diffusive transmission through a disordered medium.

Chapter 3: Numerical Test of the Theory of Pseudo-diffusive Transmission at the Dirac Point of a Photonic Band Structure

The purpose of this chapter is to perform a quantitative numerical test of the predictions of chapter 2 from first principles (solving full Maxwell's equations) without making the approximation of the Dirac equation.

By fitting the calculated transmission as a function of frequency at a fixed value of transverse wave vector to the analytical result (2.27) we extract the interface parameters which were previously left undetermined as they are beyond the description based on the Dirac equation. First we confirm the validity of the assumption made in chapter 2 concerning the independence of the interface parameters on the transverse wave vector: we show that the same set of parameters also describes the frequency de-

Figure 1.13. A photograph of a photonic crystal fragment from an ongoing experiment. The experiment is performed in the group of M. J. A. de Dood at the University of Leiden and aims, in particular, to test for $1/L$ scaling. Photograph by courtesy of M. J. A. de Dood.

pendence of the transmission probability for other values of the transverse wave vector.

Then we consider a range of incident transverse wave vectors to demonstrate the $1/L$ scaling predicted in chapter 2. We observe a clear $1/L$ scaling with slope coefficient $\Gamma_0 = 0.30$. The obtained slope is only 6% smaller than the maximal value $\Gamma_0 = 1/\pi$ reached for an ideal interface.

Further we repeat the calculations for different realizations of triangular lattice photonic crystal changing the dielectric constant of the rods and the filling fraction. In every case we arrive at the $1/L$ scaling with a slope coefficient Γ_0 that stays within 8% of the maximal value $1/\pi$. This demonstrates that nearly ideal interfaces are a generic property of these types of crystals.

We show in this chapter a good agreement between numerical results and analytical theory based on the Dirac equation. This fully justifies the applicability of the Dirac equation to a photonic crystal with a Dirac spectrum.

Figure 1.13 shows a fragment of a photonic crystal from an ongoing

experiment by the group of M. J. A. de Dood aimed, in particular, to test for $1/L$ scaling. Preliminary experimental data demonstrate the predicted $1/L$ behavior. The slope Γ_0, however, has not been determined yet.

Chapter 4: How to Detect the Pseudospin-$\frac{1}{2}$ Berry Phase in a Photonic Crystal with a Dirac Spectrum

In the previous chapters we confirm and justify the usage of the Dirac equation in describing transport properties of a photonic crystal with a Dirac spectrum. One rather important feature of the Dirac equation we investigate in this chapter is that it provides a description of particles with spin-$\frac{1}{2}$. This spin-$\frac{1}{2}$ degree of freedom in the case of photonic crystal emerges from orbital motion in the periodic dielectric medium and is therefore called pseudospin.

The pseudospin-$\frac{1}{2}$ can manifest itself by producing the Berry phase upon sweeping out some solid angle Ω (see Fig. 1.11). The Berry phase is given by the product of the spin s and the solid angle it sweeps out

$$\Gamma = -s\,\Omega. \tag{1.34}$$

Normally, when time reversal and inversion symmetries are present, the excitations in a photonic crystal with a Dirac spectrum are governed by the massless two-dimensional Dirac equation. It implies that the pseudospin follows the direction of motion and thus to make the pseudospin execute a closed path we need to make a photon execute a closed path. Such a path in general will also contain a large unspecified dynamical phase, which will obscure the Berry phase. In this chapter we show how complementary media can be used to eliminate the dynamical phase, allowing us to isolate the Berry phase.

The complementary media are isolated from free space by two gap regions. The gap regions are created by breaking the inversion symmetry of the crystal. This produces a mass term in the Dirac equation. A transmission minimum at the complementarity frequency arises as a direct consequence of the geometric phase shift of π acquired by rotation of the pseudospin over $360°$ around a perpendicular axis. We also show a
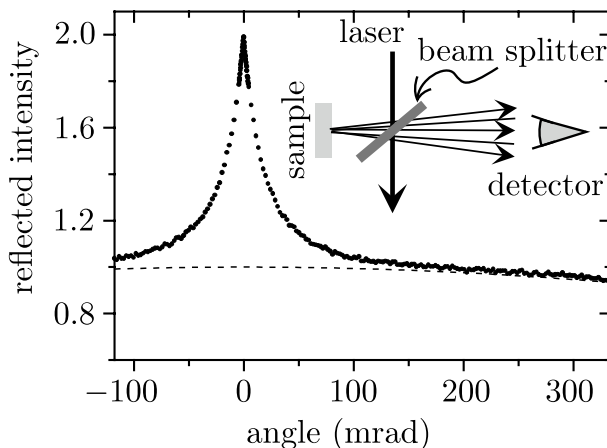
Figure 1.14. Measurement of coherent backscattering from a ZnO powder. The sample is rotated to average the reflected intensity, which is plotted against the scattering angle. The measured peak due to coherent backscattering is superimposed on the diffuse scattering intensity (dashed curve, normalized to unity in the backscattering direction at zero angle). The relative height of the peak is a factor-of-two. The angular width is of order $1/kl \approx 40\,\mathrm{mrad}$, for wave length $\lambda = 2\pi/k = 514\,\mathrm{nm}$ and mean free path $l = 1.89\,\mu\mathrm{m}$. The inset shows the optical setup. Use of a beam splitter permits detection in the backscattering direction, which would otherwise be blocked by the incident laser beam. Adapted from Ref. [70].

change from a minimum to a maximum when complementarity is broken by flipping the sign of the mass in one of the gap regions.

We support our analytical theory based on the Dirac equation by a numerical solution of full Maxwell's equations.

Chapter 5: Extinction of Coherent Backscattering by a Disordered Photonic Crystal with a Dirac Spectrum

We consider coherent backscattering from a two-dimensional triangular lattice photonic crystal with a Dirac spectrum. Elaborating on our previous findings we show here that the half-integer spin and the associated Berry phase remain observable in the presence of disorder in the crystal.

A pair of reciprocal waves, related by time reversal symmetry, arrive at an observer with a phase difference equal to a geometric phase acquired

by them. In the scalar case the geometric phase is zero and therefore a pair of reciprocal waves interfere constructively. This can be observed as a peak in the angular profile of the reflected intensity (see Fig. 1.14). The peak is in the backscattering direction, so this effect is called "coherent backscattering" [71, 72, 73, 74]. In our case of pseudospin-$\frac{1}{2}$ particles the geometric phase difference of π between the two reciprocal waves switches constructive interference to destructive interference leading to an extinction of coherent backscattering — a dramatic change from a peak to a dip with zero intensity. An analogous effect was predicted in 2005 by Bliokh [75] for scattering of ultrarelativistic electrons from a disordered medium.

By including the Berry phase in the theory for scattering of scalar waves we construct an analytical theory for the extinction of coherent backscattering. We confirm our analytical results with a numerical solution of full Maxwell's equations.

Chapter 6: Quantum Goos-Hänchen Effect in Graphene

In contrast to the preceding chapters, in this chapter the analogy between optical and electronic systems works the other way around. Here we show that the Goos-Hänchen effect (a wave effect on total internal reflection at an interface, resulting in a shift of the trajectory along the interface) observed for the first time in optics can be realized in graphene, at interfaces between n-doped and p-doped regions.

We calculate the general formula for the Goos-Hänchen shift in terms of the reflection amplitude. Further we compute the Goos-Hänchen shift upon reflection from n-n and p-n interfaces in graphene and demonstrate that for the n-n interface the Goos-Hänchen shift is always positive meaning that the wave is shifted in the forward direction whereas for the p-n interface it can be positive or negative depending on the angle of incidence. A negative Goos-Hänchen effect results in a bound state which becomes apparent as a minimum in the dispersion relation.

By means of an analytical theory we predict that in an n-doped channel with p-doped boundaries the Goos-Hänchen effect doubles the degeneracy of the lowest propagating mode, introducing a two-fold degeneracy on top of the usual spin and valley degeneracies. This can be observed as a

stepwise increase by $8e^2/h$ of the conductance with increasing channel width. We confirm this prediction by performing numerical simulations of electrical conduction in a tight binding model of a graphene sheet covered by a split-gate electrode.

Chapter 2

Extremal Transmission at the Dirac Point of a Photonic Band Structure

2.1 Introduction

In a two-dimensional photonic crystal with inversion symmetry the band gap may become vanishingly small at corners of the Brillouin zone, where two bands touch as a pair of cones. Such a conical singularity is also referred to as a Dirac point, because the two-dimensional Dirac equation has the same conical dispersion relation. In a seminal work [28, 29], Raghu and Haldane investigated the effects of broken inversion symmetry and broken time reversal symmetry on the Dirac point of an infinite photonic crystal. Here we consider the transmission of radiation through an ideal but finite crystal, embedded in free space.

As we will show, the proximity to the Dirac point is associated with an unusual scaling of the transmitted photon current I with the length L of the photonic crystal. We assume that L is large compared to the lattice constant a but small compared to the transverse dimension W of the crystal. For a true band gap, I would be suppressed exponentially with increasing L when the frequency ω lies in the gap. Instead, we find that near the Dirac point $I \propto 1/L$. The $1/L$-scaling is reminiscent of
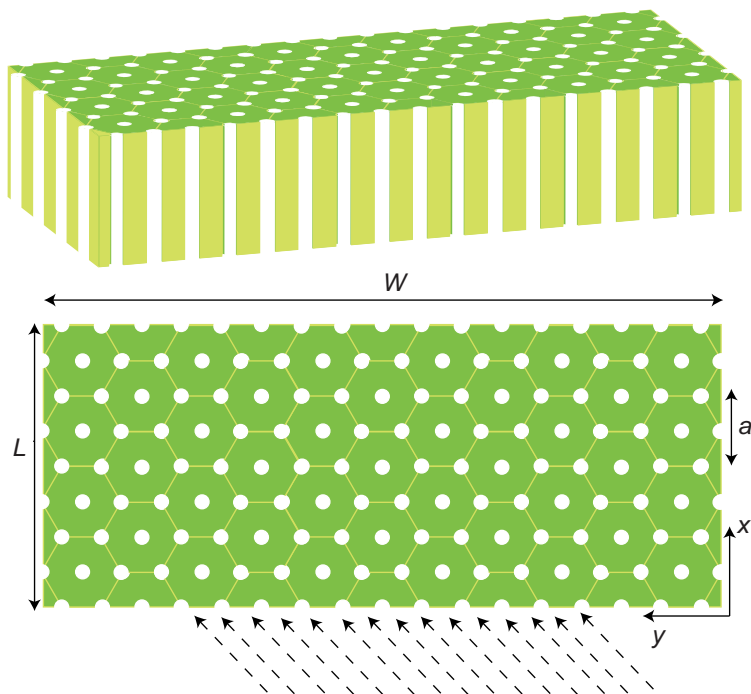
Figure 2.1.   Photonic crystal formed by a dielectric medium perforated by parallel cylindrical holes on a triangular lattice (upper panel: front view; lower panel: top view). The dashed lines indicate the radiation incident on the armchair edge of the crystal, with the electric field polarized in the z-direction.

diffusion through a disordered medium, but here it appears in the absence of any disorder inside the photonic crystal.

Such "pseudo-diffusive" scaling was discovered in Refs. [76, 77] for electrical conduction through graphene (a two-dimensional carbon lattice with a Dirac point in the spectrum). Both the electronic and optical problems are governed by the same Dirac equation inside the medium, but the coupling to the outside space is different. In the electronic problem, the coupling can become nearly ideal for electrical contacts made out of heavily doped graphene [76, 77], or by suitably matching the Fermi energy in metallic contacts [50, 78]. An analogous freedom does not exist in the optical case.

The major part of our analysis is therefore devoted to the question how

nonideal interfaces affect the dependence of I on ω and L. Our conclusion is that

$$I/I_0 = \Gamma_0 W/L \qquad (2.1)$$

at the Dirac point, with I_0 the incident current per mode and Γ_0 an effective interface transparency. The properties of the interfaces determine the proportionality constant Γ_0, and they also determine whether I as a function of ω has a minimum or a maximum near the Dirac point, but they leave the $1/L$-scaling unaffected.

In Sec. 2.2 we formulate the wave equations inside and outside the medium. The Helmholtz equation in free space is matched to the Dirac equation inside the photonic crystal by means of an interface matrix in Sec. 2.3. This matrix could be calculated numerically, for a specific model for the termination of the crystal, but to arrive at general results we work with the general form of the interface matrix (constrained by the requirement of current conservation). The mode dependent transmission probability through the crystal is derived in Sec. 2.4. It depends on a pair of interface parameters for each of the two interfaces. In Sec. 2.5 we then show that the extremal transmission near the Dirac point scales $\propto 1/L$ regardless of the values of these parameters. We conclude in Sec. 2.6 with suggestions for experiments.

2.2   Wave Equations

We consider a two-dimensional photonic crystal consisting of a triangular or honeycomb lattice in the x-y plane formed by cylindrical air-filled holes along the z-axis in a dielectric medium (see Fig. 2.1). The crystal has a width W along the y-direction and a length L along the x-direction, both dimensions being large compared to the lattice constant a. Monochromatic radiation (frequency ω) is incident on the plane $x = 0$, with the electric field $E(x,y)e^{i\omega t}$ polarized along the z-axis.

In the free space outside of the photonic crystal ($x < 0$ and $x > L$) the Maxwell equations reduce to the Helmholtz equation

$$\left(\partial_x^2 + \partial_y^2\right) E(x,y) + \frac{\omega^2}{c^2}E(x,y) = 0. \qquad (2.2)$$

The mean (time averaged) photon number flux in the x-direction is given by [79]

$$j_H = \frac{\varepsilon_0 c^2}{4i\hbar\omega^2} \left(E^* \frac{\partial E}{\partial x} - E \frac{\partial E^*}{\partial x} \right). \qquad (2.3)$$

Inside the photonic crystal ($0 < x < L$) the Maxwell equations reduce to the Dirac equation [28, 29]

$$\begin{pmatrix} 0 & -iv_D(\partial_x - i\partial_y) \\ -iv_D(\partial_x + i\partial_y) & 0 \end{pmatrix} \begin{pmatrix} \Psi_1 \\ \Psi_2 \end{pmatrix} = (\omega - \omega_D) \begin{pmatrix} \Psi_1 \\ \Psi_2 \end{pmatrix}, \qquad (2.4)$$

for the amplitudes Ψ_1, Ψ_2 of a doublet of two degenerate Bloch states at one of the corners of the hexagonal first Brillouin zone.

As explained by Raghu and Haldane [28, 29][1], the modes at the six zone corners $\boldsymbol{K}_p, \boldsymbol{K}'_p$ ($p = 1, 2, 3$), which are degenerate for a homogeneous dielectric, are split by the periodic dielectric modulation into a pair of doublets at frequency ω_D and a pair of singlets at a different frequency. The first doublet and singlet have wave vectors at the first set of equivalent corners $\boldsymbol{K}_p$, while the second doublet and singlet are at $\boldsymbol{K}'_p$. Each doublet mixes and splits linearly forming a Dirac point as the wave vector is shifted by $\delta\boldsymbol{k}$ from a zone corner. The Dirac equation (2.4) gives the envelope field $\propto e^{i\delta\boldsymbol{k}\cdot\boldsymbol{r}}$ of one of these doublets.

The frequency ω_D and velocity v_D in the Dirac equation depend on the strength of the periodic dielectric modulation, tending to $\omega_D = c'|\boldsymbol{K}_p| = c'|\boldsymbol{K}'_p| = 4\pi c'/3a$ and $v_D = c'/2$ in the limit of weak modulation. (The speed of light c' in the homogeneous dielectric is smaller than the free space value c.)

Eq. (2.4) may be written more compactly as

$$-iv_D(\nabla \cdot \boldsymbol{\sigma})\Psi = \delta\omega\Psi, \quad \delta\omega \equiv \omega - \omega_D, \qquad (2.5)$$

in terms of the spinor $\Psi = (\Psi_1, \Psi_2)$ and the vector of Pauli matrices $\boldsymbol{\sigma} = (\sigma_x, \sigma_y)$. In the same notation, the velocity operator for the Dirac

---

[1]Ref. [28, 29] considers a photonic crystal formed by dielectric cylinders in air, while we consider the inverse geometry of cylindrical perforations of a dielectric medium. Both geometries have a Dirac point in the band structure, see M. Plihal and A. A. Maradudin, Phys. Rev. B **44**, 8565 (1991).
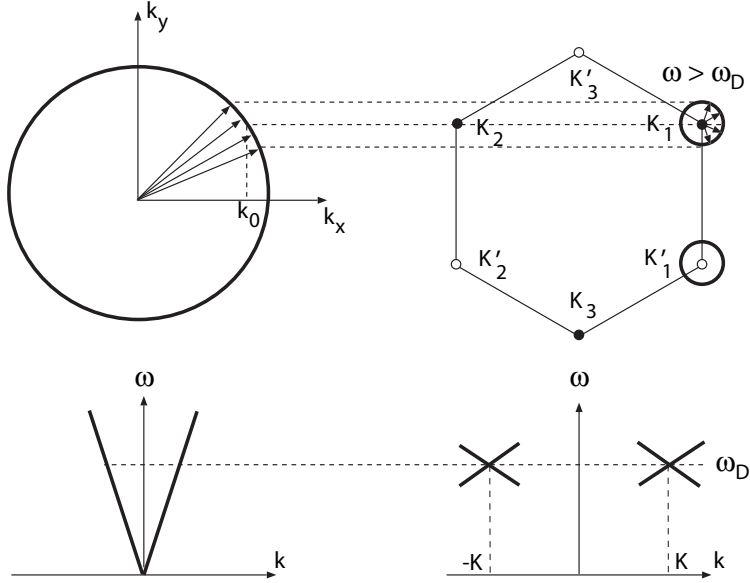
Figure 2.2. Right panels: Hexagonal first Brillouin zone of the photonic crystal (top) and dispersion relation of the doublet near one of the zone corners (bottom). Filled and open dots distinguish the two sets of equivalent zone corners, centered at $\boldsymbol{K}_p$ and $\boldsymbol{K}_p'$, respectively. The small circles centered at the zone corners are the equal-frequency contours at a frequency ω just above the frequency ω_D of the Dirac point. Left panels: Equal-frequency contour in free space (top) and corresponding dispersion relation (bottom). A plane wave in free space with k_x close to k_0 (arrows in the upper left panel) excites Bloch waves in the photonic crystal with $\boldsymbol{k}$ close to $\boldsymbol{K}_1$ and $\boldsymbol{K}_2$ (arrows in the upper right panel), as dictated by conservation of k_y and ω (dotted horizontal lines).

equation is $v_D\boldsymbol{\sigma}$. The mean photon number flux j_D in the x-direction is therefore given by

$$j_D = v_D\Psi^*\sigma_x\Psi = v_D(\Psi_1^*\Psi_2 + \Psi_2^*\Psi_1). \tag{2.6}$$

The termination of the photonic crystal in the y-direction introduces boundary conditions at the edges $y = 0$ and $y = W$ which depend on the details of the edges, for example on edges being of zigzag, armchair, or other type. For a wide and short crystal, $W \gg L$, these details become ir-

relevant and we may use periodic boundary conditions $[\Psi(x, 0) = \Psi(x, W)]$ for simplicity.

2.3   Wave Matching

The excitation of modes near a Dirac point has been discussed by Notomi [19], in terms of a figure similar to Fig. 2.2. Because the y-component of the wave vector is conserved across the boundary at $x = 0$, the doublet near $\boldsymbol{K}_1 = (K_x, K_y)$ or $\boldsymbol{K}_2 = (-K_x, K_y)$ can only be excited if the incident radiation has a wave vector $\boldsymbol{k} = (k_x, k_y)$ with k_y near K_y. The conservation of k_y holds up to translation by a reciprocal lattice vector. We will consider here the case of $|\boldsymbol{k}| < |\boldsymbol{K}_p|$, where no coupling to $\boldsymbol{K}_3$ is allowed. The actual radius of the equal frequency contour in the free space at $\omega = \omega_D$ will depend on a particular photonic crystal realization.

The incident plane waves $E_{\text{incident}} = E_0 e^{i\boldsymbol{k}\cdot\boldsymbol{r}}$ in free space that excite Bloch waves at a frequency $\delta\omega = \omega - \omega_D$ have $k_y = K_y[1 + \mathcal{O}(\delta\omega/\omega_D)]$ and $k_x = k_0[1 + \mathcal{O}(\delta\omega/\omega_D)]$ with

$$k_0 = \sqrt{(\omega_D/c)^2 - K_y^2}. \tag{2.7}$$

For $\delta\omega \ll \omega_D$ we may therefore write the incident wave in the form

$$E_{\text{incident}}(x, y) = E_+(x, y)e^{ik_0 x + iK_y y}, \tag{2.8}$$

with E_+ a slowly varying function. Similarly, the reflected wave will have $k_y \approx K_y$ and $k_x \approx -k_0$, so that we may write it as

$$E_{\text{reflected}}(x, y) = E_-(x, y)e^{-ik_0 x + iK_y y}, \tag{2.9}$$

with E_- slowly varying.

The orientation of the Brillouin zone shown in Fig. 2.2 corresponds to an armchair edge of the triangular lattice at $x = 0$. For this orientation only one of the two inequivalent doublets is excited for a given k_y. (The other doublet at $\boldsymbol{K}_1'$, $\boldsymbol{K}_2'$ is excited for $-k_y$.) A 90° rotation of the Brillouin zone would correspond to a zigzag edge. Then a linear combination of the two inequivalent doublets is excited near $k_y = 0$. For simplicity, we

will restrict ourselves here to the case shown in the figure of separately excitable doublets.

While the conservation of the wave vector component parallel to the boundary determines which modes in the photonic crystal are excited, it does not determine with what strength. For that purpose we need to match the solutions of the Helmholtz and Dirac equations at $x = 0$. The matching should preserve the flux through the boundary, so it is convenient to write the flux in the same form at both sides of the boundary.

The photon number flux (2.3) for the Helmholtz equation may be written in the same form as the flux (2.6) for the Dirac equation, by

$$j_H = v_H \mathcal{E}^* \sigma_x \mathcal{E}, \tag{2.10a}$$

$$v_H = \frac{\varepsilon_0 c^2 k_0}{4 \hbar \omega^2}, \quad \mathcal{E} = \begin{pmatrix} E_+ + E_- \\ E_+ - E_- \end{pmatrix}. \tag{2.10b}$$

(In the prefactor k_0 we have neglected corrections of order $\delta\omega/\omega_D$.) Flux conservation then requires

$$v_H \mathcal{E}^* \sigma_x \mathcal{E} = v_D \Psi^* \sigma_x \Psi, \quad \text{at} \ \ x = 0. \tag{2.11}$$

The matching condition has the general form [80]

$$\Psi = (v_H/v_D)^{1/2} M \mathcal{E}, \quad \text{at} \ \ x = 0. \tag{2.12}$$

The flux conservation condition (2.11) implies that the transfer matrix M should satisfy a generalized unitarity condition,

$$M^{-1} = \sigma_x M^\dagger \sigma_x. \tag{2.13}$$

Eq. (2.13) restricts M to a three-parameter form

$$M = e^{\gamma \sigma_z} e^{\beta \sigma_y} e^{i\alpha \sigma_x} \tag{2.14}$$

(ignoring an irrelevant scalar phase factor). The real parameters α, β, γ depend on details of the boundary at the scale of the lattice constant — they can not be determined from the Helmholtz or Dirac equations (the latter only holds on length scales $\gg a$).

We now show that the value of α becomes irrelevant close to the Dirac point. At the boundary the incident and reflected waves have the form

$$\mathcal{E}_{\text{incident}} = E_0 \begin{pmatrix} 1 \\ 1 \end{pmatrix}, \quad \mathcal{E}_{\text{reflected}} = r E_0 \begin{pmatrix} 1 \\ -1 \end{pmatrix}, \tag{2.15}$$

with r the reflection coefficient, and $E_0 \equiv E_+(0, y)$ a slowly varying function. Both "spinors" are eigenvectors of σ_x, hence the action of $e^{i\alpha\sigma_x}$ on $\mathcal{E}$ is simply a phase factor:

$$M\mathcal{E}_{\text{incident}} = e^{\gamma\sigma_z} e^{\beta\sigma_y} e^{i\alpha} \mathcal{E}_{\text{incident}},$$
$$M\mathcal{E}_{\text{reflected}} = e^{\gamma\sigma_z} e^{\beta\sigma_y} e^{-i\alpha} \mathcal{E}_{\text{reflected}}. \tag{2.16}$$

There is no need to determine the phase factor $e^{\pm i\alpha}$, since it has no effect on the reflection probability $|r|^2$.

A similar reasoning applies at the boundary $x = L$, where the matching condition reads

$$\Psi = (v_H/v_D)^{1/2} M' \mathcal{E}, \quad \text{at } x = L. \tag{2.17}$$

Flux conservation requires that $M' = e^{\gamma'\sigma_z} e^{\beta'\sigma_y} e^{i\alpha'\sigma_x}$, with real parameters α', β', γ'. The value of α' is again irrelevant close to the Dirac point, because the spinor of the transmitted wave

$$\mathcal{E}_{\text{transmitted}} = t E_0 \begin{pmatrix} 1 \\ 1 \end{pmatrix} \tag{2.18}$$

(with t the transmission coefficient) is an eigenvector of σ_x. So

$$M' \mathcal{E}_{\text{transmitted}} = e^{\gamma'\sigma_z} e^{\beta'\sigma_y} e^{i\alpha'} \mathcal{E}_{\text{transmitted}}, \tag{2.19}$$

with a phase factor $e^{i\alpha'}$ that has no effect on the transmission probability $|t|^2$.

2.4   Transmission Probability

We consider the case $W \gg L$ of a wide and short crystal, when we may use periodic boundary conditions at $y = 0, W$ for the Bloch waves $\Psi \propto e^{i\delta \boldsymbol{k} \cdot \boldsymbol{r}}$.
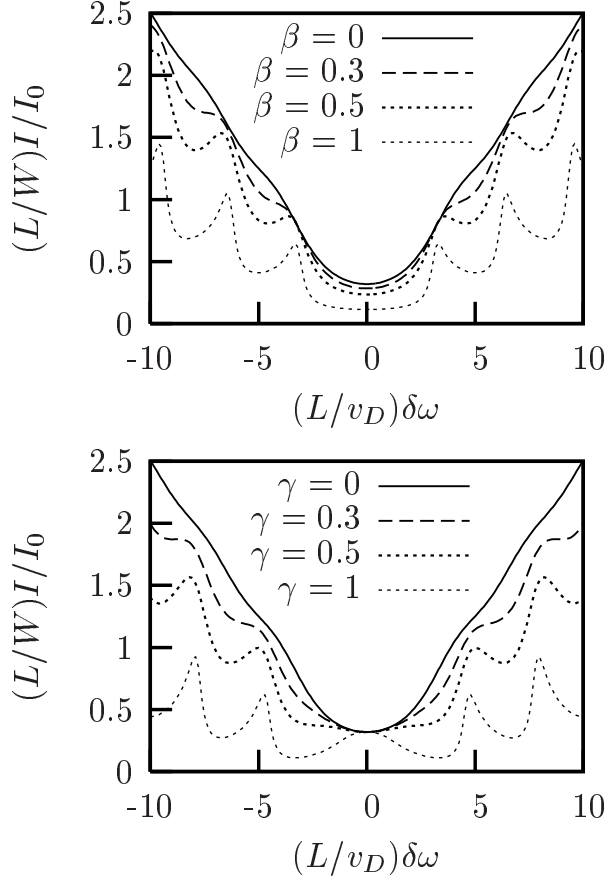
Figure 2.3. Frequency dependence of the transmitted current, for interface parameters $\beta' = \beta$, $\gamma' = -\gamma$. In the top panel we take $\gamma = 0$ and vary β, while in the bottom panel we take $\beta = 0$ and vary γ. The solid curves ($\beta = \gamma = 0$) correspond to maximal coupling of the photonic crystal to free space. The curves are calculated from Eqs. (2.27) and (2.30), in the regime $W/L \gg 1$ where the sum over modes may be replaced by an integration over transverse wave vectors.

The transverse wave vector δk_y is then discretized at $\delta k_y = 2\pi n/W \equiv q_n$, with mode index $n = 0, \pm 1, \pm 2, \pm 3, \ldots$. We seek the transmission amplitude t_n of the n-th mode.

We first determine the transfer matrix $M_n(x, 0)$ of the n-th mode

$\Phi_n(x)e^{iq_n y}$ through the photonic crystal, defined by

$$\Phi_n(x) = M_n(x,0)\Phi_n(0). \tag{2.20}$$

From the Dirac equation (2.5) we obtain the differential equation

$$\frac{d}{dx}M_n(x,0) = \left(\frac{i\delta\omega}{v_D}\sigma_x + q_n\sigma_z\right)M_n(x,0), \tag{2.21}$$

with solution

$$M_n(x,0) = \cos k_n x + \frac{\sin k_n x}{k_n}\left(\frac{i\delta\omega}{v_D}\sigma_x + q_n\sigma_z\right). \tag{2.22}$$

We have defined the longitudinal wave vector

$$k_n = \sqrt{(\delta\omega/v_D)^2 - q_n^2}. \tag{2.23}$$

The total transfer matrix through the photonic crystal, including the contributions (2.12) and (2.17) from the interfaces at $x = 0$ and $x = L$, is

$$\mathcal{M} = M'^{-1}M_n(L,0)M. \tag{2.24}$$

It determines the transmission amplitude by

$$\mathcal{M}\begin{pmatrix}1+r_n\\1-r_n\end{pmatrix} = \begin{pmatrix}t_n\\t_n\end{pmatrix} \quad\Rightarrow\quad \begin{pmatrix}1-r_n\\1+r_n\end{pmatrix} = \mathcal{M}^\dagger\begin{pmatrix}t_n\\t_n\end{pmatrix}$$

$$\Rightarrow\quad \frac{1}{t_n} = \frac{1}{2}\sum_{i=1}^{2}\sum_{j=1}^{2}\mathcal{M}_{ij}^*, \tag{2.25}$$

where we have used the current conservation relation $\mathcal{M}^{-1} = \sigma_x\mathcal{M}^\dagger\sigma_x$.

The general expression for the transmission probability $T_n = |t_n|^2$ is rather lengthy, but it simplifies in the case that the two interfaces at $x = 0$ and $x = L$ are related by a reflection symmetry. For a photonic crystal that has an axis of symmetry at $x = L/2$ both $\Phi(x)$ and $\sigma_y\Phi(L-x)$ are solutions at the same frequency. This implies for the transfer matrix the
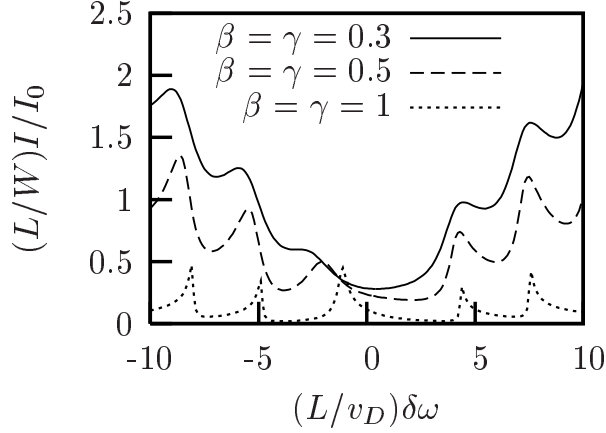
Figure 2.4. Same as Fig. 2.3, for β and γ both nonzero.

symmetry relation

$$
\begin{aligned}
\sigma_y \mathcal{M} \sigma_y &= \mathcal{M}^{-1} \Rightarrow \sigma_y M' \sigma_y = M \\
&\Rightarrow \beta' = \beta, \ \gamma' = -\gamma,
\end{aligned}
\tag{2.26}
$$

and we obtain

$$
\begin{aligned}
\frac{1}{T_n} = \Bigg(& \frac{\delta\omega \sin k_n L}{v_D k_n} \cosh 2\beta - \cos k_n L \sinh 2\beta \sinh 2\gamma \\
& - \frac{q_n \sin k_n L}{k_n} \sinh 2\beta \cosh 2\gamma \Bigg)^2 \\
& + \left(\cos k_n L \cosh 2\gamma + \frac{q_n \sin k_n L}{k_n} \sinh 2\gamma \right)^2 .
\end{aligned}
\tag{2.27}
$$

For an ideal interface (when $\beta = 0 = \gamma$) we recover the transmission probability of Ref. [77].

At the Dirac point, where $\delta\omega = 0 \Rightarrow k_n = iq_n$, Eq. (2.27) reduces further to

$$
\frac{1}{T_n} = \cosh^2(q_n L + 2\gamma) + \sinh^2 2\beta \sinh^2(q_n L + 2\gamma).
\tag{2.28}
$$

More generally, for two arbitrary interfaces, the transmission probability

at the Dirac point takes the form

$$\frac{1}{T_n} = \cosh^2(\beta - \beta') \cosh^2 \xi_n + \sinh^2(\beta + \beta') \sinh^2 \xi_n,$$

$$\xi_n = q_n L + \gamma - \gamma'. \tag{2.29}$$

While the individual T_n's depend on γ and γ', this dependence drops out in the total transmission $\sum_n T_n$.

2.5   Photon Current

The transmission probabilities determine the time averaged photon current I at frequency $\omega_D + \delta\omega$ through the photonic crystal,

$$I(\delta\omega) = I_0 \sum_{n=-\infty}^{\infty} T_n(\delta\omega), \tag{2.30}$$

where I_0 is the incident photon current per mode. The sum over n is effectively cut off at $|n| \sim W/L \gg 1$, because of the exponential decay of the T_n's for larger $|n|$. This large number of transverse modes excited in the photonic crystal close to the Dirac point corresponds in free space to a narrow range $\delta\phi \simeq a/L \ll 1$ of angles of incidence. We may therefore assume that the incident radiation is isotropic over this range of angles $\delta\phi$, so that the incident current per mode I_0 does not depend on n.

Since $W/L \gg 1$ the sum over modes may be replaced by an integration over wave vectors, $\sum_{n=-\infty}^{\infty} \to (W/2\pi) \int_{-\infty}^{\infty} dq_n$. The resulting frequency dependence of the photon current around the Dirac frequency is plotted in Figs. 2.3 and 2.4, for several values of the interface parameters. As we will now discuss, the scaling with the separation L of the interfaces is fundamentally different close to the Dirac point than it is away from the Dirac point.

Substitution of Eq. (2.29) into Eq. (2.30) gives the photon current at

the Dirac point,

$$I(\delta\omega = 0) = I_0 \Gamma_0 \frac{W}{L},$$
$$\Gamma_0 = \frac{\arctan[\sinh(\beta + \beta')/\cosh(\beta - \beta')]}{\pi \sinh(\beta + \beta')\cosh(\beta - \beta')}, \qquad (2.31)$$

independent of the parameters γ, γ'. For two ideal interfaces we reach the limit

$$\lim_{\beta,\beta'\to 0} I(\delta\omega = 0)/I_0 = \frac{1}{\pi}\frac{W}{L}, \qquad (2.32)$$

in agreement with Refs. [76, 77]. Eq. (2.31) shows that, regardless of the transparency of the interfaces at $x = 0$ and $x = L$, the photon current at the Dirac point is inversely proportional to the separation L of the interfaces (as long as $a \ll L \ll W$).

As seen in Figs. 2.3 and 2.4, the photon current at the Dirac point has an extremum (minimum or maximum) when either γ or β are equal to zero. If the interface parameters β, γ are both nonzero, then the extremum is displaced from the Dirac point by a frequency shift $\delta\omega_c$. The photon current $I(\delta\omega_c)$ at the extremum remains inversely proportional to L as in Eq. (2.31), with a different proportionality constant Γ_0 (which now depends on both β and γ).

The $1/L$-scaling of the photon current applies to a frequency interval $|\delta\omega| \lesssim v_D/L$ around the Dirac frequency ω_D. For $|\delta\omega| \gg v_D/L$ the photon current approaches the L-independent value

$$I_\infty = I_0 \Gamma \frac{W\delta\omega}{\pi v_D}, \qquad (2.33)$$

with rapid oscillations around this limiting value. The effective interface transmittance Γ is a rather complicated function of the interface parameters $\beta, \beta', \gamma, \gamma'$. It is still somewhat smaller than unity even for maximal coupling of the photonic crystal to free space ($\Gamma = \pi/4$ for $\beta = \gamma = 0$).

2.6　Conclusion

While several experiments [81, 82] have studied two-dimensional photonic crystals with a honeycomb or triangular lattice, the emphasis has been on the frequency range where the band structure has a true gap, rather than on frequencies near the Dirac point. Recent experiments on electronic conduction near the Dirac point of graphene have shown that this singularity in the band structure offers a qualitatively new transport regime [83]. Here we have explored the simplest optical analogue, the pseudo-diffusive transmission extremum near the Dirac point of a photonic crystal. We believe that photonic crystals offer a particularly clean and controlled way to test this prediction experimentally. The experimental test in the electronic case is severely hindered by the difficulty to maintain a homogeneous electron density throughout the system [84]. No such difficulty exists in a photonic crystal.

　　If this experimental test is successful, there are other unusual effects at the Dirac point waiting to be observed. For example, disorder has been predicted to increase — rather than decrease — the transmission at the Dirac point [85, 86, 87]. Photonic crystals could provide an ideal testing ground for these theories.

Chapter 3

Numerical Test of the Theory of Pseudo-Diffusive Transmission at the Dirac Point of a Photonic Band Structure

3.1 Introduction

Two-dimensional photonic crystals with a triangular lattice (such as shown in Fig. 3.1) have been studied extensively [14, 15, 16, 1, 17, 19, 18, 20, 21, 22, 23, 24, 25], in particular because they have a well-developed band gap. For frequencies inside this gap the transmission through the crystal decays exponentially with the thickness L. The band structure has another interesting feature which has received much less attention, namely the conical singularity that appears at the corner ($= K$-point) of the hexagonal first Brillouin zone [14]. As indicated in Fig. 3.2, at a given wave vector near the K-point two Bloch modes are nearly degenerate in frequency. The envelopes of the Bloch modes satisfy a pair of coupled differential equations that have the same form as the Dirac equation of relativistic quantum mechanics [28, 29]. Hence the name "Dirac point" given to
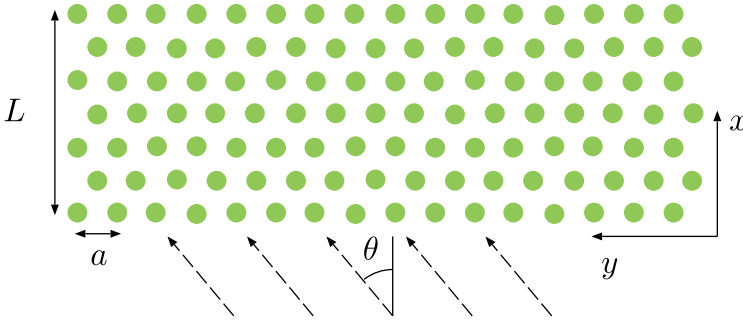
Figure 3.1. Top view of a two-dimensional photonic crystal formed by dielectric rods on a triangular lattice in the $x - y$ plane, aligned along the z-direction. The lattice constant a (centre-to-centre distance of the rods) is indicated. We calculate the transmission through the slab of thickness L of radiation incident near the K-point of the photonic crystal, and find that it scales as $1/L$.

the conical singularity. The essential difference between a band gap and a Dirac point is that the density of states is zero for a finite frequency interval in the former case, but only at a single frequency in the latter case.

Motivated by an electronic analogue (graphene [77]), Bazaliy and the authors [89] have recently predicted a new signature of the conical singularity: near the Dirac point the photon flux I transmitted through a slab of photonic crystal is predicted to scale as $1/L$ with the thickness L of the slab. The $1/L$ scaling is called "pseudo-diffusive" due to its reminiscence of diffusion through a disordered medium — although here it appears for Bloch modes in the absence of any disorder inside the photonic crystal.

More quantitatively, the prediction of Ref. [89] is that at the Dirac point

$$I = I_0 \Gamma_0 \frac{1}{L}, \quad 0 < \Gamma_0 < 1/\pi, \tag{3.1}$$

with I_0 the incident photon current per transverse mode and I the transmitted photon flux (= transmitted photon current per unit width). The coefficient Γ_0 that determines the slope of the $1/L$ scaling depends on the coupling strength of the Bloch modes inside the photonic crystal to the plane waves outside. For maximal coupling one has $\Gamma_0 = 1/\pi$ [77, 89].

It is the purpose of this chapter to test the prediction of Ref. [89]
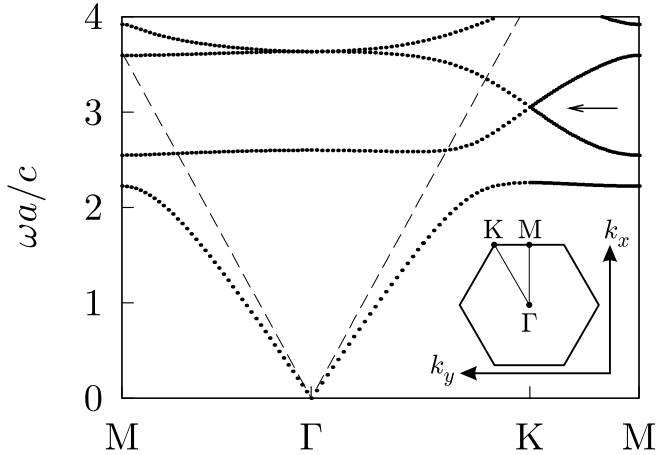
Figure 3.2. Electromagnetic band structure of the photonic crystal shown in Fig. 3.1, calculated for a dielectric constant $\epsilon = 14$ inside the rods and $\epsilon = 1$ (air, speed of light c) outside the rods. (We used the MPB software package for this type of calculation [88].) The rods (radius $r = 0.27\,a$) occupy a fraction $f = 0.26$ of space in the crystal. The bands are shown for the case that the magnetic field is parallel to the rods (TE modes). The arrow points to the conical singularity (Dirac point) and the dashed line shows the dispersion relation in free space. The first Brillouin zone is drawn in the inset. (Note that the $\Gamma - M$ direction is perpendicular to the $x = 0$ interface of the photonic crystal, for the orientation of Fig. 3.1.)

quantitatively, by means of a numerical solution of the scattering problem. (An independent test in Ref. [90] provides only a qualitative comparison.) By means of an exact solution of Maxwell's equations we can test how well the Dirac equation used in Ref. [89] describes the scattering near the Dirac point. Furthermore, we can determine the slope Γ_0 — which is beyond the reach of the Dirac equation and was left undetermined in Ref. [89].

3.2   Interface Parameters

We solve the scattering problem in the geometry of Fig. 3.1 for the parameters listed in Fig. 3.2. The transmitted photon flux for a given incident plane wave $\propto e^{ik_x x + ik_y y}$ is calculated as a function of frequency $\omega = c\sqrt{k_x^2 + k_y^2}$ for a given thickness L of the crystal. (The transverse
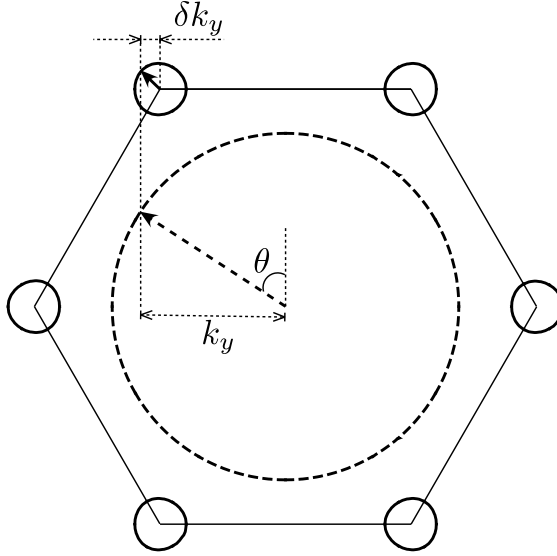
Figure 3.3. Equifrequency contours for the photonic crystal of Fig. 3.2, calculated for $\omega = 2.89\,c/a = 0.95\,\omega_D$. The contours (thick solid lines) are centered at the corners of the first Brillouin zone, and are approximately circular with a slight trigonal distortion. The dashed circle is the equifrequency contour in free space, at the same ω. An incident plane wave at an angle θ (dashed arrow) is coupled to Bloch modes in the crystal with the same wave vector component k_y (solid arrow shows wave vector of the envelope field). When $\omega \to \omega_D$, the radius of the equifrequency contours shrinks to zero and the incident plane wave can only couple to evanescent (exponentially decaying) Bloch modes.

width is infinite in the calculation.) We use the finite-difference time-domain method [56], as implemented in the MEEP software package [61].

To make contact with Ref. [89] we first extract from Fig. 3.2 the parameters $\omega_D = 3.05\,c/a$, $v_D = 0.369\,c$ that characterise the conical singularity in the band structure,

$$\delta\omega \equiv \omega - \omega_D = v_D|\delta\boldsymbol{k}|. \qquad (3.2)$$

Here $\delta\boldsymbol{k} = \boldsymbol{k} - \boldsymbol{K}$ is the displacement of the wave vector $\boldsymbol{k}$ from the K-point, with wave vector $\boldsymbol{K} = \frac{2}{3}\pi a^{-1}(\sqrt{3}, 1)$. The velocity v_D is the group velocity of Bloch modes at frequencies near the frequency ω_D of the Dirac

point. A given δk_y corresponds to an angle of incidence

$$\theta = \arcsin\left[\frac{c}{\omega}(K_y + \delta k_y)\right]. \tag{3.3}$$

In particular, $\delta k_y = 0$ and $\omega = \omega_D$ correspond to $\theta = \arcsin\left(2\pi c/3\omega_D a\right) \equiv \theta_0$. For our parameters $\theta_0 = 43°$.

As indicated in Fig. 3.3, an incident plane wave couples to Bloch modes in the photonic crystal with the same k_y. Propagating envelope modes have wave vector on the equifrequency contour centered at a K-point. As the frequency ω approaches the Dirac frequency ω_D, the radius of the equifrequency contour shrinks to zero, and the incident plane wave can only couple to evanescent modes. These decay exponentially away from the interface, with a decay length $\propto 1/|\delta k_y|$ which becomes infinitely long at the K-point.

The crucial difference between transmission at the Dirac frequency and inside a band gap is this: In both cases, the photonic crystal supports only evanescent Bloch modes, but inside the band gap the decay length as a function of angle of incidence has a finite maximum value — while at the Dirac frequency the maximum decay length is infinite. As a consequence, angular averaging of the transmitted intensity over some narrow range of incident angles around θ_0 gives an exponentially decaying transmission inside the band gap, but only an algebraic $1/L$ decay at the Dirac frequency [89].

For a quantitative description of this scaling behavior we need to consider the coupling strength of the Bloch modes inside the crystal to the plane waves outside. The transfer matrix of the interface at $x = 0$ and $x = L$, which determines this coupling, is characterised by two parameters β and γ. These parameters enter into the expression for the transmission probability $T(\delta k_y, \delta\omega)$, which is defined as the ratio of transmitted to incident photon flux for an incident plane wave [frequency $\omega = \omega_D + \delta\omega$ and
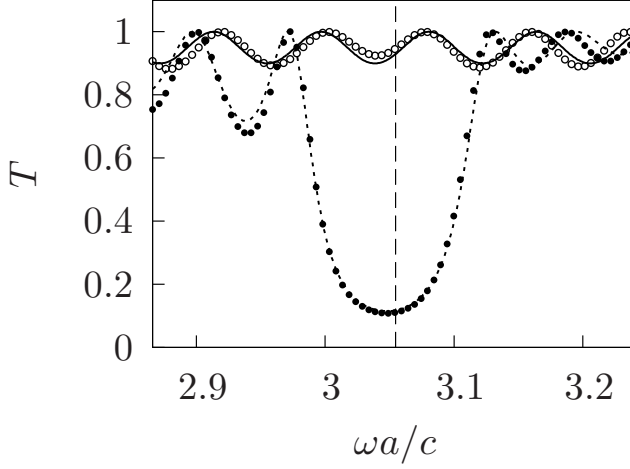
Figure 3.4.   Transmission probability through the slab of photonic crystal of thickness $L = 8\sqrt{3}\,a$. The data points are the numerical results, the curves are calculated from Eq. (3.4) with the interface parameters of Eq. (3.5). The vertical dashed line indicates the Dirac frequency ω_D. This plot is for a single incident plane wave with $\delta k_y = 0$ (open data points, solid curve) and $\delta k_y = -(\pi/30)a^{-1}$ (filled data points, dotted curve).

angle of incidence θ related to δk_y by Eq. (3.3)]. The result is [89]

$$
\frac{1}{T} = \left(\frac{\delta\omega L \sin\sigma}{v_D \sigma} \cosh 2\beta - \cos\sigma \sinh 2\beta \sinh 2\gamma \right.
$$
$$
\left. - \frac{\delta k_y L \sin\sigma}{\sigma} \sinh 2\beta \cosh 2\gamma \right)^2
$$
$$
+ \left(\cos\sigma \cosh 2\gamma + \frac{\delta k_y L \sin\sigma}{\sigma} \sinh 2\gamma \right)^2, \quad (3.4)
$$

with $\sigma = L\sqrt{(\delta\omega/v_D)^2 - \delta k_y^2}$.

We extract the two interface parameters

$$
\beta = -0.094, \quad \gamma = -0.133 \tag{3.5}
$$

from the T versus $\delta\omega$ dependence at $\delta k_y = 0$, plotted in Fig. 3.4. In the same figure we show that the δk_y dependence of these parameters is
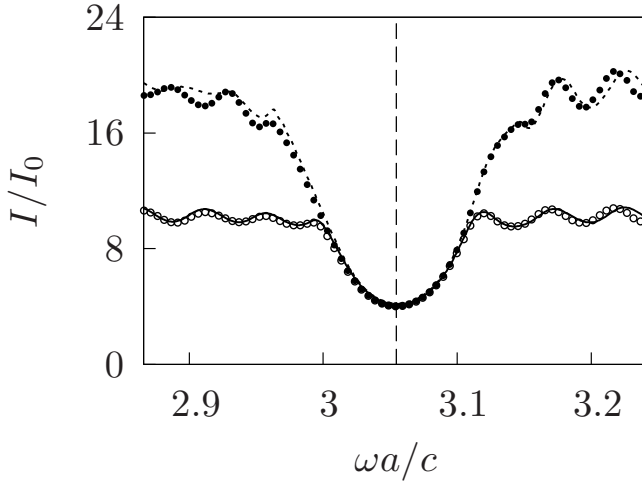
Figure 3.5. Transmitted flux (3.6) for $L = 13\sqrt{3}\,a$. Data points are the numerical results, curves are calculated from Eq. (3.4). The vertical dashed line indicates the Dirac frequency ω_D. This plot is for a range $|\delta k_y| \leq \Delta$ of incident wave vectors, with $\Delta = (\pi/30)a^{-1}$ for the open data points and solid curve; $\Delta = (\pi/15)a^{-1}$ for the filled data points and dotted curve.

weak for $\delta k_y a \ll 1$, as was assumed in Ref. [89], since the same set of parameters (3.5) also describes the $\delta\omega$ dependence of T at nonzero δk_y.

3.3   1/L Scaling

To test for the $1/L$ scaling we need to consider a range $-\Delta < \delta k_y < \Delta$ of incident transverse wave vectors. (This corresponds to a range $\Delta\theta \simeq 2c\Delta/\omega_D \cos\theta_0$ of incident angles centered at θ_0.) According to Ref. [89] the $1/L$ scaling is reached when $L \gtrsim 1/\Delta$. We calculate the transmitted photon flux $I(\omega)$ in this range of wave vectors,

$$I(\omega) = I_0 \int_{-\Delta}^{\Delta} \frac{\delta k_y}{2\pi}\, T(\delta k_y, \delta\omega = \omega - \omega_D). \qquad (3.6)$$

As shown in Fig. 3.5, we find a strong dependence of I on the range of wave vectors Δ away from the Dirac frequency — but not at the Dirac
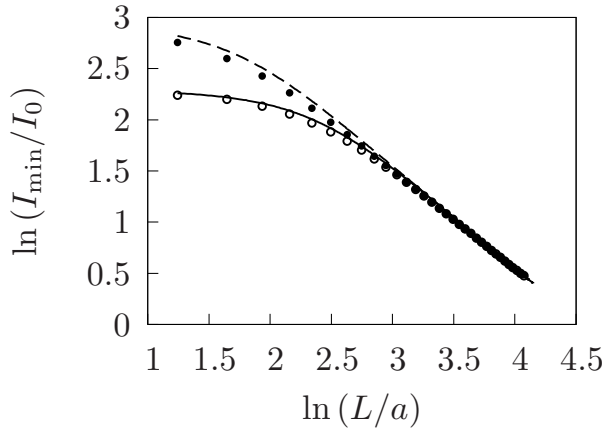
Figure 3.6. Transmitted flux I_{min} at the minimum near the Dirac point versus the thickness L of the slab. Open data points are for $\Delta = (\pi/30)a^{-1}$, filled data points are for $\Delta = (\pi/15)a^{-1}$. The solid and dashed lines show the analytical prediction from Eq. (3.4) with the interface parameters of Eq. (3.5).

	ϵ	f	$\omega_D c/a$	v_D/c	β	γ	Γ_0
○	14	0.26	3.05	0.369	-0.094	-0.133	0.298
▲	14	0.43	2.50	0.254	0.065	-0.162	0.295
●	8.9	0.33	3.03	0.432	-0.095	-0.197	0.298
+	8.9	0.40	2.83	0.393	-0.045	-0.199	0.298

Table 3.1. Parameters representing four different triangular lattice photonic crystals. Symbols on the left correspond to the data points in Fig. 3.7.

frequency, where the transmitted flux reaches a minimum I_{min} which is Δ independent for $\Delta \gtrsim 1/L$.[1]

In Fig. 3.6 we plot the L dependence of I_{min} on a double-logarithmic scale. For $L \gg \Delta^{-1}$ the predicted $1/L$ scaling of Eq. (3.1) is obtained, with a coefficient $\Gamma_0 = 0.30$. This coefficient is just 6% smaller than the value $\Gamma_0 = 1/\pi$ reached for maximal coupling of Bloch modes and plane waves at the interfaces between the photonic crystal and free space.

---

[1]The frequency ω_{min} of the transmission minimum is slightly offset from the Dirac frequency ω_D, but the relative offset is small and vanishes with increasing L: $|\omega_{min} - \omega_D|/\omega_D \approx 10^{-2}\, a/L$. We have checked that it makes no difference for the $1/L$ scaling whether we calculate the transmitted flux at ω_{min} or at ω_D.
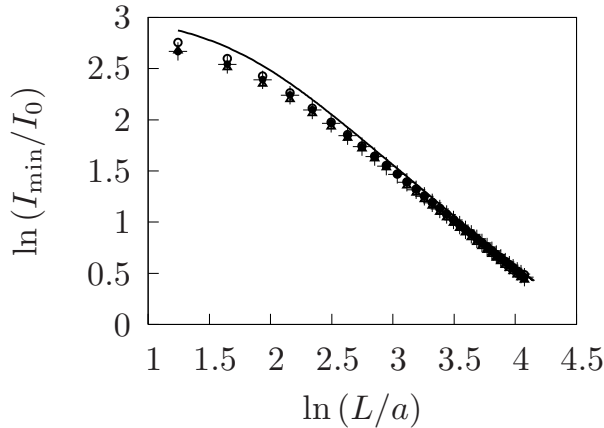
Figure 3.7. Minimal transmitted flux versus slab thickness for the four data sets tabulated in Table 3.1. We took $\Delta = (\pi/15)a^{-1}$ in each case. The analytical result for maximal coupling ($\beta = \gamma = 0$) is indicated by the solid curve.

To investigate how generic these results are, we have repeated the calculation for different values of the dielectric constant ϵ of the rods and for different filling fractions f (related to the radius r of the rods by $f = 2\pi r^2/\sqrt{3}a^2$). The parameters corresponding to the four sets of data are tabulated in Table 3.1. In Fig. 3.7 we show the L dependence of the minimal transmitted flux for each data set. In each case we find $1/L$ scaling with a slope Γ_0 that remains within 8% of the maximal value $\Gamma_0 = 1/\pi$.

3.4   Conclusion

In conclusion, we have presented a quantitative numerical test of the applicability of the Dirac equation [28, 29] to a photonic crystal with a conical singularity in the band structure. The numerical results are in good agreement with the analytical predictions [89] for the transmission through a finite slab. In particular, our numerical calculation demonstrates the $1/L$ scaling of the transmitted photon flux with a slope that is close to the value for maximal coupling at the interface with free space. This finding implies that transmission experiments can be used to search for intrinsic

properties of the Dirac point in the band structure, not hindered by a weak coupling to the outside.

Appendix 3.A   Details of the Numerical Calculations

In this appendix we give details of our numerical calculations performed with the MEEP software package. In order to calculate the transmission and reflection spectra through a sample we set up a computational cell (or computational domain — a volume where the simulation runs), shown in Fig. 3.8. On the right and on the left of the computational cell we put a perfectly matched layer (PML). As was explained in subsection 1.4.1 of the introductory chapter, a PML absorbs waves which are incident on it, thus, being equivalent to open boundary conditions.

We use a Gaussian pulse to obtain transmission and reflection in a frequency interval. The line source and the planes where the magnetic and electric fields are measured every time step (flux lines) are offset from the structure by a couple of wavelengths distance. The source is offset from the structure to make sure the local density of states does not affect the power the source irradiates, so that the same power is irradiated as when the normalization run without a sample is performed. The flux planes are offset from the structure because the proximity of the PML to evanescent modes may extract energy from the system.

MEEP gives the possibility to use Bloch periodic boundary conditions, which means one can choose any phase difference between boundaries. This allows propagation of a tilted plane wave emitted by the source with any desired angle or with any desired wave vector k_y along the y direction. Since we use a Gaussian pulse and the angle depends on frequency, it is more convenient to use k_y as a measure of tilt. The phase difference $\Delta\varphi$ between the upper and the lower boundaries is related to k_y by:

$$k_y = \Delta\varphi/W, \tag{3.7}$$

where W is the width of the cell. In contrast, in the case when periodic
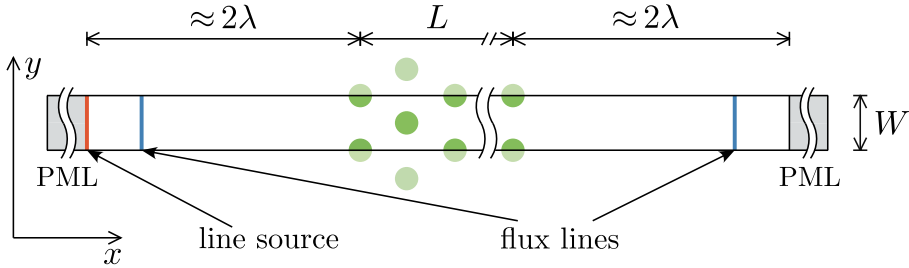
Figure 3.8. Schematic view of the computational cell. Perfectly matched layers are displayed in gray on the right and on the left of the computational cell. The flux lines and the line source are shown, respectively, in blue and red. The sample and perfectly matched layers are much longer than shown in the figure. Parts of the photonic crystals that are not present in the computational cell are indicated in pale green to show the triangular symmetry of the lattice.

boundary conditions are used, k_y takes discrete values, that is:

$$k_y = \Delta\varphi/W = 2\pi n/W, \tag{3.8}$$

with $n = 0, \pm 1, \pm 2, \ldots$.

Having set the phase difference between upper and lower boundaries, we assign different phases $\varphi(y)$ to every point y of the line source according to $\varphi(y) = k_y y$. This creates a tilted plane wave with a Gaussian time profile.

By using the subpixel averaging (for more information about the subpixel averaging implemented in MEEP see Ref. [61]) the desired accuracy is reached for resolution in pixels per unit length equal to 20. This means that every unit length (center-to-center distance between rods is set to one unit length) of the computational cell contains 20 space increments. We also measure the reflection spectrum to make sure that reflection and transmission sum to unity.

Chapter 4

How to Detect the Pseudospin-$\frac{1}{2}$ Berry Phase in a Photonic Crystal with a Dirac Spectrum

4.1 Introduction

Geometric phases (also known as Berry phases) typically appear in optics and quantum mechanics when a spin degree of freedom is transported along a closed orbit[1]. The geometric phase is given by the product of the enclosed solid angle and the spin, independently of the duration of the orbit (hence the adjective "geometric").

The spin is usually $\frac{1}{2}$ in the quantum mechanical context, when the spin is the electron spin. In the optical context, the spin corresponds to the light polarization and may be either $\frac{1}{2}$ or 1 depending on whether the photon momentum is cycled or kept fixed [91]. An early experimental detection of the spin-1 geometric phase of a photon was the measurement of the rotating linear polarization in a twisted optical fiber [92]. For electrons, the recently observed [93, 94] anomalous quantization of Landau

---

[1]The history of the geometric phase is described by M. V. Berry in Ref. [68]. Seminal papers are reprinted in Ref. [65]. A guide to the literature is Ref. [66]

levels in graphene is a direct manifestation of the geometric phase of π acquired by a pseudospin-$\frac{1}{2}$ which rotates over $360°$ in a cyclotron orbit (since the pseudospin is tangential to the velocity).

The graphene example is unusual because the spin-$\frac{1}{2}$ that is rotating is not the true electron spin but an orbital degree of freedom with the same SU(2) symmetry, emerging from the motion of the electron in the periodic potential of the carbon atoms. Such a pseudospin is not tied to the fermionic statistics of the electrons and so it might also manifest itself in the bosonic optical context.

The optical analogue of graphene is a photonic crystal with a two-dimensional (2D) triangular lattice structure. Haldane and Raghu [28, 29] showed that a pair of almost degenerate Bloch waves $(\Psi_1, \Psi_2) \equiv \Psi$ near a K-point of the Brillouin zone can be represented by a pseudospin, coupled to the orbital motion. The wave equation,

$$H\Psi = \varepsilon\Psi, \;\; \varepsilon = \frac{\omega - \omega_D}{v_D}, \tag{4.1a}$$

$$H = -i\sigma_x \frac{\partial}{\partial x} - i\sigma_y \frac{\partial}{\partial y} + \mu\sigma_z, \tag{4.1b}$$

is the 2D Dirac equation of a spin-$\frac{1}{2}$ particle with mass μ (nonzero if inversion symmetry is broken) [28, 29]. The resulting dispersion relation,

$$\varepsilon^2 = k_x^2 + k_y^2 + \mu^2, \tag{4.2}$$

reduces to a double cone in the case $\mu = 0$ of a perfect lattice, with a degeneracy at the frequency ω_D of the Dirac point. The slope $d\omega/dk = v_D$ is the frequency-independent group velocity. The upper cone (frequencies $\omega > \omega_D$) corresponds to the conduction band in graphene, and the lower cone ($\omega < \omega_D$) to the valence band. Several analogies between the electronic and optical transport properties near the Dirac point have been analysed [28, 29, 89, 95, 96, 90, 97]. What is missing is an optical way to directly observe the geometric phase due to the rotating pseudospin, analogous to the "smoking gun" found in the electronic cyclotron motion [93, 94].

A direct analogy is problematic because there exists no optical cy-

clotron motion. One can imagine other ways to have a photon execute a closed orbit, but the large and unspecified dynamical phase is likely to obscure the geometric phase. Here we show how complementary media [98] can be used to eliminate the dynamical phase, resulting in a transmission minimum that is a direct consequence of the π phase shift acquired by the rotating pseudospin. We support our argument by an analytical solution of the Dirac equation and by a numerical solution of the full Maxwell equations.

4.2   Calculation of the Geometric Phase

The system that can isolate the geometric phase from the dynamical phase is illustrated in Fig. 4.1 (lower two panels). It is the optical analogue of the p-n junction in graphene studied in Ref. [99]. In graphene, complementary media are formed when the Fermi level crosses from the conduction band to the valence band [100]. For the optical analogue, we introduce a (smooth) step in the Dirac frequency at $x = 0$, so that ω_D decreases from ω_D^- for $x < 0$ to ω_D^+ for $x > 0$. The Dirac frequency can be changed for instance by varying the radius of the dielectric rods that form the photonic crystal. Unlike in the electronic case, a shift of ω_D is generally accompanied by a shift of v_D, from v_D^- to v_D^+. The corresponding shift in the parameter ε is from ε^- to ε^+. We define the complementarity frequency ω_c such that

$$\frac{\omega_c - \omega_D^+}{v_D^+} = -\frac{\omega_c - \omega_D^-}{v_D^-} \Leftrightarrow \varepsilon^+ = -\varepsilon^-. \tag{4.3}$$

As illustrated in Fig. 4.2, waves of frequency ω_c have the same wave vector in absolute value in the two regions $x < 0$ and $x > 0$, but of opposite orientation relative to the group velocity (since k and $d\omega/dk$ have the same sign for $x > 0$ and opposite sign for $x < 0$). Dynamical phase shifts accumulated in the two regions thus cancel, leaving only the geometric phase from the rotation of the pseudospin.

We calculate the geometric phase for the closed orbit shown in Fig. 4.1 (top panel). Notice the negative refraction [100, 19] at the interface $x = 0$ where the orbit tunnels between the upper and lower cones of the dispersion relation (Klein tunneling). The component $k_y = q$ of the
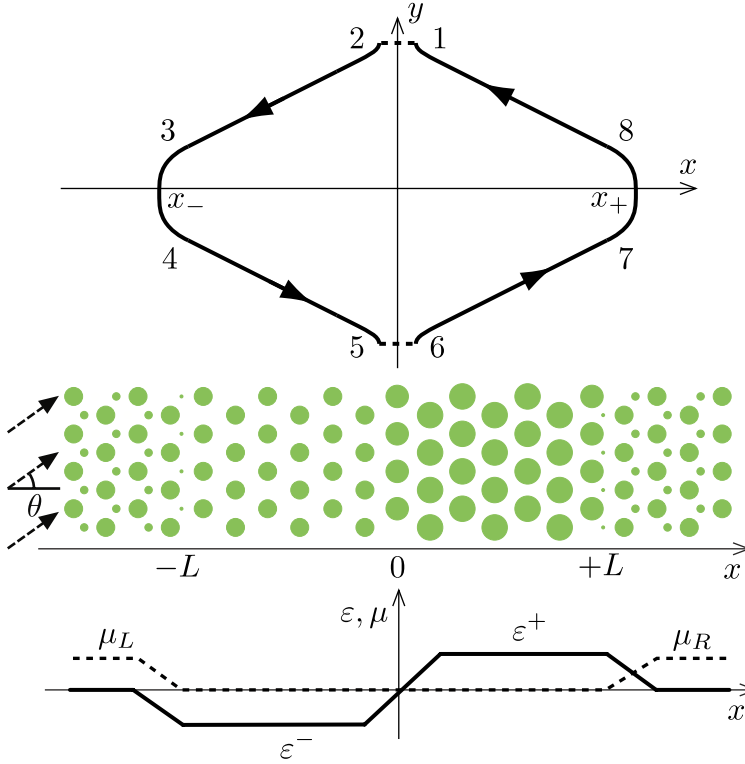
Figure 4.1. Lower two panels: Schematic layout (not to scale) of the triangular-lattice photonic crystal (with the cross-section of the dielectric rods shown in green) and plot of the corresponding profiles $\varepsilon(x)$ and $\mu(x)$. The two regions $x < 0$ and $x > 0$ form complementary media if the rescaled frequency ε is an odd function of x while the mass term μ is an even function of x. The top panel shows a closed orbit in the photonic crystal, with the dashed lines indicating tunneling through the region of imaginary wave vector.

wave vector parallel to the interface is conserved (because of translational invariance in the y-direction), while the component $k_x = k$ changes sign when $x \mapsto -x$. The orbit is reflected at the turning points $x_\pm$ by a mass term $\mu(x)$. We require $\mu(-x) = \mu(x)$ and $\varepsilon(-x) = -\varepsilon(x)$. Because $\Psi(x)$ and $\sigma_x \Psi(-x)$ are then both solutions of Eq. (4.1) (for a given y-dependence $\propto e^{iqy}$), it follows that the transfer matrix $M(x, x')$ through
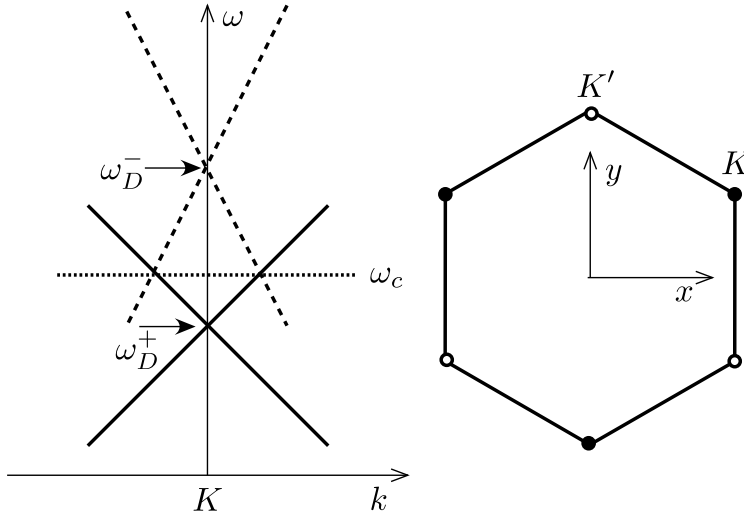
Figure 4.2. Left panel: Schematic view of the conical dispersion relations near a K-point, in the region $x > 0$ (solid lines) and $x < 0$ (dashed lines). The horizontal dotted line indicates the frequency ω_c, given by Eq. (4.3), at which the two regions form complementary media. Right panel: Hexagonal first Brillouin zone of the triangular lattice. The K and K'-points are indicated by filled and open dots, respectively. Only the K-points are excited in the geometry of Fig. 4.1.

the photonic crystal [defined by $\Psi(x) = M(x, x')\Psi(x')$] satisfies

$$M(x, 0)\sigma_x M(0, -x) = \sigma_x. \qquad (4.4)$$

This is a generalized complementarity relation [101] (the original complementarity relation [98] would have the unit matrix in place of σ_x).

A trajectory description is applicable if the variations of μ, ω_D, and v_D with x are smooth on the scale of the wave length. The spatial derivatives in Eq. (4.1) may then be replaced by the local wave vector, $-i\nabla \rightarrow \boldsymbol{k}$ (measured relative to the K point). The solution is

$$\Psi = \mathcal{C}^{-1/2} \begin{pmatrix} \mu + \varepsilon \\ k + iq \end{pmatrix} \equiv \begin{pmatrix} \cos(\theta/2) \\ e^{i\phi}\sin(\theta/2) \end{pmatrix}, \qquad (4.5)$$

with k determined from ε, μ, q through Eq. (4.2) and $\mathcal{C} = (\mu+\varepsilon)^2 + |k+iq|^2$
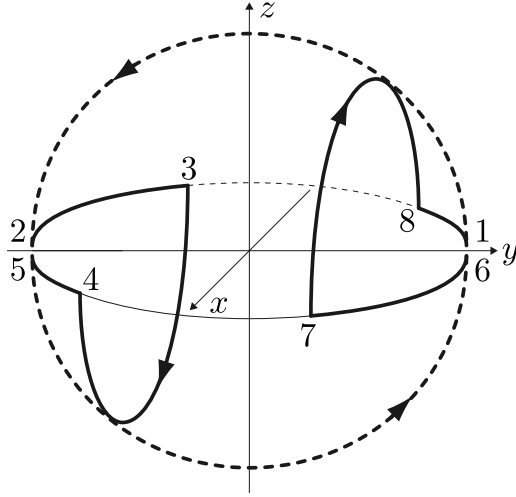
Figure 4.3. Rotation of the Bloch vector $\boldsymbol{B}$ along the closed orbit of Fig. 4.1, with the corresponding points numbered. The full rotation sweeps out a solid angle of 2π, producing a Berry phase of π.

a normalization constant. The angles ϕ, θ define the Bloch vector $\boldsymbol{B} = (\cos\phi\sin\theta, \sin\phi\sin\theta, \cos\theta)$, representing the direction of the pseudospin on the Bloch sphere. The rotation of the Bloch vector along the closed orbit is indicated in Fig. 4.3.

The geometric phase $\Phi = \Omega/2$ is one half the solid angle Ω subtended at the origin by the rotating Bloch vector [65]. We distinguish three contributions to Ω, a contribution Ω_- from the trajectory in the lower cone of the dispersion relation ($x < 0$), a contribution Ω_+ from the trajectory in the upper cone ($x > 0$), and a contribution Ω_K from Klein tunneling between the two cones (through the interface $x = 0$, indicated by dashed lines). The Bloch vector that sweeps out $\Omega_\pm$ is given by $\boldsymbol{B} = (k, q, \mu)/\varepsilon$. It follows from $k(-x) = -k(x)$, $\mu(-x) = \mu(x)$, $\varepsilon(-x) = -\varepsilon(x)$ that $\Omega_+ = -\Omega_-$, so the two contributions from the upper and lower cones cancel.

The contribution from Klein tunneling between the points $\pm\delta x$ has imaginary $k = i\kappa$. The sign of κ is positive when tunneling towards positive x (from the lower cone to the upper cone) and negative when

tunneling towards negative x (from upper to lower cone) — to ensure a decaying wave $\propto e^{-\kappa x}$.

The Bloch vector

$$\boldsymbol{B} = (\mu^2 + q^2)^{-1} \begin{pmatrix} 0 \\ \kappa\mu + q\varepsilon \\ \mu\varepsilon - \kappa q \end{pmatrix} \tag{4.6}$$

rotates in the $y - z$ plane from $\boldsymbol{B}_+$ to $\boldsymbol{B}_-$ through the positive z-axis (tunneling from upper to lower cone) and back to $\boldsymbol{B}_+$ through the negative z-axis (tunneling from lower to upper cone). The value of $\boldsymbol{B}_\pm$ of the Bloch vector at points $\pm\delta x$ follows from Eq. (4.6) with $\kappa = 0$,

$$\boldsymbol{B}_\pm = \frac{1}{\varepsilon(\pm\delta x)} \begin{pmatrix} 0 \\ q \\ \mu(\pm\delta x) \end{pmatrix} \Rightarrow \boldsymbol{B}_- = -\boldsymbol{B}_+. \tag{4.7}$$

The resulting $360°$ rotation of $\boldsymbol{B}$ in the $y - z$ plane sweeps out a solid angle $\Omega_K = 2\pi$, so that the total geometric phase acquired in the closed orbit of Fig. 4.1 is $\Phi = \pi$.

4.3   Destructive Interference of Partial Waves

The Berry phase of π suppresses the formation of a bound state at the complementarity frequency ω_c. To show this, we demonstrate the destructive interference of partial waves that return to the point of origin after multiple tunnel events. A more formal proof of the absence of a bound state at ω_c is given in App. 4.A.

The scattering problem is illustrated in Fig. 4.4. Partial wave amplitudes are labelled A_n for $x < 0$ and B_n for $x > 0$. The wave amplitudes at a tunnel event (black circle) are related by a unitary scattering matrix,

$$\begin{pmatrix} A_{n+1} \\ B_n \end{pmatrix} = S \begin{pmatrix} A_n \\ B_{n+1} \end{pmatrix}, \quad S = \begin{pmatrix} r & t' \\ t & r' \end{pmatrix}. \tag{4.8}$$

The phase shift of π acquired in a single closed loop $A_n \rightarrow B_n \rightarrow A_n$
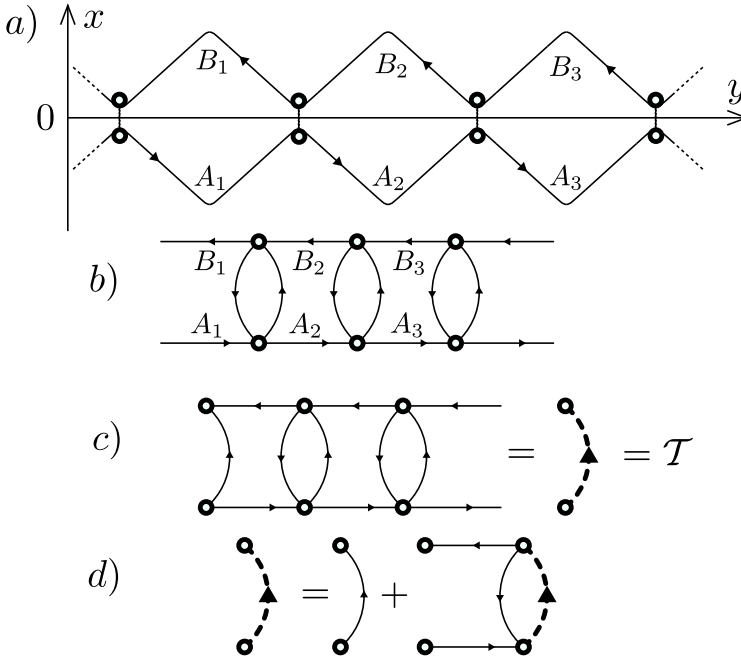
Figure 4.4. Sequence of partial wave amplitudes A_n and B_n, produced by tunnel events (black circles) at the interface $x = 0$ between two complementary media. Panel a) shows a top view of the multiply scattered rays, panel b) shows a more abstract representation. Panels c) and d) illustrate the construction of the total transmission amplitude $\mathcal{T}$ and of the Dyson equation that it obeys.

implies

$$\arg(t) + \arg(t') = \pi \Rightarrow t' = -t^*. \tag{4.9}$$

Unitarity of S then requires that the scattering matrix of a tunnel event is of the form

$$S = \begin{pmatrix} r & -t^* \\ t & r^* \end{pmatrix}, \quad |r|^2 + |t|^2 = 1. \tag{4.10}$$

An initial wave amplitude A_n^{initial} interferes with the sum A_n^{final} of partial wave amplitudes that return after different sequences of tunnel events. Each sequence $A_n \rightarrow \cdots \rightarrow B_n \rightarrow \cdots \rightarrow A_n$ includes B_n exactly once. We write $A_n^{\text{final}} = \mathcal{T}'\mathcal{T} A_n^{\text{initial}}$, with $\mathcal{T}$ the total transmission amplitude from A_n^{initial} to B_n and $\mathcal{T}'$ the total transmission amplitude from B_n to A_n^{final}.

For $\mathcal{T}$ we can construct a Dyson equation (see Fig. 4.4):

$$\mathcal{T} = t + r'\mathcal{T}r + r'\mathcal{T}t'\mathcal{T}r + r'\mathcal{T}(t'\mathcal{T})^2 r + \cdots \tag{4.11}$$

$$= t + \frac{rr'\mathcal{T}}{1 - t'\mathcal{T}}. \tag{4.12}$$

Similarly, we have

$$\mathcal{T}' = t' + \frac{rr'\mathcal{T}'}{1 - t\mathcal{T}'}. \tag{4.13}$$

The two Dyson equations can be combined into a single equation for the variable $\xi = \mathcal{T}/t = \mathcal{T}'/t'$,

$$\xi = 1 + \frac{rr'\xi}{1 - tt'\xi}. \tag{4.14}$$

At this point we invoke the Berry phase relation (4.9), which together with unitarity implies $tt' = -|t|^2 = rr' - 1$. The Dyson equation (4.14) then reduces to

$$\xi^2 = 1/|t|^2. \tag{4.15}$$

Regardless of the ambiguity in the sign of ξ, we can conclude that

$$\mathcal{T}'\mathcal{T} \equiv \xi^2 t't = -1 \Rightarrow A_n^{\text{final}} = -A_n^{\text{initial}}. \tag{4.16}$$

The end result is therefore a phase shift of π between A_n^{final} and A_n^{initial}, without any change in the magnitude. The destructive interference of A_n^{final} and A_n^{initial}, which prevents the formation of a bound state at frequency ω_c, is a direct consequence of the phase shift of π acquired in a single closed loop, even if the weight $|t|^2$ of a single loop is small.

4.4   Detection of the Destructive Interference

To detect the destructive interference, we propose a measurement of the transmission probability T of resonant tunneling of a plane wave through the photonic crystal[2]. If the confinement at $x = \pm L$ is strong, the transmission probability will have narrow resonances at the frequencies of the

---

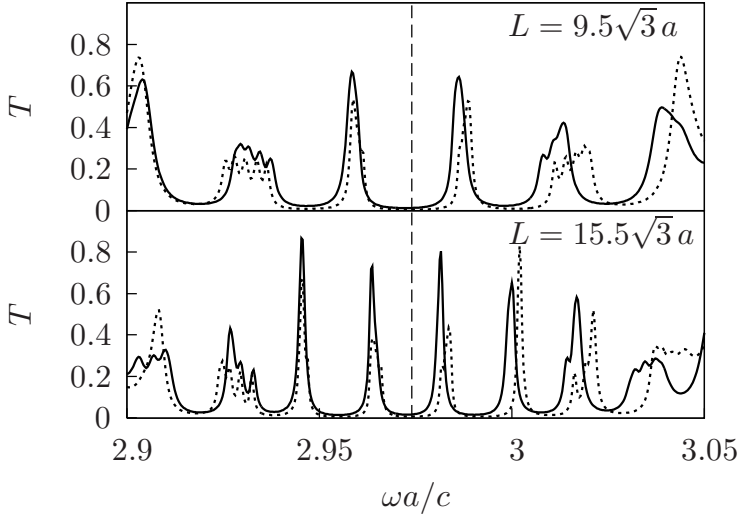[2]This was suggested to us by M. J. A. de Dood.

Figure 4.5. Frequency dependent transmission probability for two values of L in the case $\mu_R = \mu_L$ of complementary media. The solid curves show the numerical result from the Maxwell equations, while the dashed curves are calculated analytically from the Dirac equation. The vertical dashed line indicates the complementarity frequency ω_c.

quasi-bound states. The destructive interference at $\omega = \omega_c$ will produce a transmission minimum for any L. This is unlike usual Fabry-Perot resonances, which would shift with L, so that there would not be a systematic minimum or maximum at any particular frequency.

For a well-developed conical band structure we take the TE polarization (magnetic field parallel to the dielectric rods). The parameters of the photonic crystal are summarized in a footnote[3]. A 7% increment of the radius of the rods (at fixed lattice constant a) shifts ω_D and v_D by about

---

[3]The parallel dielectric rods in air that form the triangular-lattice photonic crystal (lattice constant a, dielectric constant 14) have radius $0.268\,a$ for $-L < x < 0$ and $0.288\,a$ for $0 < x < L$. (We smoothly changed the radius between these two values over an interval of order $5\,a$.) The resulting parameters of the Dirac spectrum are $\omega_D^- = 3.05\,c/a$, $v_D^- = 0.395\,c$, $\omega_D^+ = 2.91\,c/a$, $v_D^+ = 0.342\,c$. The complementarity frequency is $\omega_c = 2.974\,c/a$. The inversion symmetry is broken in the region $L < |x| < L + 10\,a$ by inserting thin rods (radius $0.08\,a$) in the unit cell, displaced by $\pm a(1/\sqrt{3}, 0)$ from the center of the thick rods (radius $0.271\,a$). The dispersion relation in that region has parameters $\omega_D = 2.973\,c/a$, $v_D = 0.313\,c$, $\mu = \pm 0.16/a$.
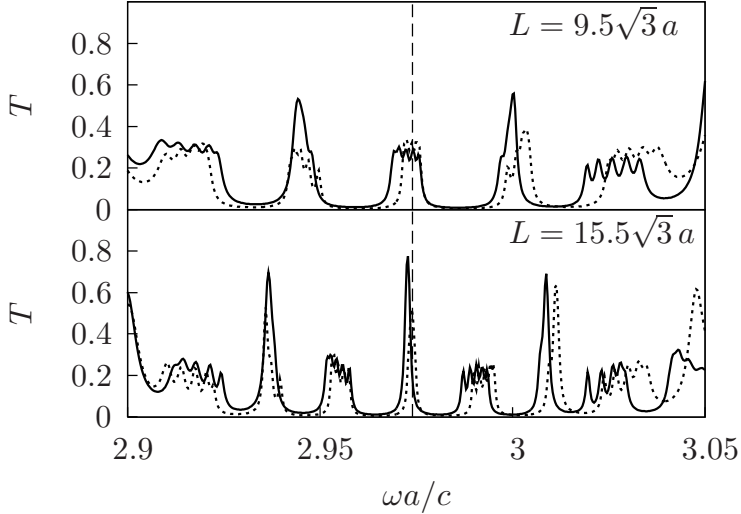
Figure 4.6.   The same as Fig. 4.5, for the case $\mu_R = -\mu_L$ when the complementarity is broken by the mass term.

5% and 15%, respectively. The mass term at $x = \pm L$ is created by breaking the inversion symmetry through the addition of an extra rod in the unit cell (see Fig. 4.1). We have solved the full Maxwell equations with the finite-difference time-domain method [56] using the MEEP software package [61]. The computational setup is similar to one from the previous chapter, described in Appendix 3.A. To reach the desired accuracy in this case our resolution has to be equal to 180 pixels per unit length or larger. This requirement makes the simulation quite heavy and time consuming. We used parallelization to get the solution in a reasonable time.

The wave vector $\boldsymbol{k} = (k, q)$ is the displacement of the wave vector of an incident plane wave from the K-point at wave vector $\boldsymbol{K} = \frac{2}{3}\pi a^{-1}(\sqrt{3}, 1)$. There are two inequivalent K-points in the hexagonal first Brillouin zone, see Fig. 4.2, and we excite a single one by orienting the lattice relative to the incident plane wave as indicated in Fig. 4.1. [The angle of incidence is spread over a narrow interval $\delta\theta \simeq 2.3°$ around $\theta = \arcsin(cK_y/\omega_c)$.] Results are shown in Fig. 4.5 (solid curves) for two values of L.

As an independent test on the accuracy of the numerical calculations, we have also calculated analytically the transmission probability from the

Dirac equation (4.1), using the transfer matrix method of Ref. [89, 95]. For simplicity we assumed in this analytical calculation an ideal coupling between the plane waves in free space and the Bloch waves in the photonic crystal. The analytical results are also plotted in Fig. 4.5 (dotted curves) and are found to agree well with the numerical results from the Maxwell equations. There are no adjustable parameters in this comparison. (The parameters ω_D, v_D, μ were extracted independently from the band structure, calculated using the MPB software package [88].)

We observe in Fig. 4.5 a transmission minimum at ω_c that does not shift with variations of L. To test our interpretation of the origin of this minimum, we have broken the complementarity of the media by inverting the sign of the mass term at the left end of the crystal. (This can be done by inverting the position of the extra rod in the unit cell.) For $q = 0$ the inversion produces an extra phase shift of π that switches the destructive interference to constructive interference — in agreement with the observed switch (see Fig. 4.6) from a transmission minimum to a transmission maximum at ω_c.

4.5   Conclusion

In conclusion, we have proposed a method to detect the pseudospin-$\frac{1}{2}$ geometric phase produced by the Dirac spectrum in a photonic crystal. The dynamical phase can be eliminated by measuring the transmission through complementary media, so that only the π geometric phase remains and a parameter-independent transmission minimum results at the complementarity frequency. Our analysis is based on the Dirac equation, which is an approximate long-wave length description, but it is fully supported by an exact numerical solution of the Maxwell equations in a triangular lattice of dielectric rods.

The experiment proposed and analysed here can be seen as the optical analogue of the detection of the geometric phase acquired during electronic cyclotron motion in graphene [93, 94]. There is one fundamental difference: In a cyclotron orbit the π phase shift is produced by $360°$ rotation of the pseudospin in the $x - y$ plane of the lattice, while in our complementary media the rotation is in the perpendicular $y - z$ plane. The

difference shows up in the dependence of the geometric phase on a mass term $\mu\sigma_z$ in the Dirac equation. A nonzero mass pushes the pseudospin out of the $x-y$ plane, thereby reducing the enclosed solid angle and hence reducing the geometric phase acquired during a cyclotron orbit [102]. In the complementary media the geometric phase remains equal to π.

In graphene, the suppression of the density of states at a *p-n* junction is analogous to the proximity effect in a normal-superconductor junction [99]. Observation of the optical counterpart presented in this chapter would open up the possibility to study superconducting analogies in non-electronic systems.

Appendix 4.A   Absence of a Bound State at the Complementarity Frequency

The demonstration of destructive interference of partial waves given in Sec. 4.3 explicitly shows how the Berry phase of π prevents the formation of a bound state at the complementarity frequency ω_c. A more formal proof, that does not rely on the partial wave decomposition, is given here.

We use again the property that if $\Psi(x)e^{iqy}$ is a solution of Eq. (4.1) at $\omega = \omega_c$, then also $\sigma_x\Psi(-x)e^{iqy}$ is a solution at the same frequency. We may therefore take even and odd superpositions of these two states to form new bound states $\Psi_\pm$ that satisfy $\sigma_x\Psi_\pm(0) = \pm\Psi_\pm(0)$. The photon flux density through the interface $x = 0$ is

$$v_D\Psi_\pm^*(0)\sigma_x\Psi_\pm(0) = \pm v_D|\Psi_\pm(0)|^2. \qquad (4.17)$$

This should vanish for a bound state, which is only possible if $\Psi_\pm(0) = 0$, meaning that the two regions $x < 0$ and $x > 0$ are decoupled. Any tunnel coupling between the two regions will result in $\Psi_\pm(0) \neq 0$, preventing the formation of a bound state at ω_c.

Chapter 5

Extinction of Coherent Backscattering by a Disordered Photonic Crystal with a Dirac Spectrum

5.1   Introduction

Coherent backscattering is a rare example of an optical interference effect that is systematically constructive in a random medium [71]. A reciprocal pair of waves (related by time reversal symmetry) arrive in phase at the observer regardless of the path length or scattering sequence. By measuring the angular profile of the diffusively reflected intensity for plane wave illumination and averaging over the random scattering, a peak is observed at a specific reflection angle [72, 73, 74]. Under optimal conditions (same polarization of incident and reflected wave, transport mean free path l much larger than wave length λ), the average peak and background intensity have ratio $\mathcal{R} = 2$ [103, 104]. This factor of two enhancement follows directly by comparing the *coherent* addition of intensities (first sum the two wave amplitudes, then square to obtain the total intensity) with the *incoherent* addition (first square, then sum).

Because coherent backscattering does not depend on the random scat-

tering phase shifts, it is a sensitive tool to probe systematic phase shifts that contain information about internal degrees of freedom of the scatterers and the photons. One example in light scattering from cold atoms is the coupling of the photon polarization to the collective spin of the atomic ensemble, which can change the constructive into a destructive interference [105, 106]. This effect is similar to the change from $\mathcal{R} = 2$ to $\mathcal{R} = 1/2$ in electronic systems with strong spin-orbit coupling [107].

A few years ago, Bliokh [75] discussed an altogether different and more dramatic switch from constructive to destructive interference: ultrarelativistic fermions (with an energy much greater than the rest energy) would have a complete extinction of coherent backscattering, so $\mathcal{R} = 0$, as a consequence of the Berry phase of π accumulated along a closed trajectory by a half-integer spin pointing in the direction of motion. Indeed, it was previously noticed by Ando et al. in the context of graphene [108, 109] that the scattering amplitude $s(\phi)$ for massless Dirac fermions vanishes when $\phi \to \pi$ (with ϕ the angle between the initial and final wave vectors $\boldsymbol{k}_i$ and $\boldsymbol{k}_f$). This absence of backscattering can be understood either in terms of the Berry phase difference of π between time reversed scattering sequences [108, 109] or in terms of the antisymmetry $S(\boldsymbol{k}_i \to \boldsymbol{k}_f) = -S(-\boldsymbol{k}_f \to -\boldsymbol{k}_i)$ of the scattering matrix of the Dirac equation [110]. Absence of backscattering in graphene might be measurable if scanning probe microscopy can provide the required angular resolution of the electron flow [111].

Here we investigate an alternative realization of the extinction of coherent backscattering that relies on photons rather than ultrarelativistic fermions. The half-integer spin required for the Berry phase of π is produced by the Dirac-type band structure of a triangular-lattice photonic crystal [28, 29, 112]. By using photons rather than electrons the difficulty of angular resolved detection is avoided. We first discuss the effect at the level of the Dirac equation, and then test the predictions with a numerical solution of the full Maxwell's equations.

5.2   Origin of the Berry Phase

We consider a photonic crystal with a two-dimensional (2D) triangular lattice structure. The hexagonal first Brillouin zone is shown in Fig. 5.1.

Haldane and Raghu [28, 29] showed that a pair of almost degenerate envelope Bloch waves $(\Psi_1, \Psi_2) \equiv \Psi$ near a corner of the Brillouin zone can be represented by a pseudospin, coupled to the orbital motion. On length scales large compared to the lattice constant a and for frequencies near the degeneracy frequency ω_D, the wave equation reduces to

$$\left(-i\sigma_x \frac{\partial}{\partial x} - i\sigma_y \frac{\partial}{\partial y}\right)\Psi = \frac{\omega - \omega_D}{v_D}\Psi, \qquad (5.1)$$

with Pauli matrices σ_x, σ_y. This is the 2D Dirac equation of a spin-$\frac{1}{2}$ particle with zero mass and group velocity v_D (of order $a\omega_D$). The dispersion relation

$$(\omega - \omega_D)^2 = v_D^2(k_x^2 + k_y^2) \qquad (5.2)$$

has a double cone with a degeneracy at frequency ω_D (the so-called Dirac point).

The Berry phase associated with the pseudospin degree of freedom was calculated in Ref. [112]. The solution of Eq. (5.1) with a definite wave vector $\boldsymbol{k} = (k_x, k_y)$ is

$$\Psi = \mathcal{C}^{-1/2}\begin{pmatrix} (\omega - \omega_D)/v_D \\ k_x + ik_y \end{pmatrix} \equiv \begin{pmatrix} \cos(\theta/2) \\ e^{i\phi}\sin(\theta/2) \end{pmatrix}, \qquad (5.3)$$

with $\mathcal{C}$ a normalization constant. The angles ϕ, θ define the Bloch vector $(\cos\phi\sin\theta, \sin\phi\sin\theta, \cos\theta)$, representing the direction of the pseudospin on the Bloch sphere. Because of the dispersion relation (5.2) the angle $\theta = \pi/2$, so the Bloch vector lies in the $x - y$ plane, pointing in the direction of $\boldsymbol{k}$. The Berry phase ϕ_B is one half the solid angle subtended at the origin by the rotating Bloch vector. A rotation of $\boldsymbol{k}$ by $360°$ in the $x - y$ plane thus produces a Berry phase $\phi_B = \pi$.

5.3   Analytical Results

Because of refraction at the interfaces $x = 0$ and $x = L$ between the photonic crystal and air, we need to distinguish the initial and final wave vectors $\boldsymbol{k}_i, \boldsymbol{k}_f$ of envelope Bloch waves inside the crystal (velocity v_D) from the corresponding values $\boldsymbol{k}_i^{\mathrm{air}}, \boldsymbol{k}_f^{\mathrm{air}}$ of plane waves outside (velocity c). For
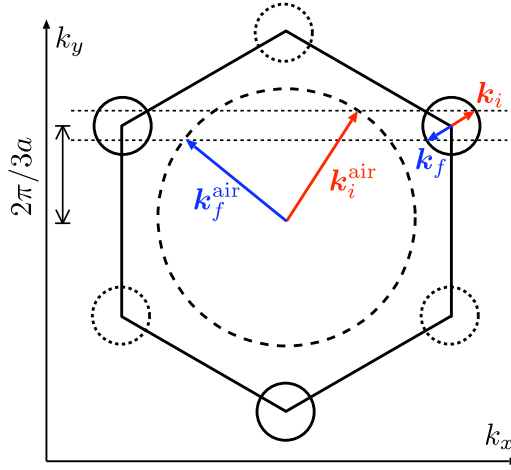
Figure 5.1.   Hexagonal first Brillouin zone of a two-dimensional triangular lattice photonic crystal, with equifrequency contours centered at the corners. The three solid circles are related by translation over a reciprocal lattice vector, so they are equivalent, while scattering from a solid to a dotted circle is suppressed if the scattering potential is smooth on the scale of the lattice constant a. The large dashed circle at the center is the equifrequency contour in air, included to indicate the refraction at the air-crystal interface (as expressed by Eq. (5.4)).

the crystallographic orientation shown in Fig. 5.1, the wave vectors before and after refraction (at a given frequency ω) are related by [89, 95]

$$k_y^{\mathrm{air}} = k_y + 2\pi/3a, \tag{5.4a}$$

$$c^2(k^{\mathrm{air}})^2 - \omega^2 = 0 = v_D^2 k^2 - (\omega - \omega_D)^2, \tag{5.4b}$$

with a the lattice constant and ω_D the frequency of the Dirac point. We denote $k^{\mathrm{air}} = |\boldsymbol{k}^{\mathrm{air}}|$ and $k = |\boldsymbol{k}|$.

Before considering the diffuse reflection from the disordered photonic crystal, we address the specular reflection from the air-crystal interface that is present even without any disorder. A plane wave incident at an angle

$$\theta = \arcsin(ck_{i,y}^{\mathrm{air}}/\omega) = \arcsin(2\pi c/3\omega a + ck_{i,y}/\omega) \tag{5.5}$$

is specularly reflected at an angle $\theta_{\mathrm{spec}} = \pi - \theta$. The interface reflectivity R_{int} (the fraction of the incident photon flux that is specularly reflected)
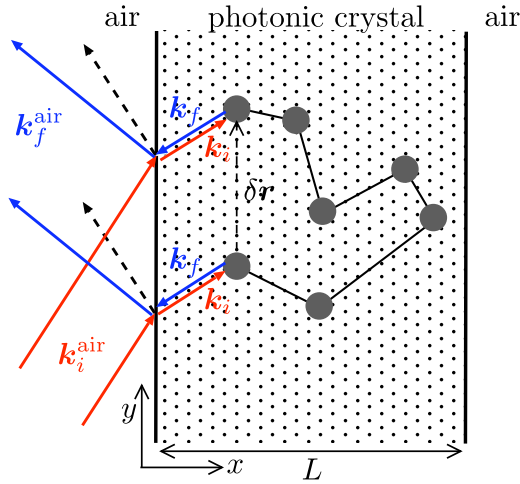
Figure 5.2. A pair of reciprocal waves that interfere destructively, resulting in the extinction of coherent backscattering. Arrows at the air-crystal interface indicate the incident plane wave (red solid lines), the diffusively reflected wave (blue solid lines), and the specularly reflected wave (black dashed lines). The two initial waves (wave vector $\boldsymbol{k}_i^{\mathrm{air}}$, refracted to $\boldsymbol{k}_i$) follow time-reversed sequences of scattering events (dark circles), to end up in two final waves (wave vector $\boldsymbol{k}_f$, refracted to $\boldsymbol{k}_f^{\mathrm{air}}$) with a phase difference of $\pi + (\boldsymbol{k}_i + \boldsymbol{k}_f) \cdot \delta \boldsymbol{r}$. For $\boldsymbol{k}_f = -\boldsymbol{k}_i$ only the Berry phase difference of π remains. As a consequence of this destructive interference, the intensity of the reflected wave indicated in blue is suppressed. By measuring the angular profile of the average reflected intensity a minimum of nearly zero intensity will result at this angle.

follows from the transfer matrix of the air-crystal interface calculated in Ref. [89, 95]. In the approximation of maximal coupling we find

$$R_{\mathrm{int}}(k_y) = \frac{1 - \sqrt{1 - (k_y/k)^2}}{1 + \sqrt{1 - (k_y/k)^2}}, \tag{5.6}$$

hence the interface reflectivity is zero for $k_y = 0$. Numerical solutions of Maxwell's equations [89, 95] give $R_{\mathrm{int}}(0) \simeq 0.05$ for ω near ω_D, so this is a reasonably accurate approximation.

Disorder inside the photonic crystal produces a background of diffusively reflected waves in an angular opening $\delta\theta \simeq k/k^{\mathrm{air}} \ll 1$ around $\theta_0 = \pi - \arcsin(2\pi c/3\omega a)$. The reciprocity angle θ_* for coherent backscat-

tering is related to the incident angle θ of Eq. (5.5) by

$$\theta_* = \pi - \arcsin(2\pi c/3\omega a - c k_{i,y}/\omega). \qquad (5.7)$$

We will choose $k_{i,y}$ small ($\ll k$) but nonzero, so that $R_{\text{int}} \ll 1$ while still coherent backscattering at angle θ_* can be resolved from specular reflection at angle θ_{spec}.

The extinction of coherent backscattering by destructive interference of reciprocal waves is illustrated in Fig. 5.2. The two series of time reversed scattering events $S_+ = \boldsymbol{k}_i \to \boldsymbol{k}_1 \to \boldsymbol{k}_2 \to \cdots \to \boldsymbol{k}_{n-1} \to \boldsymbol{k}_n \to -\boldsymbol{k}_i$ and $S_- = \boldsymbol{k}_i \to -\boldsymbol{k}_n \to -\boldsymbol{k}_{n-1} \to \cdots \to -\boldsymbol{k}_2 \to -\boldsymbol{k}_1 \to -\boldsymbol{k}_i$ have the same scattering amplitude up to a Berry phase difference $\phi_B = \pi$ [75, 108, 109]. This destructive interference suppresses the reflected intensity at angle θ_*. If the final wave vector $\boldsymbol{k}_f$ deviates from the exact backscattering direction $-\boldsymbol{k}_i$, the phase difference $\Delta\phi = \phi_B + (\boldsymbol{k}_i + \boldsymbol{k}_f) \cdot \delta\boldsymbol{r}$ depends on the separation $\delta\boldsymbol{r}$ of the first and last scattering events [103]. The Berry phase difference ϕ_B remains equal to π, because both the Berry phases accumulated along S_+ and S_- are incremented by the same amount (half the angle between $\boldsymbol{k}_f$ and $-\boldsymbol{k}_i$).

By including the Berry phase in the theory [71, 103, 104] of coherent backscattering of scalar waves in the weak scattering regime ($l \gg \lambda$), it follows that the incoherent part R_0 of the reflectivity R remains unaffected while the interference part δR acquires an overall factor $\cos\phi_B$ [75]:

$$R = R_0 + \delta R \cos\phi_B. \qquad (5.8)$$

The entire angular profile of coherent backscattering in the Dirac equation (where $\phi_B = \pi$) may therefore be obtained, for $l \gg \lambda$, by simply changing the sign of the known results for δR for scalar waves (where $\phi_B = 0$). In particular, for $k_{i,y} \ll k$ and $\delta k = k_{f,y} + k_{i,y} \ll 1/l$ one has

$$R_0 = \frac{1}{\pi N}(1 + z_0/l)\left(1 - \frac{l + z_0}{L + 2z_0}\right), \qquad (5.9)$$

$$\begin{aligned} \delta R = &\frac{1}{\pi N}(1 + z_0/l) \\ &\times \left\{1 - (l + z_0)\delta k \coth[\delta k(L + 2z_0)]\right\}. \end{aligned} \qquad (5.10)$$

The normalization factor $N = kW/2\pi$ is chosen such that R is the fraction of the incident photon flux which is reflected in a single transverse mode when $k_{f,y} = 2\pi n/W$ ($n = 0, \pm 1, \pm 2, \ldots$) is discretized by periodic boundary conditions at $y = 0$ and $y = W$. (This normalization is chosen to simplify the comparison with the numerical calculations described later on.)

Eqs. (5.9) and (5.10) are approximate results from the radiative transfer equation, accurate for a disordered slab of thickness L not much smaller than the transport mean free path l. The parameter z_0, the so-called extrapolation length, depends on the reflectivity R_{int} of the interface between the photonic crystal and vacuum, according to [113]

$$z_0 = \tfrac{1}{4}\pi l \frac{1 + C_2}{1 - C_1}, \quad C_1 = \frac{1}{k}\int_0^k R_{\text{int}}(k_y)dk_y, \tag{5.11a}$$

$$C_2 = \frac{4}{\pi}\int_0^k \sqrt{1 - (k_y/k)^2}\, R_{\text{int}}(k_y)dk_y. \tag{5.11b}$$

Substitution of Eq. (5.6) gives the simple answer $z_0 = l$ for the extrapolation length of the air-crystal interface.

Collecting results, we arrive at the following line shape of the reflectivity near the reciprocity angle:

$$R = \frac{4}{\pi N}\left(l\delta k \coth[\delta k(L + 2l)] - \frac{l}{L + 2l}\right)$$
$$\rightarrow \frac{4}{3\pi N}(Ll + 2l^2)\delta k^2 \quad \text{for} \quad \delta k \rightarrow 0. \tag{5.12}$$

The suppression (5.12) of the reflected intensity within a narrow angular opening $\delta\theta \simeq 1/kl$ around the reciprocity angle θ_* is compensated by an excess intensity $\delta R \simeq 1/kl$ of the diffusively reflected wave at angles away from θ_*. This compensation is required by current conservation [114], but difficult to observe for $kl \gg 1$. We will therefore not consider it in what follows.

5.4   Comparison with Numerics

We now compare the analytical predictions from the Dirac equation with a numerical solution of Maxwell's equations. As in earlier work [89, 95], we use the MEEP software package [61] to solve Maxwell's equations in the time domain [56] for a continuous plane wave source (time dependence $\propto e^{i\omega t}$) switched on gradually. We calculate the reflected intensity, projected onto transverse modes, as a function of time and take the large time limit to obtain the stationary reflectivity R. We took the time sufficiently large that the sum of the total transmission and total reflection differs from unity by less than 0.03.

The photonic crystal consists of a triangular lattice of parallel dielectric rods (dielectric constant 8.9, radius $\rho_0 = 0.3\,a$) in air. The orientation of the lattice is as shown in Fig. 5.2. The magnetic field is taken parallel to the rods (TE polarization). The conical singularity in the band structure is at frequency $\omega_D = 3.03\,c/a$, with a slope $d\omega/dk \equiv v_D = 0.432\,c$. We discretize the transverse wave vector by means of periodic boundary conditions: $k_y = 2\pi n/W$, $n = 0, \pm 1, \pm 2, \ldots$, with $W = 1200\,a$. The longitudinal dimension of the lattice is taken at $L = 60\sqrt{3}\,a$ (corresponding to 121 rows of dielectric rods). The frequency ω of the incident plane wave is chosen such that $\omega - \omega_D = 0.206\,c/a$ is sufficiently large that $N = 88 \gg 1$, but sufficiently small that the trigonal distortion of the circular equifrequency contours is insignificant.

Disorder is introduced by randomly varying the radius $\rho(\boldsymbol{r})$ of the dielectric rods at position $\boldsymbol{r}$, according to $\rho(\boldsymbol{r}) = \rho_0 + \delta\rho(\boldsymbol{r})$. The variation $\delta\rho(\boldsymbol{r})$ is spatially correlated over a length ξ in a Gaussian manner,

$$\delta\rho(\boldsymbol{r}) = \sum_{i=1}^{\mathcal{N}} A_i \exp(-|\boldsymbol{r} - \boldsymbol{r}_i|^2/2\xi^2), \tag{5.13}$$

where $\boldsymbol{r}_i$ $(i = 1, 2, \ldots \mathcal{N})$ is a randomly chosen point in the crystal and A_i is a randomly chosen amplitude in the interval $(-\Delta, \Delta)$. We took $\mathcal{N} = 3200$, $\Delta = 0.04\,a$, $\xi = 2a$. It is essential that the correlation length ξ of the disorder is larger than the lattice constant a to minimize scattering between the two inequivalent corners of the Brillouin zone (solid and
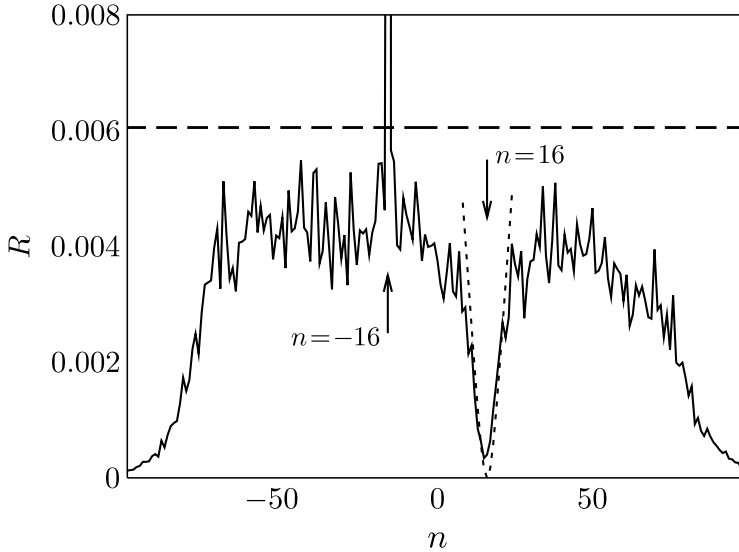
Figure 5.3. Plot of the reflectivity R (fraction of incident flux reflected in a single transverse mode) as a function of the transverse mode index n (related to the transverse wave vector by $k_{f,y} = 2\pi n/W$). The specularly reflected flux is at $n = -16$ and the extinction of coherent backscattering is at $n = +16$ (indicated by arrows). The curve is calculated numerically from Maxwell's equations. The dashed and dotted lines are, respectively, the analytical predictions (5.9) and (5.12) for the incoherent background and the line shape near the extinction angle, for a transport mean free path of $l = 10\,a$.

dashed circles in Fig. 5.1). For these disorder parameters we found that only about 2% of the incident flux is reflected into the opposite corner.

The numerical data in Fig. 5.3 is for the incident wave vector $k_{i,y} = -32\,\pi/W$, averaged over 80 realizations of the disorder. The angle of incidence (measured relative to the positive x-axis) is $\theta = 0.67\,\mathrm{rad} = 38.4°$. The specularly reflected wave at an angle $\theta_{\mathrm{spec}} = \pi - \theta = 2.47\,\mathrm{rad} = 141.5°$ has transverse mode number $n = -16$. The reciprocity angle (5.7) is $\theta^* = 2.40\,\mathrm{rad} = 137.5°$, corresponding to the mode number $n = +16$.

Both the specularly reflected wave at $n = -16$ and the extinction of the coherent backscattering at $n = +16$ are clearly visible in Fig. 5.3. The extinction at the reciprocity angle is not complete, presumably because of scattering between inequivalent corners of the Brillouin zone. The analytical theory predicts a parabolic line shape of the reflectivity around

the reciprocity angle, given by Eq. (5.7), the width of which depends on the value of the transport mean free path l. A fit to the numerical data gives $l = 10\,a$ (dotted curve in Fig. 5.3), which then implies a background of incoherent diffuse reflection at a value $R_0 \approx 0.006$ which is somewhat larger than the numerical data (dashed horizontal line).

5.5   Conclusion

In conclusion, we have shown that coherent backscattering of radiation from a disordered triangular lattice photonic crystal is extinguished at an angle that is reciprocal to the angle of incidence. This effect has an analogue for electrons [75, 108, 109], but it should be easier to observe for photons because angular resolved detection is more feasible. The observation of the extinction of coherent backscattering would be a striking demonstration of a spin-1/2 Berry phase in a disordered optical system.

Appendix 5.A   Details of the Numerical Calculations

The computational setup we use in this chapter to calculate the reflected intensity versus transverse wave vector is similar to what we used in the previous two chapters (see Appendix 3.A for details). There are, however, several important differences we discuss here.

As opposed to the previous cases where we could make use of the periodicity and perform transmission measurements on one unit cell, the computational cell width in this case is taken to be the same as the actual system width W, which equals 1200 unit lengths (lattice spacing a is one unit length). The waves scatter by disorder impurities, change their direction of propagation and move in both two dimensions. We use periodic boundary conditions and choose the width large enough, so that the discretization of the transverse wave vector $k_{y_n} = 2\pi n/W$ (where $n = 0, \pm 1, \pm 2, \dots$) is sufficiently fine to resolve the dip in the reflected intensity profile. A resolution of 20 pixels per unit length in combination

with subpixel averaging suffice for our accuracy requirements. We also make use of parallelization to obtain results in relatively short time.

We utilize a continuous in time line source switched on gradually. The gradual switching on prevents an appearance of high frequencies that are more weakly absorbed by PML boundaries. We stop the simulation when the wave propagates through the structure and the flow becomes steady (the sum of transmission and reflection is ≥ 0.97). Then the y component of the electric field E_λ^{full} and the z component of the magnetic field H_λ^{full} are output along a line in the y direction in front of the structure. The subscript $\lambda = \overline{1, \Lambda}$ labels mesh points of the computational domain and

$$\Lambda = 1 + W(\text{in units of unit lengths}) \times \text{resolution} \qquad (5.14)$$

is the total number of points along y direction.

The simulation is run again with an empty computational domain (normalization run). The normalization run is stopped at the same time as the run with the structure. We output the field components E_λ^{norm} and H_λ^{norm} along the same line (the same x coordinate) as before and subtract them from the fields of the run with the structure. Remaining fields are the fields of the reflected wave:

$$E_\lambda = E_\lambda^{\text{full}} - E_\lambda^{\text{norm}}, \quad H_\lambda = H_\lambda^{\text{full}} - H_\lambda^{\text{norm}}. \qquad (5.15)$$

Further, we process the field values using the orthogonality of modes in the periodic waveguide to determine the reflectivity R_m as a function of mode index. In the periodic two-dimensional waveguide the TE mode fields of a reflected wave at some fixed time t' and fixed coordinate x' are given by

$$\boldsymbol{H}(y) = \sum_{n=-\infty}^{\infty} \alpha_n \hat{z} e^{i(\omega t' + k_{x_n} x' - k_{y_n} y)},$$

$$\boldsymbol{E}(y) = \sum_{n=-\infty}^{\infty} (-\alpha_n \frac{ck_{y_n}}{\omega} \hat{x} - \alpha_n \frac{ck_{x_n}}{\omega} \hat{y}) e^{i(\omega t' + k_{x_n} x' - k_{y_n} y)}, \qquad (5.16)$$

where k_{x_n} is the wave vector along the x axis $k_{x_n} = \sqrt{\omega^2/c^2 - k_{y_n}^2}$ and

α_n are complex amplitudes. The fields belonging to different modes can be projected out from the sums (5.16) using orthogonality of modes, that is any field component F_m of mth mode can be obtained as:

$$F_m = \frac{e^{-ik_{y_m}y}}{W} \int\limits_0^W F e^{ik_{y_m}y} \, dy. \tag{5.17}$$

The flux is given by the integral over the width of the x projection of the Poynting vector:

$$P = \int\limits_0^W s_x \, dy = \frac{c}{8\pi} \int\limits_0^W \left[\text{Re}(E_y H_z) + \text{Re}(E_y^* H_z) \right] \, dy. \tag{5.18}$$

Inserting (5.16) into (5.18) we get

$$P = \frac{cW}{8\pi} \text{Re} \sum_{n=-\infty}^{\infty} \alpha_n \alpha_{-n} \frac{ck_{x_n}}{\omega} e^{2i(\omega t' - k_{x_n}x')} + \frac{cW}{8\pi} \sum_{n=-\infty}^{\infty} |\alpha_n|^2 \frac{ck_{x_n}}{\omega}. \tag{5.19}$$

The first term in this formula comes from the interference between nth and $-n$th modes. This term depends on time and drops out after averaging over a time period. However, we do not have to do the time averaging as we are interested in a single mode flux P_m, which does not depend on time:

$$P_m = \frac{c}{8\pi} \int\limits_0^W \text{Re} \left[E_{y_m}^* H_{z_m} \right] \, dy. \tag{5.20}$$

Here $E_{y_m}^*$ and H_{z_m} are field components belonging to mode m. The total incident flux through the waveguide does not depend on time either, because the incident wave is in a single mode. Collecting equations (5.17), (5.18) and (5.20) we arrive at the reflectivity as a function of

mode index:

$$R_m = P_m/P^{\text{norm}},$$

$$P_m = \frac{c}{8\pi W} \int_0^W H_z e^{ik_{ym}y}\, dy \int_0^W E_y^* e^{-ik_{ym}y}\, dy,$$

$$P^{\text{norm}} = \frac{c}{8\pi} \int_0^W \text{Re}\left[H_z^{\text{norm}} \left(E_y^{\text{norm}} \right)^* \right]\, dy. \tag{5.21}$$

Finally, we compute R_m according to formulas (5.21) and using the output fields (5.15), that is:

$$R_m = \frac{\displaystyle\sum_{\lambda=1}^{\Lambda-1} E_\lambda^* e^{-ik_{ym}(\lambda-1)\Delta y} \sum_{\nu=1}^{\Lambda-1} H_\nu e^{ik_{ym}(\nu-1)\Delta y}}{(\Lambda-1)\displaystyle\sum_{\lambda=1}^{\Lambda-1} \text{Re}\left[H_\lambda^{\text{norm}} \left(E_\lambda^{\text{norm}} \right)^* \right]}, \tag{5.22}$$

where Λ is the total number of mesh points along y direction in the computational domain (given by formula (5.14)) and $\Delta y = (1/\text{resolution})$ is the distance between two neighboring points. The summation runs to $\Lambda - 1$ because the fields at $y = 0$ ($i = 1$) are the same as at $y = W$ ($i = \Lambda$), since periodic boundary conditions are used. The fields at both boundaries contribute to sum (5.22) with 1/2 weights, so together their contribution is represented by the first term ($i = 1$) in the sum.

Chapter 6

Quantum Goos-Hänchen Effect in Graphene

6.1 Introduction

Analogies between optics and electronics have inspired the research on graphene since the discovery of this material a few years ago [27]. Some of the more unusual analogies are drawn from the field of optical metamaterials. In particular, negative refraction in a photonic crystal [19] has an analogue in a bipolar junction in graphene if the width d of the p-n interface is less than the electron wave length λ_F [100]. Negative refraction is only possible for angles of incidence α less than a critical angle α_c. For $\alpha > \alpha_c$ the refracted wave becomes evanescent and the incident wave is totally reflected with a shift σ of order λ_F along the interface. This wave effect is known as the Goos-Hänchen effect [115], after the scientists who first measured it in 1947. The GH effect was already predicted in Newton's time and has become a versatile probe of surface properties in optics, acoustics, and atomic physics [116]. In particular, the interplay of the GH effect and negative refraction plays an important role in photonic crystals and other metamaterials [117, 118].

The electronic analogue of the GH effect has been considered previously [119, 120, 121, 122], including relativistic corrections, but not in the ultrarelativistic limit of massless electrons relevant for graphene. As we

will show here, the shift of a beam upon reflection at a p-n interface in graphene is strongly dependent on the sublattice (or "pseudospin") degree of freedom — both in magnitude and sign. We calculate the average shift σ after multiple reflections at opposite p-n interfaces and (contrary to a recent expectation [123][1]) we find that σ changes sign at $\alpha^* = \arcsin\sqrt{\sin\alpha_c}$. In search for an observable consequence of the GH effect we study the conductance of the p-n-p junction, for current parallel to the interfaces (see Fig. 6.1). We find that the lowest mode in the n-doped channel has a twofold degeneracy, observable as an $8e^2/h$ stepwise increase in the conductance as a function of channel width.

We recall some basic facts about the carbon monolayer called graphene [99, 55]. Near the corners of the Brillouin zone the electron energy depends linearly on the momentum, like the energy-momentum relation of a photon (but with a velocity v that is 300 times smaller). The corresponding wave equation is formally equivalent to the Dirac equation for massless spin-1/2 particles in two dimensions. The spin degree of freedom is not the real electron spin (which is decoupled from the dynamics), but a pseudospin variable that labels the two carbon atoms (A and B) in the unit cell of a honeycomb lattice.

6.2   General Formula for the Goos-Hänchen Shift

To calculate the GH shift we consider a beam,

$$\mathbf{\Psi}^{\text{in}}(x,y) = \int_{-\infty}^{\infty} dq\, f(q - \bar{q}) e^{iqy + ik(q)x} \begin{pmatrix} e^{-i\alpha(q)/2} \\ e^{i\alpha(q)/2} \end{pmatrix}, \qquad (6.1)$$

incident on a p-n interface at $x = 0$ from an n-doped region $x < 0$. The spinor wave function $\mathbf{\Psi} = (\Psi_+, \Psi_-)$ has pseudospin component Ψ_+ and Ψ_- on the A and B sublattices. We require that $\mathbf{\Psi}^{\text{in}}$ is a solution of the

---

[1]These authors find a GH shift σ in graphene which disagrees both in magnitude and sign with our Eq. (6.14). The reason is that the simple relation (6.9) between σ and the reflection amplitude r holds only in a basis such that the product of the upper and lower spinor components is real. Zhao and Yelin use a basis with spinor components $(1, e^{i\alpha})$ for the incident wave and $(1, -e^{-i\alpha})$ for the reflected wave. This change of basis changes the reflection amplitude, $r \mapsto \tilde{r} \equiv -ie^{i\alpha}r$, so that instead of Eq. (6.9) they should have used $\sigma = -\text{Im}\,(d/dq)\ln\tilde{r} + d\alpha/dq$.
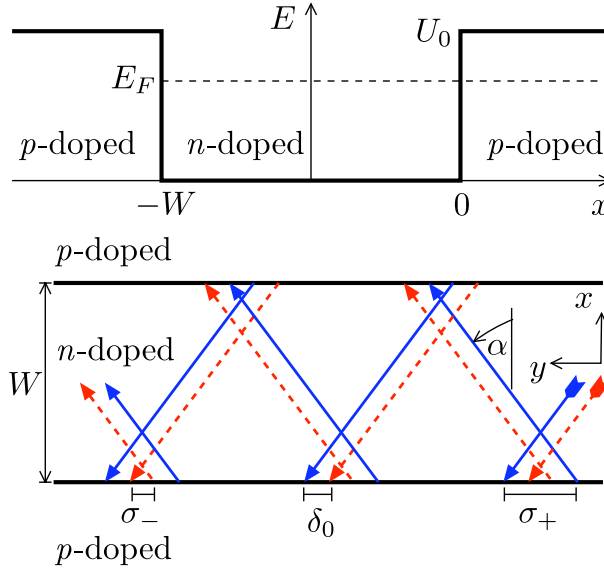
Figure 6.1. Upper panel: Potential profile of an n-doped channel between p-doped regions. Lower panel: Top view of the channel in the graphene sheet. The blue solid line follows the center of a beam on the A sublattice, while the red dashed line follows the center on the B sublattice. The two centers have a relative displacement δ_0. Upon reflection, each pseudospin component experiences alternatingly large and small shifts $\sigma_{\pm}$.

Dirac equation,

$$\left(-i\hbar v\sigma_x\frac{\partial}{\partial x} - i\hbar v\sigma_y\frac{\partial}{\partial y} + U\right)\Psi = E\Psi, \tag{6.2}$$

with $U = 0$ (zero potential in the n-doped region) and $E = E_F$ (the Fermi energy). This requirement fixes the dependence of the longitudinal wave vector k and the angle of incidence α on the transverse wave vector q,

$$k = \sqrt{(E_F/\hbar v)^2 - q^2}, \quad \alpha = \arcsin(\hbar vq/E_F). \tag{6.3}$$

For brevity, we will set $\hbar v \equiv 1$ in some intermediate equations (restoring units in the final answers).

The transverse wave vector profile $f(q - \bar{q})$ of the beam is peaked at some $\bar{q} \in (0, E_F/\hbar v)$, corresponding to an angle of incidence $\bar{\alpha} =$

$\arcsin(\bar{q}/E_F) \in (0, \pi/2)$. None of our results depend on the shape of the profile, but for definiteness we take a Gaussian,

$$f(q - \bar{q}) = \exp[-\tfrac{1}{2}(q - \bar{q})^2/\Delta_q^2], \tag{6.4}$$

of width Δ_q.

For Δ_q small compared to the Fermi wave vector $k_F = E_F/\hbar v$ we may expand $k(q)$ and $\alpha(q)$ to first order around $\bar{q}$, substitute in Eq. (6.1), and evaluate the Gaussian integral to obtain the spatial profile of the incident beam. At the interface $x = 0$ the two components $\Psi_\pm^{\text{in}} \propto \exp[-\tfrac{1}{2}\Delta_q^2(y - \bar{y}_\pm^{\text{in}})^2]$ of $\boldsymbol{\Psi}^{\text{in}}(0, y)$ are Gaussians of the same width $\Delta_y = 1/\Delta_q$, centered at two different mean y-coordinates

$$\bar{y}_\pm^{\text{in}} = \pm\tfrac{1}{2}\alpha'(\bar{q}) = \pm\tfrac{1}{2}(k_F \cos \bar{\alpha})^{-1}. \tag{6.5}$$

(The prime in α' indicates the derivative with respect to q.) The separation

$$\delta_0 = |\bar{y}_+^{\text{in}} - \bar{y}_-^{\text{in}}| = (k_F \cos \bar{\alpha})^{-1} \tag{6.6}$$

of the two centers is of the order of the Fermi wave length $\lambda_F = 2\pi/k_F$, which is small compared to the width Δ_y but of the same order of magnitude as the GH shift — so it cannot be ignored.

Similar considerations are now applied to the reflected wave,

$$\boldsymbol{\Psi}^{\text{out}} = \int_{-\infty}^{\infty} dq\, f(q - \bar{q}) e^{iqy - ik(q)x} r(q) \begin{pmatrix} -ie^{i\alpha(q)/2} \\ ie^{-i\alpha(q)/2} \end{pmatrix}, \tag{6.7}$$

obtained from the incident wave (6.1) by the replacements $k \mapsto -k$, $\alpha \mapsto \pi - \alpha$ and multiplication with the reflection amplitude $r(q) = |r(q)|e^{i\phi(q)}$. The two components $\Psi_\pm^{\text{out}}$ of $\boldsymbol{\Psi}^{\text{out}}(0, y)$ at the interface are Gaussians centered at

$$\bar{y}_\pm^{\text{out}} = -\phi'(\bar{q}) \mp \tfrac{1}{2}\alpha'(\bar{q}) = -\phi'(\bar{q}) \mp \tfrac{1}{2}(k_F \cos \bar{\alpha})^{-1}. \tag{6.8}$$

Comparison with Eq. (6.5) shows that the first component of the spinor is displaced along the interface by an amount $\sigma_+ = y_+^{\text{out}} - y_+^{\text{in}} = -\phi'(\bar{q}) - \delta_0$, while the second component is displaced by $\sigma_- = y_-^{\text{out}} - y_-^{\text{in}} = -\phi'(\bar{q}) + \delta_0$.

The average displacement,

$$\sigma = \tfrac{1}{2}(\sigma_+ + \sigma_-) = -\phi'(\bar{q}) = -\mathrm{Im}\,\frac{d}{dq}\ln r, \tag{6.9}$$

is the GH shift. As illustrated in Fig. 6.1, after N reflections the two components of the spinor are displaced by the same amount $N\sigma$ if N is even and by a different amount $N\sigma \mp \delta_0$ if N is odd. For $N \gg 1$ the difference $2\delta_0$ between the two displacements becomes small compared to the average shift $N\sigma$.

6.3   Goos-Hänchen Shift upon Reflection from a *p-n* Interface

The formula (6.9) for the GH shift is generally valid for reflection from any interface. To apply it to the step function *p-n* interface we calculate the reflection amplitude by matching $\mathbf{\Psi}^{\mathrm{in}} + \mathbf{\Psi}^{\mathrm{out}}$ at $x = 0$ to the evanescent wave

$$\mathbf{\Psi}^{\mathrm{ev}} = \int_{-\infty}^{\infty} dq\,C(q)e^{iqy-\kappa(q)x}\begin{pmatrix} i(U_0 - E_F) \\ \kappa(q) + q \end{pmatrix}, \tag{6.10}$$

$$\kappa = \sqrt{q^2 - (\hbar v)^{-2}(E_F - U_0)^2}. \tag{6.11}$$

This is a solution of the Dirac equation (6.2) (with $U = U_0$ and $E = E_F$) that decays into the *p*-doped region $x > 0$ for $\hbar v|q| > |E_F - U_0|$.

Continuity of the wave function at $x = 0$ allows us to eliminate the unknown function $C(q)$ and to obtain the reflection amplitude,

$$r = \frac{ie^{i\alpha}(E_F - U_0) + \kappa + q}{E_F - U_0 + ie^{i\alpha}(\kappa + q)}. \tag{6.12}$$

The modulus $|r| = 1$ for angles of incidence

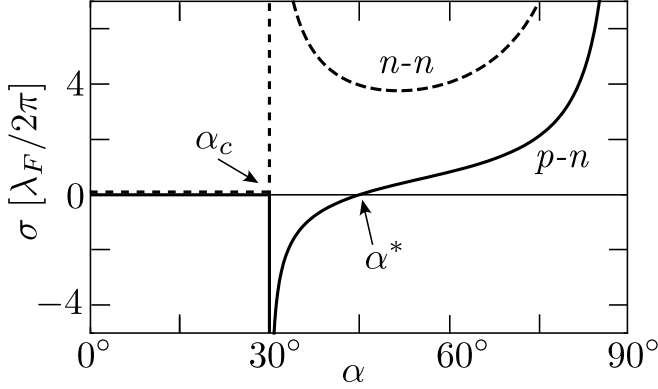$$\alpha > \alpha_c \equiv \arcsin|U_0/E_F - 1| \tag{6.13}$$

Figure 6.2. Dependence on the angle of incidence α of the GH shift σ, calculated from Eq. (6.14) for $U_0/E_F = 1.5$ (solid curve, p-n interface) and for $U_0/E_F = 0.5$ (dashed curve, n-n interface). The critical angle for total reflection (below which $\sigma = 0$) equals $\alpha_c = 30°$ in both cases. The sign-change angle $\alpha^* = 45°$ for $U_0/E_F = 1.5$.

such that there is total reflection[2]. Substitution into Eq. (6.9) then gives the GH shift,

$$
\begin{aligned}
\sigma &= \frac{\sin^2 \alpha + 1 - U_0/E_F}{\kappa \sin \alpha \cos \alpha} \\
&= \frac{\lambda_F}{\pi \sin 2\alpha} \frac{\sin^2 \alpha - \operatorname{sign}(U_0 - E_F) \sin \alpha_c}{\sqrt{\sin^2 \alpha - \sin^2 \alpha_c}}.
\end{aligned}
\tag{6.14}
$$

A negative GH shift (in the backward direction) appears at a p-n interface (when $E_F < U_0$) for angles of incidence

$$
\alpha_c < \alpha < \alpha^* \equiv \arcsin \sqrt{\sin \alpha_c}.
\tag{6.15}
$$

For $\alpha > \alpha^*$ the GH shift is positive (in the forward direction), regardless of the relative magnitude of E_F and U_0. In Fig. 6.2 we have plotted the α dependence of σ for two representative cases.

The product $\sigma \cos \alpha \equiv \sigma_\perp$ is the shift in the direction perpendicular

---

[2]For $|\alpha| < \alpha_c$ one has $\kappa = -i\sqrt{(E_F - U_0)^2 - q^2}$ and $|r| < 1$, because part of the incident wave is transmitted. One can readily check, by substitution into Eq. (6.9), that $\sigma = 0$ for these subcritical angles. As expected, there is no Goos-Hänchen shift without an evanescent wave.
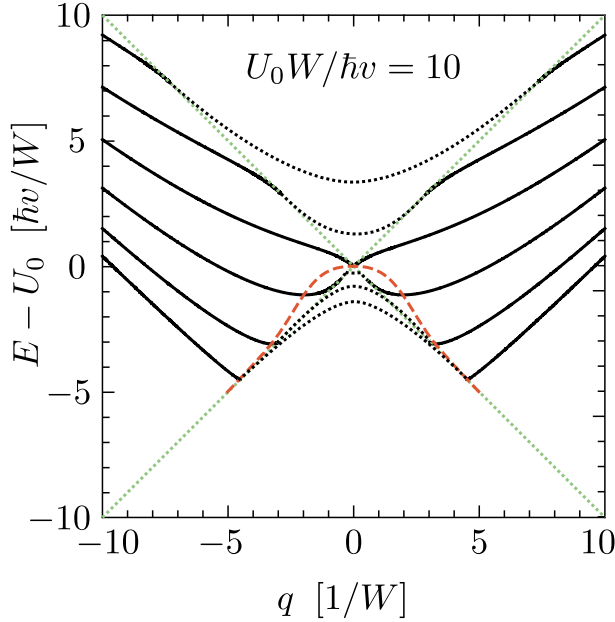
Figure 6.3.   Energy E of waves propagating with wave vector q in the y-direction, bounded in the channel $-W < x < 0$ by the potential profile in Fig. 6.1. The different curves (black solid lines) correspond to different modes. (Only the six lowest channel modes are shown.) The curves are calculated from Eq. (6.22) for $U_0 W/\hbar v = 10$ (semiclassical regime). The velocity $v_\parallel = dE/\hbar dq$ in the y-direction vanishes at the minima of the dispersion relation, given by Eq. (6.18) (red dashed curve). At the (green) dotted lines $\hbar v|q| = |E - U_0|$ the channel modes are joined to modes in the wide region, as indicated schematically by the (black) dotted curves.

to the angle of incidence (while σ is measured along the interface). This quantity becomes independent of α [in the interval $(\alpha_c, \pi/2)$] when the charge density in the p-doped region goes to zero at fixed charge density in the n-doped region,

$$\sigma_\perp \to 1/k_F \ \text{ if } \ |E_F - U_0| \ll E_F \sin^2 \alpha. \tag{6.16}$$

In this limit it does not matter for the sign of the shift if E_F is larger or smaller than U_0. Since the perpendicular displacement of the two spinor components equals $\delta_0^\perp = \delta_0 \cos \alpha = 1/k_F$, the limit (6.16) for $\sigma_\perp$ implies

that upon reflection one component has shift $\sigma_\perp - \delta_0^\perp = 0$ equal to zero while the other component has shift $\sigma_\perp + \delta_0^\perp = 2/k_F$.

As illustrated in Fig. 6.1, the GH shift accumulates upon multiple reflections in the channel between two p-n interfaces. If the separation W of the two interfaces is large compared to the wave length λ_F, the motion between reflections may be treated semiclassically. The time between two subsequent reflections is $W/v\cos\alpha$, so the effect of the GH shift on the velocity $v_\parallel$ along the junction is given by

$$v_\parallel = v\sin\alpha + (\sigma/W)v\cos\alpha. \tag{6.17}$$

Substitution of Eq. (6.14) shows that, for $U_0 > E_F$, the velocity $v_\parallel$ vanishes at an angle α^{**} satisfying the equation

$$\sin^2\alpha^{**} = (U_0/E_F - 1)(\kappa W + 1)^{-1}, \tag{6.18}$$

which for $k_F W \gg 1$ has the solution

$$\alpha^{**} = \alpha_c + \frac{(1 - \sin\alpha_c)^2}{(k_F W)^2 \sin 2\alpha_c \sin^2\alpha_c} + \mathcal{O}(k_F W)^{-4}. \tag{6.19}$$

6.4   Effects on Dispersion and Conductance

The vanishing velocity shows up as a minimum in the dispersion relation, obtained by solving the Dirac equation (6.2) with the potential profile

$$U(x) = \begin{cases} U_0 & \text{for } |x| > W/2, \\ 0 & \text{for } |x| < W/2. \end{cases} \tag{6.20}$$

Matching of propagating waves to decaying waves at $x = -W$ and $x = 0$ produces the following relation between E and q:

$$[q^2 + E(U_0 - E)]\sin kW + k\kappa\cos kW = 0, \tag{6.21}$$

$$k = \sqrt{E^2 - q^2}, \quad \kappa = \sqrt{q^2 - (U_0 - E)^2}. \tag{6.22}$$

The dispersion relation $E(q)$ is plotted for the first few modes in Fig. 6.3. The slope determines the velocity, $v_\parallel = dE/\hbar dq$. The minima in
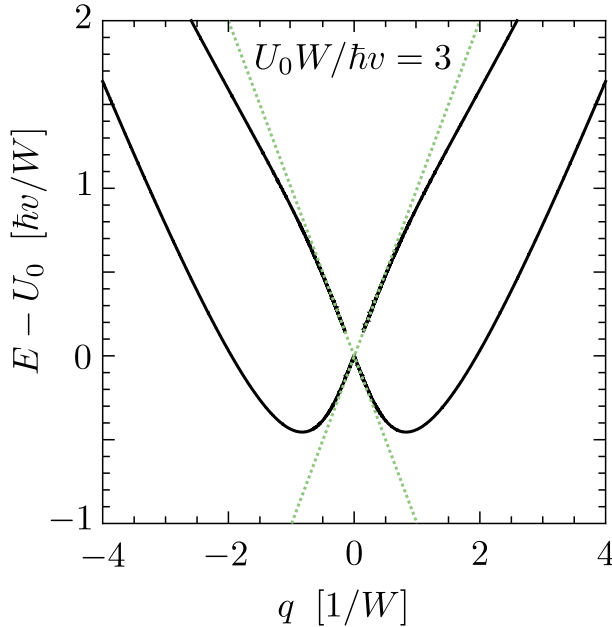
Figure 6.4. Same as Fig. 6.3, but now showing the lowest channel modes in the fully quantum mechanical regime $U_0 W/\hbar v = 3$. The two minima at $q = \pm 0.83\, W^{-1}$ each contribute independently an amount of $4e^2/h$ to the conductance.

the dispersion relation where $v_\parallel = 0$ are clearly visible for $E \lesssim U_0$. The locations of the minima are precisely[3] given by Eq. (6.18) (red dashed curve). For $E \gtrsim U_0$ the GH effect increases the velocity, which is visible in the dispersion relation as a local increase in the slope of the dispersion relation. The solid curves in Fig. 6.3 give the dispersion relation of modes that are confined to the narrow n-doped channel. At the dotted lines $\hbar v|q| = |E - U_0|$ these channel modes are joined to the modes in the wide p-doped region (as indicated by the dotted curves in Fig. 6.3).

As the channel width is reduced so that $U_0 W/\hbar v$ becomes of order unity, we enter the fully quantum mechanical regime. The minimum in the dispersion relation becomes very pronounced for the lowest channel

---

[3]Although the equation (6.18) for zero velocity was derived semiclassically, it is in fact quantum mechanically exact — as we have found by differentiating the dispersion relation (6.21) with respect to q and searching for the value $q^{**} = E \sin \alpha^{**}$ at which the derivative vanishes.
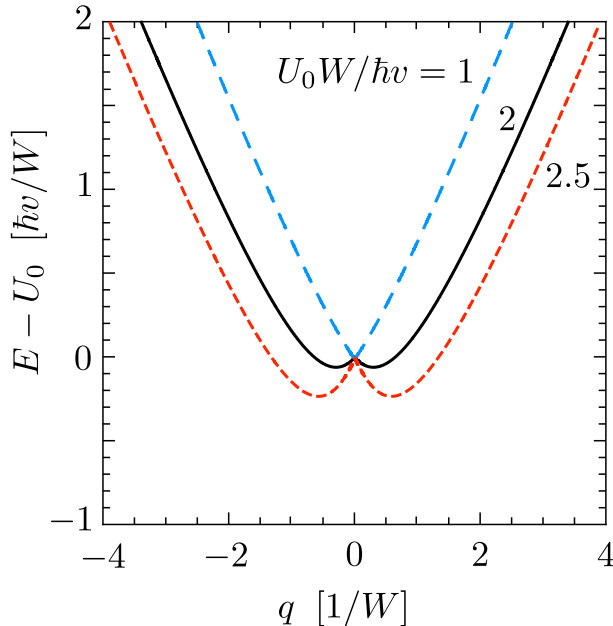
Figure 6.5. Plot of the lowest mode for three values of $U_0 W/\hbar v$, showing how the the two minima merge into a single minimum at $q = 0$ upon reducing W.

mode, as we show in Fig. 6.4. There are two minima at $q \approx 1/W$ and $q \approx -1/W$, each contributing to the conductance a quantum of e^2/h per spin and valley degree of freedom. The total contribution to the conductance from the lowest channel mode is therefore $8e^2/h$. As shown in Fig. 6.5, if W is reduced further, the two degenerate minima in the dispersion relation merge into a single minimum at $q = 0$ (this happens at $U_0 W/\hbar v = 1.57$), and for smaller W the lowest channel mode again contributes the usual amount of $4e^2/h$ to the conductance.

6.5 Numerical Test

To test these analytical predictions, we have performed numerical simulations of electrical conduction in a tight-binding model of a graphene sheet covered by a split-gate electrode. The geometry is similar to that studied in Ref. [124] (but not in the p-n junction regime of interest here). Using the recursive Green function technique on a honeycomb lattice of
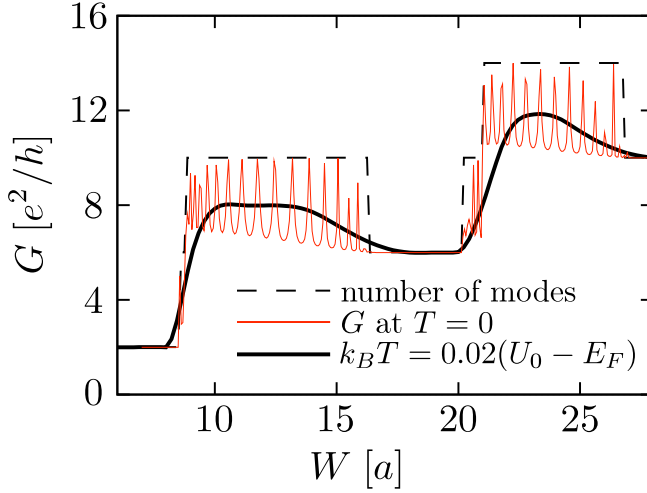
Figure 6.6. Conductance versus channel width, calculated numerically at zero temperature (thin red curve) and at a finite temperature (thick black curve). The dashed black curve gives the number of propagating modes, calculated from the dispersion relation.

carbon atoms (lattice constant a) we obtain the transmission matrix t, and from there the conductance $G = (2e^2/h)\mathrm{Tr}\, tt^\dagger$. Only the twofold spin degeneracy is included by hand as a prefactor, all other degeneracies follow from the simulation. The graphene strip is terminated in the x-direction by zigzag boundaries (separated by a distance $W_{\mathrm{total}} = 220\, a$), while it is infinitely long in the y-direction. A smooth potential profile defines a long and narrow channel of length $L = 1760\, a$ and a width W which we vary between 0 and $30\, a$. The potential rises from 0 in the wide reservoirs (far from the narrow channel), to $U_0 = 0.577\, \hbar v/a$ underneath the gate, and has an intermediate value of $U_{\mathrm{channel}} = 0.277\, \hbar v/a$ inside the channel (where the gate is split). The Fermi energy is kept at $E_F = 0.547\, \hbar v/a$, so that it lies in the valence band underneath the gate, while it lies in the conduction band inside reservoirs and channel.

Results of the simulations are shown in Fig. 6.6. From the dispersion relation we read off the total number of propagating modes (dashed curve). The zigzag edges of the graphene strip support one spin-degenerate edge mode, so the conductance levels off at $2e^2/h$ as the channel is pinched off. Upon widening the channel, the new channel modes have the 8-fold

degeneracy predicted by our analytical theory. The valley degeneracy is not exact (notice the small intermediate step at $W = 20\,a$), as expected for a finite lattice constant. The zero-temperature conductance (thin red curve) shows pronounced Fabry-Perot type oscillations, due to multiple reflections at the entrance and exit of the channel, with an envelope that follows closely the number of propagating modes.

At finite temperature (black curve) the oscillations are averaged out, but the excess conductance characteristic of the Goos-Hänchen effect remains clearly observable at the temperature $T = 0.02(U_0 - E_F)/k_B$ used in the simulation. Scaling up to realistic parameter values, we can set the channel width $W = 100\,\text{nm}$ at the first conductance step, hence $U_0 - E_F = 0.03\,\hbar v/W \simeq 10\,\text{K}$, so this would correspond to a temperature of $0.2\,\text{K}$. The Fermi wave length λ_F in the channel is of order $100\,\text{nm}$ for these parameter values (of the same order as W at the first step), well above the typical width $d \simeq 40\,\text{nm}$ of a p-n interface [125]. Note that d is two orders of magnitude larger than $a = 0.25\,\text{nm}$, so the potential is indeed smooth on the scale of the lattice constant (as assumed both in the analytical and numerical calculations). For ballistic transport through the constriction the mean free path should be well above the $100\,\text{nm}$ scale.

6.6　Conclusion

In conclusion, we have identified and analyzed a novel pseudospin-dependent scattering effect in graphene, that manifests itself as an $8e^2/h$ conductance step in a bipolar junction. This quantum Goos-Hänchen effect mimics the effects of a pseudospin degeneracy, by producing a pronounced double minimum in the dispersion relation of an n-doped channel with p-doped boundaries. Such a channel can be created electrostatically, and might therefore be a versatile building block in an electronic circuit.

Bibliography

[1] J. D. Joannopoulos, R. D. Meade, and J. N. Winn, *Photonic Crystals: Molding the Flow of Light* (Princeton University Press, 1995).

[2] V. Tolmachev, T. Perova, E. Astrova, B. Volchek, and J. K. Vij, Phys. Stat. Sol. (a) **197**, 544 (2003).

[3] R. van der Heijden, E.J. Geluk, R. W. van der Heijden, F. Karouta, P. A. M. Nouwens, Y. S. Oei, E. M. Roeling, E. Smalbruggea, T. de Vries, and H. W. M. Salemink, *proc. Semiconductor Advances for Future Electronics (SAFE) 03*, 25-26 November 2003, ISBN 90-73461-39-1; STW, Veldhoven, The Netherlands, 2003, pp. 604-609.

[4] http://www.cfn.uni-karlsruhe.de/web/.

[5] J. V. Sanders, Nature **204**, 1151 (1964).

[6] J. B. Jones, J. V. Sanders, and E. R. Segnit, Nature **204**, 990 (1964).

[7] P. J. Darragh, A. J. Gaskin, B. C. Terrell, and J. V. Sanders, Nature **209**, 13 (1966).

[8] J. V. Sanders, Acta Crystallogr. A **24**, 427 (1968).

[9] H. Ghiradella, Appl. Opt. **30**, 3492 (1991).

[10] P. Vukusic, J. R. Sambles, and H. Ghiradella, Photonics Sci. News **6**, 61 (2000).

[11] A. R. Parker, Materials Today **5**, 26 (2002).

[12] V. N. Bogomolov, S. V. Gaponenko, I. N. Germanenko, A. M. Kapitonov, E. P. Petrov, N. V. Gaponenko, A. V. Prokofiev, A. N. Ponyavina, N. I. Silvanovich, and S. M. Samoilovich, Phys. Rev. E **55**, 7619 (1997).

[13] R. O. Prum, T. Quinn, and R. H. Torres, J. Exp. Biol. **209**, 748 (2006).

[14] M. Plihal and A. A. Maradudin, Phys. Rev. B **44**, 8565 (1991).

[15] P. R. Villeneuve and M. Piché, Phys. Rev. B **46**, 4969 (1992).

[16] K. Sakoda, Phys. Rev. B **52**, 8992 (1995).

[17] D. Cassagne, C. Jouanin, and D. Bertho, Phys. Rev. B **53**, 7134 (1996).

[18] N. Susa, J. Appl. Phys. **91**, 3501 (2002).

[19] M. Notomi, Phys. Rev. B **62**, 10696 (2000).

[20] S. Foteinopoulou and C. M. Soukoulis, Phys. Rev. B **67**, 235107 (2003).

[21] A. Berrier, M. Mulot, M. Swillo, M. Qiu, L. Thylén, A. Talneau, and S. Anand, Phys. Rev. Lett. **93**, 073902 (2004).

[22] K. Guven, K. Aydin, K. B. Alici, C. M. Soukoulis, and E. Ozbay, Phys. Rev. B **70**, 205125 (2004).

[23] P. V. Parimi, W. T. Lu, P. Vodo, J. Sokoloff, J. S. Derov, and S. Sridhar, Phys. Rev. Lett. **92**, 127401 (2004).

[24] R. Moussa, S. Foteinopoulou, L. Zhang, G. Tuttle, K. Guven, E. Ozbay, and C. M. Soukoulis, Phys. Rev. B **71**, 085106 (2005).

[25] R. Gajić, R. Meisels, F. Kuchar, and K. Hingerl, Phys. Rev. B **73**, 165310 (2006).

[26] P. R. Wallace, Phys. Rev. **71**, 622 (1947).

[27] K. S. Novoselov, A. K. Geim, S. V. Morozov, D. Jiang, Y. Zhang, S. V. Dubonos, I. V. Grigorieva, and A. A. Firsov, Science **306**, 666 (2004).

[28] F. D. M. Haldane and S. Raghu, Phys. Rev. Lett. **100**, 013904 (2008), `arXiv:cond-mat/0503588`.

[29] S. Raghu and F. D. M. Haldane, Phys. Rev. A **78**, 033834 (2008), `arXiv:cond-mat/0602501`.

[30] J. C. Meyer, A. K. Geim, M. I. Katsnelson, K. S. Novoselov, T. J. Booth, and S. Roth, Nature **446**, 60 (2007).

[31] Y. Zhang, Y.-W. Tan, H. L. Stormer, and P. Kim, Nature **438**, 201 (2005).

[32] J. W. McClure, Phys. Rev. **104**, 666 (1956).

[33] G. W. Semenoff, Phys. Rev. Lett. **53**, 2449 (1984).

[34] D. P. DiVincenzo and E. J. Mele, Phys. Rev. B **29**, 1685 (1984).

[35] F. D. M. Haldane, Phys. Rev. Lett. **61**, 2015 (1988).

[36] R. E. Peierls, Helv. Phys. Acta **7**, 81 (1934).

[37] R. E. Peierls, Ann. Inst. Henri Poincaré **5**, 177 (1935).

[38] L. D. Landau, Phys. Z. Sowjetunion **11**, 26 (1937).

[39] L. D. Landau and E. M. Lifshitz, *Statistical Physics* Part I, Sections 137 and 138 (Pergamon, 1980).

[40] N. D. Mermin and H. Wagner, Phys. Rev. Lett. **17**, 1133 (1966).

[41] P. C. Hohenberg, Phys. Rev. **158**, 383 (1967).

[42] N. D. Mermin, Phys. Rev. **176**, 250 (1968).

[43] J. A. Venables, G. D. T. Spiller, and M. Hanbücken, Rep. Prog. Phys. **47**, 399 (1984).

[44] M. Zinke-Allmang, L. C. Feldman, and M. H. Grabow, Surf. Sci. Rep. **16**, 377 (1992).

[45] J. W. Evans, P. A. Thiel, and M. C. Bartelt, Surf. Sci. Rep. **61**, 1 (2006).

[46] D. R. Nelson and L. Peliti, J. Phys. **48**, 1085 (1987).

[47] P. Le Doussal and L. Radzihovsky, Phys. Rev. Lett. **69**, 1209 (1992).

[48] D. R. Nelson, T. Piran, and S. Weinberg, *Statistical Mechanics of Membranes and Surfaces* (World Scientific, 2004).

[49] R. R. Nair, P. Blake, A. N. Grigorenko, K. S. Novoselov, T. J. Booth, T. Stauber, N. M. R. Peres, and A. K. Geim, Science **320**, 1308 (2008).

[50] H. Schomerus, Phys. Rev. B **76**, 045433 (2007).

[51] S. Patchkovskii, J. S. Tse, S. N. Yurchenko, L. Zhechkov, T. Heine, and G. Seifert, Proc. Natl. Acad. Sci. **102**, 10439 (2005).

[52] V. P. Gusynin, S. G. Sharapov, and J. P. Carbotte, Int. J. Mod. Phys. B **21**, 4611 (2007).

[53] M. I. Katsnelson and K. S. Novoselov, Solid State Comm. **143**, 3 (2007).

[54] C. W. J. Beenakker, Rev. Mod. Phys. **80**, 1337 (2008).

[55] A. H. Castro Neto, F. Guinea, N. M. R. Peres, K. S. Novoselov, and A. K. Geim, Rev. Mod. Phys. **81**, 109 (2009).

[56] A. Taflove and S. C. Hagness, *Computational Electrodynamics: The Finite-Difference Time-Domain Method* (Artech House, 2005).

[57] K. Yee, IEEE Trans. Antennas and Propagation **14**, 302 (1966).

[58] http://ab-initio.mit.edu/wiki/index.php/Meep.

[59] J.-P. Berenger, J. Comput. Phys. **114**, 185 (1994).

[60] Z. S. Sacks, D. M. Kingsland, R. Lee, and J. F. Lee, IEEE Trans. Antennas and Propagation **43**, 1460 (1995).

[61] A. Farjadpour, D. Roundy, A. Rodriguez, M. Ibanescu, P. Bermel, J. D. Joannopoulos, S. G. Johnson, and G. W. Burr, Opt. Lett. **31**, 2972 (2006).

[62] http://ab-initio.mit.edu/wiki/index.php/MIT_Photonic_Bands.

[63] Z. Bai, J. Demmel, J. Dongarra, A. Ruhe, and H. van der Vorst, editors, *Templates for the solution of Algebraic Eigenvalue Problems: A Practical Guide* (SIAM, 2000).

[64] M. V. Berry, Proc. R. Soc. A **392**, 45 (1984).

[65] A. Shapere and F. Wilczek, eds., *Geometric Phases in Physics* (World Scientific, 1989).

[66] J. Anandan, J. Christian, and K. Wanelik, Am. J. Phys. **65**, 180 (1997).

[67] D. J. Griffiths, *Introduction to Quantum Mechanics* (Prentice Hall, 1994).

[68] M. V. Berry, Physics Today **43** (12), 34 (1990).

[69] S. M. Rytov, Dokl. Akad. Nauk. USSR **18**, 263 (1938), reprinted in Ref. [126], p. 6; V. V. Vladimirskii, Dokl. Akad. Nauk. USSR **21**, 222 (1941), reprinted in Ref. [126], p. 11.

[70] D. S. Wiersma, M. P. van Albada, and A. Lagendijk, Rev. Sci. Instrum. **66**, 5473 (1995).

[71] E. Akkermans and G. Montambaux, *Mesoscopic Physics of Electrons and Photons* (Cambridge University Press, 2007).

[72] Y. Kuga and A. Ishimaru, J. Opt. Soc. Am. A **8**, 831 (1984).

[73] M. P. van Albada and A. Lagendijk, Phys. Rev. Lett. **55**, 2692 (1985).

[74] P. E. Wolf and G. Maret, Phys. Rev. Lett. **55**, 2696 (1985).

[75] K. Y. Bliokh, Phys. Lett. A **344**, 127 (2005).

[76] M. I. Katsnelson, Eur. Phys. J. B **51**, 157 (2006).

[77] J. Tworzydło, B. Trauzettel, M. Titov, A. Rycerz, and C. W. J. Beenakker, Phys. Rev. Lett. **96**, 246802 (2006).

[78] Y. M. Blanter and I. Martin, Phys. Rev. B **76**, 155433 (2007).

[79] H. van Houten and C. W. J. Beenakker, in *Analogies in Optics and Micro Electronics*, edited by W. van Haeringen and D. Lenstra (Kluwer, 1990).

[80] T. Ando, S. Wakahara, and H. Akera, Phys. Rev. B **40**, 11609 (1989).

[81] D. Cassagne, C. Jouanin, and D. Bertho, Appl. Phys. Lett. **70**, 289 (1997).

[82] J.-Y. Ye and S. Matsuo, J. Appl. Phys. **96**, 6934 (2004).

[83] A. K. Geim and K. S. Novoselov, Nature Materials **6**, 183 (2007).

[84] E.-A. Kim and A. H. Castro Neto, EPL **84**, 57007 (2008).

[85] M. Titov, EPL **79**, 17004 (2007).

[86] A. Rycerz, J. Tworzydło, and C. W. J. Beenakker, EPL **79**, 57003 (2007).

[87] P. M. Ostrovsky, I. V. Gornyi, and A. D. Mirlin, Phys. Rev. Lett. **98**, 256801 (2007).

[88] S. G. Johnson and J. D. Joannopoulos, Opt. Express **8**, 173 (2001).

[89] R. A. Sepkhanov, Ya. B. Bazaliy, and C. W. J. Beenakker, Phys. Rev. A **75**, 063813 (2007).

[90] X. Zhang, Phys. Lett. A **372**, 3512 (2008).

[91] R. Bhandari, Phys. Rep. **281**, 1 (1997).

[92] A. Tomita and R. Y. Chiao, Phys. Rev. Lett. **57**, 937 (1986).

[93] K. S. Novoselov, A. K. Geim, S. V. Morozov, D. Jiang, M. I. Katsnelson, I. V. Grigorieva, S. V. Dubonos, and A. A. Firsov, Nature **438**, 197 (2005).

[94] Y. Zhang, Y.-W. Tan, H. L. Stormer, and P. Kim, Nature **438**, 201 (2005).

[95] R. A. Sepkhanov and C. W. J. Beenakker, Opt. Commun. **281**, 5267 (2008).

[96] X. Zhang, Phys. Rev. Lett. **100**, 113903 (2008).

[97] J. L. Garcia-Pomar, A. Cortijo, and M. Nieto-Vesperinas, Phys. Rev. Lett. **100**, 236801 (2008).

[98] J. B. Pendry and S. A. Ramakrishna, J. Phys. Cond. Matter **15**, 6345 (2003).

[99] C. W. J. Beenakker, A. R. Akhmerov, P. Recher, and J. Tworzydło, Phys. Rev. B **77**, 075409 (2008).

[100] V. V. Cheianov, V. Fal'ko, and B. L. Altshuler, Science **315**, 1252 (2007).

[101] K. Kobayashi, J. Phys. Cond. Matter **18**, 3703 (2006).

[102] P. Carmier and D. Ullmo, Phys. Rev. B **77**, 245413 (2008).

[103] E. Akkermans, P. E. Wolf, and R. Maynard, Phys. Rev. Lett. **56**, 1471 (1986).

[104] M. B. van der Mark, M. P. van Albada, and A. Lagendijk, Phys. Rev. B **37**, 3575 (1988).

[105] D. V. Kupriyanov, I. M. Sokolov, and M. D. Havey, Opt. Commun. **243**, 165 (2004).

[106] D. V. Kupriyanov, I. M. Sokolov, C. I. Sukenik, and M. D. Havey, Laser Phys. Lett. **3**, 223 (2006).

[107] R. Berkovits and M. Kaveh, Phys. Rev. B **37**, 584 (1988).

[108] T. Ando and T. Nakanishi, J. Phys. Soc. Japan **67**, 1704 (1998).

[109] T. Ando, T. Nakanishi, and R. Saito, J. Phys. Soc. Japan **67**, 2857 (1998).

[110] T. Ando and H. Suzuura, J. Phys. Soc. Japan **71**, 2758 (2002).

[111] M. Braun, L. Chirolli, and G. Burkard, Phys. Rev. B **77**, 115433 (2008).

[112] R. A. Sepkhanov, J. Nilsson, and C. W. J. Beenakker, Phys. Rev. B **78**, 045122 (2008).

[113] J. X. Zhu, D. J. Pine, and D. A. Weitz, Phys. Rev. A **44**, 3948 (1991).

[114] S. Fiebig, C. M. Aegerter, W. Bührer, M. Störzer, E. Akkermans, G. Montambaux, and G. Maret, EPL **81**, 64004 (2008).

[115] F. Goos and H. Hänchen, Ann. Phys. (Leipzig) **436**, 333 (1947).

[116] F. de Fornel, *Evanescent Waves: From Newtonian Optics to Atomic Optics* (Springer, 2001).

[117] R. Marqués, F. Martín, and M. Sorolla, *Metamaterials with Negative Parameters* (Wiley-Interscience, 2007).

[118] K. L. Tsakmakidis, A. D. Boardman, and O. Hess, Nature **450**, 397 (2007).

[119] S. C. Miller, Jr. and N. Ashby, Phys. Rev. Lett. **29**, 740 (1972).

[120] D. M. Fradkin and R. J. Kashuba, Phys. Rev. D **9**, 2775 (1974).

[121] N. A. Sinitsyn, Q. Niu, J. Sinova, and K. Nomura, Phys. Rev. B **72**, 045346 (2005).

[122] X. Chen, C.-F. Li, and Y. Ban, Phys. Rev. B **77**, 073307 (2008).

[123] L. Zhao and S. F. Yelin, `arXiv:0804.2225`.

[124] I. Snyman, J. Tworzydło, and C. W. J. Beenakker, Phys. Rev. B **78**, 045118 (2008).

[125] B. Huard, J. A. Sulpizio, N. Stander, K. Todd, B. Yang, and D. Goldhaber-Gordon, Phys. Rev. Lett. **98**, 236803 (2007).

[126] B. Markovski and V. I. Vinitskiy, *Topological Phases in Quantum Theory* (World Scientific, 1989).

Samenvatting

Een fotonisch kristal is een bijzonder kunstmatig materiaal, geïnspireerd op natuurlijke kristallen, dat uit periodieke optische elementen bestaat. Bijvoorbeeld, in een blok worden gaatjes geboord of worden paaltjes geplaatst op een regelmatige manier. Een fotonisch kristal heeft als bijzondere eigenschap dat het licht er niet door heen kan in een bepaald frequentie-interval. Dit frequentie-interval heet de "kloof" van het fotonische kristal. Er zijn allerlei soorten fotonische kristallen, maar de driehoekige variant is de meest bekende, omdat in het bijzonder dit kristal een tamelijk grote kloof heeft. (Onder driehoekige variant verstaan we een driehoekig rooster van gaatjes of paaltjes.)

De grafiek van frequentie uitgezet tegen golfvector laat, behalve de kloof, nog een eigenaardigheid zien, die tot voor kort onopgemerkt was gebleven: er is een raakpunt waar slechts één enkele golfvector is toegestaan. In de vrije ruimte bevindt zo'n raakpunt zich uitsluitend bij frequentie nul. In het fotonische kristal is een tweede raakpunt ontstaan, bij frequentie ongelijk aan nul. Ondanks het feit dat de frequentie van het laatstgenoemde raakpunt ongelijk aan nul is, heeft het raakpunt toch iets gemeen met frequentie nul, namelijk, de golflengte is oneindig op dit punt.

In grafeen (een enkele laag van een koolstofkristal) bestaat ook zo'n raakpunt. Daar noemt men het een "Diracpunt", omdat de golfvergelijking er de vorm aanneemt van de Diracvergelijking uit de relativistische quantumfysica. Wij hebben ons laten inspireren door de recente ontdekking van grafeen en wij zijn op zoek gegaan naar het effect van een Diracpunt op de eigenschappen van fotonen.

Wij hebben ontdekt dat de doorlaatbaarheid van het fotonische kris-
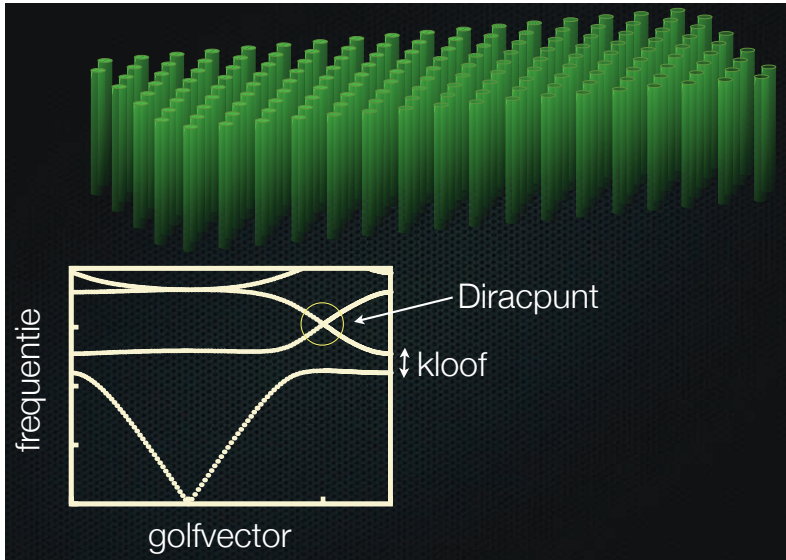
Figuur 6.7. Driehoekig fotonisch kristal en de bijbehorende grafiek van frequentie als functie van golfvector. Frequenties in de kloof kunnen niet door het kristal heen. Boven de kloof bevindt zich een raakpunt waar slechts een enkele golfvector is toegestaan. Dit zogenaamde Diracpunt zorgt ervoor dat de fotonen bijzondere eigenschappen krijgen, waaronder een halftallige spin.

tal, bij frequenties in de buurt van het Diracpunt, op een bijzondere wijze van de dikte van het kristal afhangt. Het product van doorlaatbaarheid en kristaldikte is constant, onafhankelijk van materiaaleigenschappen. Hetzelfde effect is bekend voor de doorlaatbaarheid van het grafeen voor elektronen, en er zijn meer parallellen tussen beide systemen. Wij hebben ook laten zien dat de analogie tussen beide systemen in de omgekeerde richting werkt: een effect, dat in fotonische kristallen en andere kunstmatige optische materialen een belangrijke rol speelt, namelijk het Goos-Hänchen effect bij totale interne reflectie, kan in grafeen ook van groot belang zijn.

Het meest verrassende effect van het Diracpunt in een fotonisch kristal is dat het foton zich gedraagt alsof het een halftallige spin heeft, net als een elektron. Wij hebben berekend dat de halftallige spin kan worden waargenomen door de verschuiving van interferentiepatronen, zodat constructieve interferentie destructief wordt – en vice versa. Het Diracpunt

voegt zo een nieuwe reeks van mogelijkheden toe aan de manipulatie van licht in fotonische kristallen.

Publications

- *Quantum Goos-Hänchen effect in graphene*, C. W. J. Beenakker, R. A. Sepkhanov, A. R. Akhmerov, and J. Tworzydło, Phys. Rev. Lett. **102**, 146804 (2009). (Chapter 6.)

- *Extinction of coherent backscattering by a disordered photonic crystal with a Dirac spectrum*, R. A. Sepkhanov, A. Ossipov, and C. W. J. Beenakker, EPL **85**, 14005 (2009). (Chapter 5.)

- *How to detect the pseudospin-$\frac{1}{2}$ Berry phase in a photonic crystal with a Dirac spectrum*, R. A. Sepkhanov, Johan Nilsson, and C. W. J. Beenakker, Phys. Rev. B **78**, 045122 (2008). (Chapter 4.)

- *Numerical test of the theory of pseudo-diffusive transmission at the Dirac point of a photonic band structure*, R. A. Sepkhanov and C. W. J. Beenakker, Opt. Commun. **281**, 5267 (2008). (Chapter 3.)

- *Extremal transmission at the Dirac point of a photonic band structure*, R. A. Sepkhanov, Ya. B. Bazaliy, and C. W. J. Beenakker, Phys. Rev. A **75**, 063813 (2007). (Chapter 2.)

Curriculum Vitæ

I was born in Moscow on the 26th of March 1983, where I attended primary and high schools. I finished the school in the year 2000. In September 2000 I entered the Faculty of Physics of Moscow State University. After 2.5 years of General Physics studies I started to focus on Theoretical Physics and became affiliated with the Chair of Theoretical Physics within the Faculty. I worked under the supervision of Prof. A. V. Borisov on the phenomenology of high-energy physics in particular: neutrino oscillations, lepton flavor violation and phenomenology of Standard Model extensions. In 2006 I defended my University Diploma thesis titled *Conversion $e \rightarrow \mu$ in an external electromagnetic field in theories beyond the Standard Model*.

In September 2006 I started to work on a PhD project at the Leiden Institute of Physics of Leiden University as an employee of the Foundation for Fundamental Research on Matter (FOM). My supervisor was Prof. C.W.J. Beenakker of the Instituut-Lorentz for Theoretical Physics. I worked on transport properties of nano systems such as graphene and photonic crystals with a Dirac spectrum. The greater part of that work is presented in this thesis. In the course of my PhD I attended a number of schools and conferences in The Netherlands, Germany, Slovenia, Finland and Italy. To most of them I contributed with a poster or a talk.

Stellingen

behorend bij het proefschrift

Light Scattering by Photonic Crystals with a Dirac Spectrum

1. The transmitted photon current at the Dirac point of a photonic crystal is inversely proportional to the crystal length.

   Chapter 2

2. A triangular lattice photonic crystal attaches a spin-$\frac{1}{2}$ to the photon.

   Chapter 4

3. The extinction of coherent backscattering predicted for ultrarelativistic electrons has a photonic analogue.

   Chapter 5

4. The Goos-Hänchen shift of a beam upon total internal reflection can be observed as a conductance step of $8e^2/h$ in a graphene bipolar junction.

   Chapter 6

5. The "optical clepsydra" introduced by Tsakmakidis et al. is more properly called "optical hourglass".

   K. L. Tsakmakidis, A. D. Boardman, and O. Hess,
   Nature **450**, 397 (2007)

6. The common attribution of the Goos-Hänchen shift to Newton is inappropriate, since he got the sign wrong.

I. Newton, *Opticks* (London, 1730)

7. The surmise by Akkermans et al. that the Fano factor depends on the fractal dimension of a conductor is unfounded.

E. Akkermans, G. V. Dunne, and A. Teplyaev,
arXiv:0903.3681

8. The photon dynamics in the Lévi glass of Barthelemy et al. differs markedly from a Lévy flight because of finite-size effects.

P. Barthelemy, J. Bertolotti, and D. S. Wiersma,
Nature **453**, 495 (2008)

9. The amount of irrationality in science is underestimated.

Ruslan Sepkhanov
Leiden, 20 May 2009